Environmental-Induced Damage in Tin (Sn) and Aluminum (Al) Alloys

by

Venkata Sathya Sai Renuka Vallabhaneni

A Dissertation Presented in Partial Fulfillment
of the Requirements for the Degree
Doctor of Philosophy

Approved April 2017 by the
Graduate Supervisory Committee:

Nikhilesh Chawla, Chair
Jagannathan Rajagopalan
Kiran Solanki

ARIZONA STATE UNIVERSITY

May 2017

ABSTRACT

Sn and Al alloys are widely used in various industries. Environmental-induced damage resulting in whiskering in Sn and corrosion in Al account for numerous failures globally every year. Therefore, for designing materials that can better withstand these failures, a comprehensive study on the characterization of the damage is necessary. This research implements advanced characterization techniques to study the above-mentioned environmental-induced damage in Sn and Al alloys.

Tin based films are known to be susceptible to whisker growth resulting in numerous failures. While the mechanisms and factors affecting whisker growth have been studied extensively, not much has been reported on the mechanical properties of tin whiskers themselves. This study focuses on the tensile behavior of tin whiskers. Tensile tests of whiskers were conducted *in situ* a dual beam focused ion beam (FIB) with a scanning electron microscope (SEM) using a micro electro-mechanical system (MEMS) tensile testing stage. The deformation mechanisms of whiskers were analyzed using transmission electron microscopy (TEM).

Due to the heterogenous nature of the microstructure of Al 7075, it is susceptible to corrosion forming corrosion products and pits. These can be sites for cracks nucleation and propagation resulting in stress corrosion cracking (SCC). Therefore, complete understanding of the corrosion damaged region and its effect on the strength of the alloy is necessary. Several studies have been performed to visualize pits and understand their effect on the mechanical performance of Al alloys using two-dimensional (2D) approaches which are often inadequate. To get a thorough understanding of the pits, it is necessary for three-dimensional (3D) studies. In this study, Al 7075 alloys were corroded

in 3.5 wt.% NaCl solution and X-ray tomography was used to obtain the 3D microstructure of pits enabling the quantification of their dimensions accurately. Furthermore, microstructure and mechanical property correlations helped in a better understanding of the effect of corrosion. Apart from the pits, a surface corrosion layer also forms on Al. A subsurface damage layer has also been identified that forms due to the aggressive nature of NaCl. Energy dispersive X-ray spectroscopy (EDX) and nanoindentation helped in identifying this region and understanding the variation in properties.

DEDICATION

To my mother Vasantha Lakshmi for her support and encouragement throughout which enabled me to reach this stage of my life.

ACKNOWLEDGMENTS

I would like to thank my adviser, Prof. Nikhilesh Chawla for providing me an opportunity to work under him. His constant guidance, support and encouragement throughout the past few years have not only trained me to do high quality research but also imbibed in me the never give up attitude. I would like to express my gratitude towards my committee members Prof. Jagannathan Rajagopalan and Prof. Kiran Solanki for taking their time in evaluating my research. I would like to acknowledge the funding support from the air force office of scientific research (AFOSR) through the multi-university research initiative (MURI) program on Peridynamics. I would also like to acknowledge the use of facilities within the center for 4D materials science (4DMS) and the center for solid state sciences at Arizona state university.

I am grateful to research scientist, Dr. Jason Williams for his assistance with the technical challenges in the lab and in my research. I would also like to heartfully thank members of Chawla research group for their wonderful support and collaboration. Finally, I would like to express my sincere gratitude towards my family and friends for their belief in me and constantly motivating me towards achieving my dreams.

TABLE OF CONTENTS

Page

LIST OF TABLES

LIST OF FIGURES

Figure Page

Figure Page

Figure Page

Figure Page

Figure Page

CHAPTER 1

INTRODUCTION

Restricted usage of lead (Pb) in electronic products due to its toxicity has resulted in electronic suppliers moving towards the usage of pure Sn [1]. However, the usage of pure Sn and high Sn based coatings without Pb has resulted in a reliability concern regarding the formation of conductive tin whiskers. These tin whiskers are thin filaments known to grow spontaneously from Sn and can pose a serious reliability risk to electronic assemblies. They are widespread in electronic appliances and are found in various areas such as pins of components, connectors, metal lids etc. They are undesirable because they can grow long enough to bridge components to cause short-circuits, they may break off and interfere with other electronic devices or may cause failure in other ways [2]. Whiskers have been implicated in over $1B of losses [3], many of which are documented on the NASA whisker website [4]. Hence, it is necessary to develop mitigation strategies for tin whiskers for which understanding their growth mechanisms as well as properties is important.

The exact mechanisms for whisker nucleation and growth are still unknown, but, most researchers in the whisker research community come to a consensus that compressive stresses are necessary for their formation [5-7]. Compressive stresses can be induced by mechanical, chemical and thermal effects [8]. While the mechanisms, factors influencing Sn whiskering have been studied for decades, very little is known about the mechanical properties of these. Very few studies have been conducted on the mechanical behavior of Sn whiskers [9, 10] owing to the difficulties of handling, gripping, and

testing such fine-diameter and high-aspect-ratio whiskers [11]. Having an idea of the mechanical properties such as strength of the whisker will enable researchers to predict when it breaks, falls off and damages the device. Strength details could also be helpful for researchers working on developing whisker resistant coatings. These coatings are known to retard whisker growth and contain them within the coat thereby protecting the devices [12]. By knowing the strength, various decisions such as choosing the right materials for the coatings, optimum thickness of the coatings etc. can be made.

There is a need to utilize techniques different from the conventional mechanical testing techniques to be able to perform mechanical tests of such fine diameter and high aspect ratio whiskers reliably. Issues such as manual handling, gripping and accurate measurement of cross-sectional area of whiskers for stress calculations faced by the previous researchers need to be overcome. *In situ* mechanical characterization using microelectromechanical systems (MEMS) has emerged as an excellent technique to carry out tests on miniature specimens such as nanowires, nanorods, whiskers, thin films etc. The high level of integration and miniaturization in these devices allows to perform tests *in situ* and observe the deformation in real time. Owing to the small sizes of the tin whiskers, the utilization of MEMS to obtain the mechanical strength can be useful. While tensile testing of tin whiskers using MEMS has been previously conducted, that study was limited to reporting the strength of only two whiskers [11]. Apart from knowing the strength by performing *in situ* tests, it is also necessary to understand the structure to understand its deformation behavior. Scanning electron microscope with energy

dispersive X-ray spectroscopy capability (SEM-EDX) and transmission electron microscopy (TEM) can be used to obtain structural information of the whiskers.

The first part of this dissertation focusses on achieving a comprehensive understanding of the tensile behavior of the tin whiskers. Accelerated growth techniques can be used to obtain whiskers for performing the tests. *In situ* tensile tests using MEMS carried out on multiple whiskers with different lengths and processing conditions and structure-property correlation after the tests will be instrumental in achieving a better understanding of deformation behavior of tin whiskers. This will ultimately lead to the better development of whisker mitigation techniques.

It is well known that 7xxx series aluminum alloys have been widely used as structural materials due to their attractive properties such as low density, high strength, toughness, ductility and resistance to fatigue [13-15]. Also, out of these, 7075 Al alloy has been the most extensively used. However, these alloys are sensitive to localized corrosion, stress corrosion cracking and exfoliation corrosion [16]. Aluminum alloys usually possess corrosion resistance in air due to the protective nature of the barrier oxide film. But in certain aggressive environments such as halide ion environments (eg. Cl^- ions), these alloys lose their corrosion resistance forming pits and corrosion products. On application of stress, cracks are found to initiate from these damaged regions causing stress corrosion cracking and resulting in premature failure. Hence, corrosion can have a severe effect on aluminum alloys life resulting in their catastrophic failure. Therefore, it is important to understand and completely characterize the corroded region in aluminum alloys to design alloys that can better withstand stress corrosion cracking.

Corroded region in 7075 Al alloys corroded in 3.5 wt.% NaCl solution comprises of corrosion products and pits. It is important to completely characterize the entire damaged region to gain a comprehensive understanding of the corrosion processes in aluminum. Traditionally, characterization of pits was performed using 2D imaging techniques which are often inadequate and might result in inaccurate conclusions. But recent advances in imaging techniques has resulted in the development of three-dimensional (3D) analyses. X-ray tomography is one such technique allowing for the 3D visualization of the microstructure. This technique is advantageous owing to its nondestructive approach as well as providing a high spatial and temporal resolution. This technique can be used to visualize the 3D microstructure of the pits and enabling the accurate quantification of their dimensions.

A surface corrosion product layer forms on aluminum and due to the chemical modification because of corrosion, the presence of defects in it, it is expected to show composition and mechanical properties largely different from the bulk Al alloy. EDX and nanoindentation techniques can be used to understand the localized variation in composition as well as mechanical properties in the damaged region compared to the un-corroded Al.

The second part of this dissertation focuses on completely characterizing the corrosion damaged region of 7075 Al alloys corroded in 3.5 wt.% NaCl solution. X-ray tomography can enable to visualize the pits in 3D and accurately quantify their dimensions. The microstructure visualized can be correlated with the tensile strength. The localized mechanical properties, compositional variation in the corroded region can

provide a better insight in to the corrosion mechanisms. In this way, complete characterization of the corroded region could be obtained which would aid in better understanding of corrosion mechanisms and stress corrosion cracking in Al alloys.

CHAPTER 2

LITERATURE REVIEW

2.1 Tin whiskers

2.1.1 Tin whiskers and reports on common tin whisker failures

Tin whiskers are electrically conductive, crystalline structures that are known to grow from the surface of tin [2]. They may be formed spontaneously from the Sn surface or would need a storage time even up to years to nucleate and grow. They can appear in all kinds of shapes including straight, kinked, bent, forked, and lumps or appear as short irregularly shaped nodules commonly known as hillocks (Figure 1). Striations are observed on the surface of most whiskers giving the appearance of having been extruded [17, 18]. Typical diameters range from 1 μm-4 μm with some reports as high as 10 μm and as low as 0.006 μm [10] and growth rates ranging from 0.03 to 9 mm/year have been reported [19]. Long, straight whiskers have been observed to grow with lengths up to millimeters but lengths in the range of 10 μm–100 μm are observed commonly [8, 20, 10]. Even these short whiskers have become more problematic as the spacing between the conducting elements on circuit boards has decreased [8]. Whiskers have been implicated in over $1B of losses [3], many of which are documented on the NASA whisker web-site [4] including the crash of the Hughes Galaxy satellite, recall of medical pacemakers and a nuclear plant shutdown. There are several ways whiskers can lead to electronic devices failure and some of them are listed. Numerous failures have been attributed to short circuits caused by tin whiskers that bridge closely spaced circuit elements. Tin whiskers

can bend in response to forces such as electrostatic attraction increasing the probability of tin whisker shorts either from two whiskers colliding or from one whisker bending to contact another conductor.

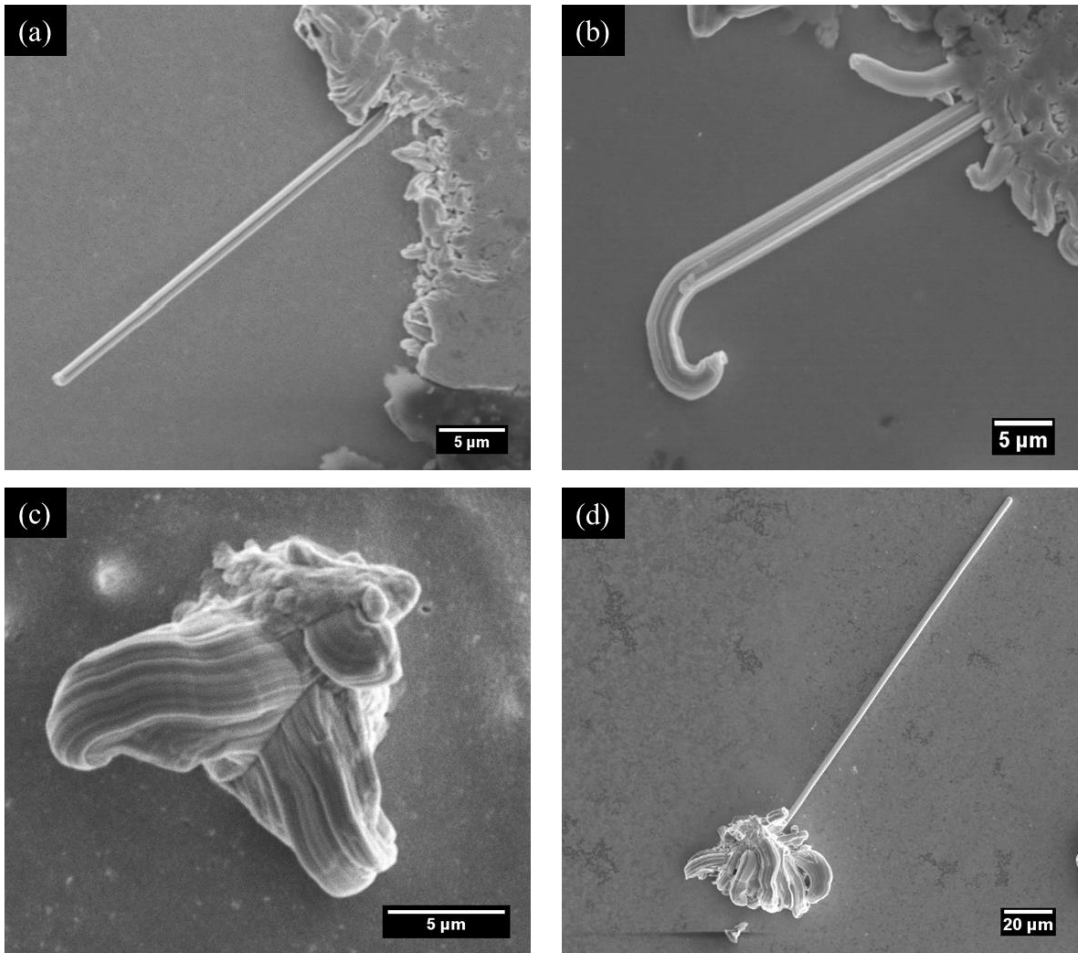

Figure 1. Different kinds of whiskers observed (a) straight whisker (b) whisker with a kink (c) low aspect ratio whisker termed as hillock/nodule (d) whisker forming from the nodules. The striations on the whiskers can also be observed.

Applications with very high levels of current and voltage may cause the whiskers to vaporize into a conductive plasma of ions. These plasmas can carry hundreds of amperes

which can lead to catastrophic damage. Also, the whiskers may fracture and drop on to neighboring portions interfering with their operation [2].

Tin plated films containing more than 3% lead are known to mitigate the formation of tin whiskers and this had been an industry accepted solution for many years [21-23]. But environmental regulations (RoHS [24]) restricting the usage of Pb in electronic products due to its toxicity has resulted in electronic suppliers moving towards the usage of pure Sn [1] leading to the re-emergence of whiskering as a critical reliability issue in Pb-free electronics. Sn whiskers are wide spread in electronic assemblies and failures caused by them can be catastrophic and are highly undesirable. Hence it is very important to study about tin whiskers and understand their growth mechanisms as well as other properties to develop effective mitigation strategies.

2.1.2 Factors influencing whisker growth

Experts in the electronics and electroplating industry still have not reached a consensus upon a single accepted explanation of the mechanism(s) that drives whisker formation. Most researchers in the whisker research community agree that compressive stresses are necessary for Sn whisker formation [6, 25, 26] and that Sn whisker formation and growth observed to be mainly a stress relief phenomenon [27-33, 17]. However, there are some commonly accepted factors that are known to promote tin whisker formation.

2.1.2.1 Externally applied mechanical stress

Compressive stress in the Sn could be induced by externally applied mechanical stresses [5, 34 and 35] such as bending or stretching of the surface after plating, torqueing

of a nut/bolt assembly etc. Scratches in the plating introduced due to handling could also be the sites for whisker nucleation. To understand the mechanism of whisker formation by these mechanically induced compressive forces, experiments have been done by indenting the tin film and accelerating the induction of mechanical stresses in the film. It was observed by Suganuma et al. [36] that due to mechanical loads, compressive stresses are exerted in localized regions. Because of this stress, new grain structure results in the deformed region due to recrystallization. The plated columnar structures are no longer retained in the deformed region. Instead, flatter, more horizontal grain

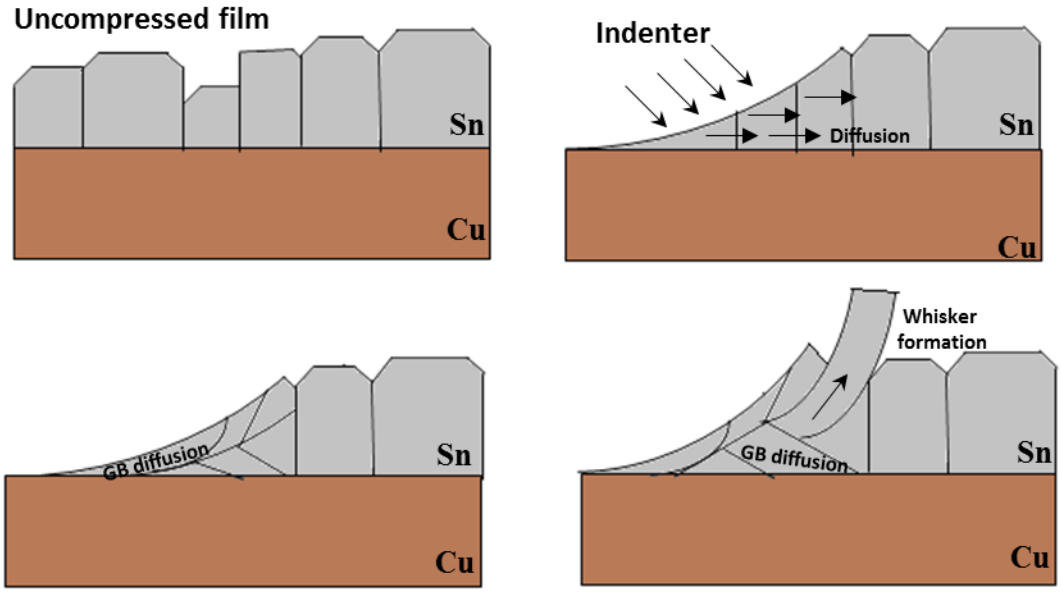

Figure 2. Schematic diagram showing the microstructure development in the deformed region [36].

boundaries are formed resulting in an equi-axed grain structure. These flatter grains have more diffusion paths which result in easy diffusion of tin atoms and result in whisker growth (Figure 2).

Williams et al. [37] monitored the growth of hillocks by *in situ* nanoindentation of tin films. Refs. [38], [39], [40] also performed indentation of the tin films and obtained whiskers for various studies. Figure 3 (a) and (b) show hillocks and whiskers obtained by indentation. Applying mechanical stress in Sn using an indenter is being successfully used as an accelerated growth technique to obtain whiskers and use them for several investigations.

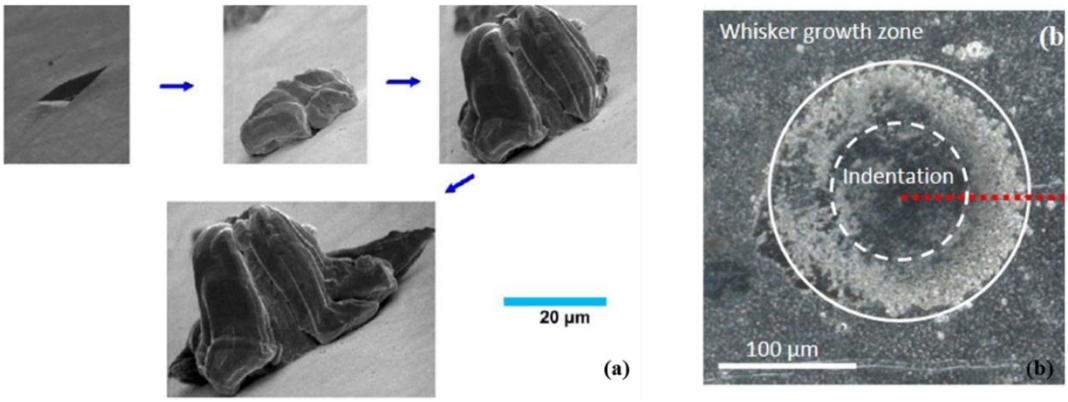

Figure 3. (a) in situ nanoindentation leading to tin hillock growth [37] and (b) Tin whiskers obtained by indentation [38].

2.1.2.2 Temperature

Intermetallic compound, a substance formed between tin plating and substrates by diffusion of copper species into tin films, followed by a solid-state reaction, has interested most of researchers on tin whiskers. A layer of Cu–Sn intermetallic compound (IMC) is seen to grow readily between the Sn and Cu layers at room temperature. The IMC grows on the Sn side of the Sn–Cu interface, nucleating preferentially at Sn–Sn grain boundaries [41, 42]. The growth of IMC into the Sn layer is consistent with interdiffusion measurements [43] showing that Cu diffuses much more rapidly into Sn

than Sn does into Cu. Under ambient conditions, the IMC grows in the Cu_6Sn_5 phase; the Cu_3Sn phase is only observed to form at temperatures above 80 °C [44, 45]. The development of compressive stress within tin film is thought to be related to the formation of this compound. Several analyses exist on how the formation of Cu_6Sn_5 would result in the development of compressive stress. Some researchers propose that the interstitial diffusion of Cu and formation of Cu_6Sn_5 may alter the lattice spacing in the Sn plating and generate compressive stress [45, 46]. Few others propose that the generation of compressive stress is due to the volume change. Cu_6Sn_5 occupies more volume than the tin it consumes, hence resulting in a compressive stress in the plating [47]. It is also suggested that the intermetallic growth is greater at the grain boundaries [48-50] until a certain temperature which results in a stress gradient driving diffusion. Additionally, rapid oxide formation at high temperatures eliminates surface vacancies and constrains vacancies creating compressive stress [51]. Tin whiskers nucleate and grow to relieve this stress. Diffusion readily occurs at elevated temperatures and results in the formation of intermetallic compounds, oxide rapidly. Therefore, temperature is one of the important factors to be considered in whisker growth studies. If diffusion and IMC formation contribute to whisker formation, it seems logical to suspect that elevated temperatures which encourage such processes will also increase whisker propensity. Most experimenters report that ambient temperatures of approximately 50°C [52] are optimal for whisker formation, while others report that equivalent specimens maintained at room temperature (22°C to 25°C) have grown whiskers faster [53]. Reportedly, whisker growth ceases at temperatures above 150°C [54] due to uniform distribution of intermetallics and no build-up of stress. Thermal cycling is also found to induce stress in the plating [55-57]

due to mismatch of coefficients of thermal expansions of different materials present. Increase in temperature will result in the generation of stress in many ways and promote whisker formation. Hence aging the Sn plated samples at high temperatures/ thermal cycling could be used as accelerated growth methods to obtain whiskers.

2.1.2.3 Grain size/film thickness

Most researchers agree that the tendency to form whiskers decreases as the thickness of the plating or the grain size increases [58-60]. Glazunova reported that thicknesses below 0.5 μm and above 20 μm were less prone to whisker formation while 2 μm-10 μm thicknesses showed maximum growth rate [61]. Schetty and Zhang have suggested thicknesses over 8 μm tend to be in the safer region [62, 63]. A decrease of whiskering with larger grain size has been noted by others [64], with the observation that fine-grained bright Sn has a greater propensity to form whiskers than larger-grained satin Sn. Xu & Zhang [63] verified the grain size effects on tin whiskers formation on three pure tin finishes: bright tin, matte tin and satin bright tin. Of the three finishes, bright tin has the finest grain size and is found to be much more prone to whisker formation than the satin bright and matte finishes. Diffusion of Cu and formation of Cu-Sn intermetallic compound at the grain boundaries results in the generation of compressive stress in the film. The thickness of the intermetallic formed is expected to decrease with increasing distance from the tin-substrate interface and the average compressive stress will decrease with increasing film thickness which in turn reduces whisker number density (Figure 4) [10]. Also, it has been hypothesized that thicker coatings tend to distribute the stresses more evenly, especially those originating at the substrate/plating interface [17].

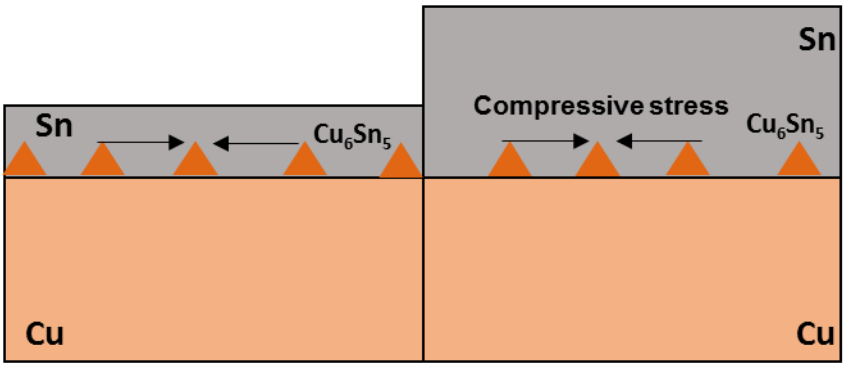

Figure 4. Effect of film thickness on the development of compressive stress: The average compressive stress decreases with increase in film thickness reducing whisker density [10].

2.1.2.4 Substrate effect

Whisker growth has been observed on different substrate materials commonly used in the electronics industry. Most researchers agree that brass and copper are the most sensitive due to Zn and Cu diffusion and formation of intermetallic compounds resulting in the build-up of the stress [65].

2.1.2.5 Crystal structure of the tin deposit

Kakeshita reported that the grain shape along with the size play significant roles in whisker propensity [66]. It is observed that equiaxed crystal structure of Sn is less prone to whisker formation than columnar structure [67]. Alloying additions such as Pb, Bi, Zn or Ag [68-71], can produce more equiaxed grain structures than the columnar structures which is why Pb-Sn coatings are found to be effective inhibitors of whisker growth. It is observed that equiaxed structures result in very controlled, evenly distributed and relatively thin IMC dissipating the stress resulting in no whisker formation [67].

2.1.2.6 Other factors

There are many other factors known to aid in whisker nucleation and growth apart from those mentioned above. The plating chemistry and process [62] influence the formation of whiskers and even slight modifications would largely vary the results. A higher current density during electroplating is known to produce a higher residual stress and promote whisker formation. Brighteners usually added to the electroplating bath result in a finer grain size of the plating and are known to aid in whisker formation. Environmental conditions such as moisture and humidity [54] are also found to accelerate growth of whiskers by forming corrosion products and oxides.

The initial objective in the current work was to obtain whiskers to utilize them for various tests. Understanding the growth mechanisms and factors affecting whisker growth will help in the selection of suitable accelerated whisker growth methods as well as other parameters. While several studies exist on the growth mechanisms, factors affecting the growth of whiskers, very few studies exist discussing their mechanical behavior. To completely understand the properties of tin whiskers and develop efficient mitigation strategies, it is essential to know the mechanical properties as well. Hence the current research work focuses on obtaining tin whiskers and understanding the mechanical behavior of these.

2.1.3 Mechanical behavior of tin whiskers

Limited studies on the mechanical behavior of Sn whiskers can be found in the literature for comparison with the current work. This can be attributed to the difficulty in

handling, gripping and testing such fine-diameter and high-aspect ratio whiskers. Dunn (Figure 4) [72] attempted to obtain elastic properties as well as tensile strength of tin whiskers. Tin whiskers were carefully plucked and were fixed on glass slides on one end. The dimensions of each projecting whisker were measured using an optical microscope. Gold wires were carefully slipped over the individual whiskers and the glass slides were then rotated so that each gold wire is made to hang on to the protruding whisker which is then stressed in the manner of a cantilever beam. A large variability in Young's modulus was observed (8 GPa to 85 GPa). In addition, the tensile strength was obtained by bonding whiskers with gold wire on a glass slide, suspending it and adding additional wires until it fractured. The strength value obtained was found to be very low (8 MPa). Some potential problems with these data include measurement of the whisker radius with an optical microscope and assuming that the cross-sectional area is circular. The assumption of circular cross-section of area would lead in an over-estimation of area and hence under-estimation of strength. Furthermore, in bending theory, the Young's modulus goes as the radius of the whisker to the fourth power, meaning that slight changes in radius could result in large errors in modulus.

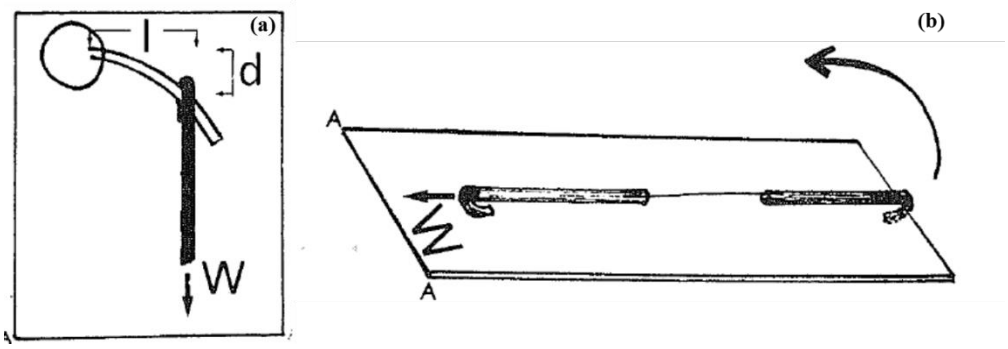

Figure 5. (a) Schematic illustrating the cantilever method of testing with a gold wire hanging on a whisker and (b) schematic showing a whisker bonded with gold wires for tensile test [72].

Powell and Skove [73] attempted to perform tensile tests on Sn whiskers by carefully removing them from a substrate and gluing the ends with diphenylcarbazide to a pulling apparatus. Force versus displacement curves were obtained, which were linear in nature, although the strength of the whiskers was not reported. Large variation in strain was found. Some other issues include manual handling of whiskers and no measurement of stress due to issues with measurement of cross-sectional area.

2.1.4 *In situ* tensile testing using MEMS

It is well known that mechanical response of materials varies with length scale and the properties of bulk materials cannot be directly extrapolated to the micro and nanoscale materials. Different deformation mechanisms are operative as the size is reduced and this results in a change in the mechanical behavior. Due to the increasing miniaturization of the devices, accurate characterization of micro/nano scale materials became increasingly relevant. The emergence of small scale technologies such as MEMS

enabled reliable prediction of properties at the micro/nano scale [74]. Utilizing these technologies and performing the mechanical tests *in situ* SEM/TEM/FIB-SEM etc. enabled to observe the deformation behavior in real time resulting in a better understanding of the mechanisms in small scale materials. Owing to the small size of the whiskers, MEMS can be a suitable platform for performing their tensile tests. Traditionally, free standing metal films are co-fabricated on the micro tensile devices. A recent study has utilized these devices and performed tensile tests on tin whiskers successfully. Whiskers are lifted-out using FIB and placed on the device to perform tensile testing *in situ* FIB/SEM [11]. Figure 6 shows the MEMS stage used, which is very similar to stages previously used to test freestanding thin films [75, 76] was fabricated using the process described in Refs. [77, 78]. The stage has built-in force and displacement sensors that allow simultaneous measurement of nominal stress and strain in the whisker during *in situ* deformation. As shown in Fig. 6(a), when the stage is loaded, the U-springs deform and apply uniaxial tension on the specimen. Fig. 6(b) and 6(c) show the gages. During loading, the deflection of the force-sensing beams, provided by the relative displacement of G1 with respect to fixed gage G0 (G_{01}), multiplied by their stiffness gives the force on the sample.

$$\text{Force (F, in } \mu\text{N)} = K_{total} * G_{01}\ (\mu\text{m}) \quad (1)$$

Where K_{total} is the stiffness of the two beams and $K_{per\ beam} = x.(E*I)/L^3$ and $I = (1/12) * b * h^3$

Where E is the modulus of the beam, I is the moment of inertia, L is the length of the beam, b is the height of the beam and h is the width of the beam.

The stress is calculated by dividing this force with area (A) calculated initially using FIB.

$$\text{Stress} = F/A \quad (2)$$

The elongation of the sample is given by the relative displacement of G2 with respect to G1 (G_{21}).

$$\text{Strain} = G_{21}/L_0 \quad (3)$$

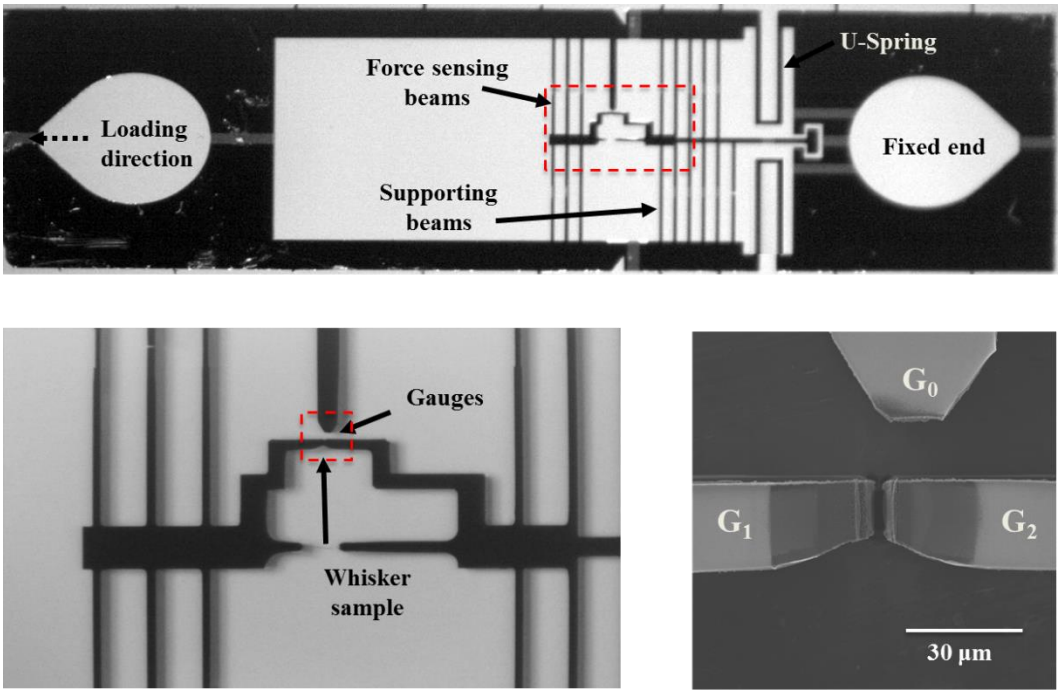

Figure 6. (a) Optical micrograph of the MEMS stage used for tensile testing of whiskers, (b) Zoomed view of the rectangular box in (a), showing the sample and force and displacement gages and (c) Scanning electron micrograph of the gages (Nanomaterials, mechanics and MEMS lab, ASU).

From the above-mentioned reports, it is evident that limited study has been done on the mechanical behavior of tin whiskers. There is a need for more research to be done

to understand the mechanical behavior of tin whiskers by conducting tests and trying to overcome the limitations of previously used methods. Since the whiskers are very fine and difficult to handle, new techniques must be developed to test them *in situ* avoiding manual handling. Tin whiskers will be obtained utilizing accelerated growth methods considering all the factors mentioned in the previous section and will be utilized for various tests. To understand the tensile behavior, a novel testing method *in situ* FIB/SEM utilizing MEMS tensile testing stage will be used. This method of testing provides more accurate and reliable results than previously available. This is because the MEMS load frame provides higher load and displacement resolution while the FIB cross sectioning allows for the high-resolution measurement of the whisker area required for accurate stress determination. Additionally, the possible damage associated with manual handling is eliminated by using an *in situ* micromanipulator. Singh et al. [11] utilized a similar method and reported the tensile strength values. But that study focused only on reporting the results from a limited number of tests. Hence the present study aims in providing the deformation behavior and post mortem TEM characterization on a wider array of whiskers, providing insight into the possible mechanisms of growth and deformation. *In situ* TEM studies and bending tests will also be performed. With the critical issues in mind regarding the studies carried out on mechanical behavior of Sn whiskers as mentioned above, this research work aims to achieve the following objectives:

1. Obtain tin whiskers by accelerated growth methods so that they could be used for tests to understand their mechanical behavior.

2. Perform tensile tests reliably *in situ* FIB/SEM overcoming the limitations of previous methods.

    - ✓ Understand the effect of varying parameters such as gage length and method of processing on the tensile strength of whiskers.

3. Understand the structure and mechanisms of deformation of tin whiskers in tensile tests and correlate with the strength.

2.2 Corrosion of aluminum alloys

Pure aluminum has low strength and hence alloying additions are added to improve its strength. The main alloying elements in Al are copper (Cu), zinc (Zn), magnesium (Mg), manganese (Mn) and silicon (Si). Based on the principal alloying element, wrought alloys are divided in to groups and designated by a four digit numerical system developed by the aluminum association: 1xxx (no alloying elements), 2xxx (Cu is the principal alloying element), 3xxx (Mn is the principal alloying element), 4xxx (Si is the principal alloying element), 5xxx (Mg is the principal alloying element), 6xxx (Mg and Si are the principal alloying elements), 7xxx (Zn is the primary alloying element), 8xxx (other elements eg. Lithium (Li)), 9xxx (unused) [79, 80]. The 7xxx series alloys are widely used due to their high strength to weight ratio. They comprise more than 80% of the weight of the aircraft [81-83]. Intermetallic particles are observed within Al alloys and they can be classified in three types [84]: (i) precipitates (ii) inclusions and (iii) dispersoids. Precipitates are formed by nucleation and growth from a supersaturated solid solution during low temperature aging and they are observed to be concentrated along the

grain boundaries. Inclusions are observed in the aluminum alloys which are formed from impurities and alloying elements reacting during the casting process [85]. In commercial Al 7075 alloys, the predominant types of inclusions are Al_7Cu_2Fe and Mg_2Si [80, 86 and 87]. Dispersoids form by low additions of highly insoluble elements such as Cr, Mn or Zr [84]. Although these alloys possess good mechanical properties, they can undergo localized corrosion such as pitting, exfoliation corrosion, intergranular cracking, stress corrosion cracking crevice corrosion depending on the environment [88].

The basic reactions comprising corrosion of aluminum are [84]:

Anodic reaction: metal dissolution

$$Al \rightarrow Al^{3+} + 3e^- \quad (4)$$

Cathodic reaction: oxygen reduction or hydrogen reduction

$$O_2 + 2\ H_2O + 4e^- \rightarrow 4\ OH^- \quad (5)$$

$$2\ H^+ + 2e^- \rightarrow H_2 \quad (6)$$

Al alloys are usually resistant to corrosion due to the passive oxide layer that forms on them. This layer acts as a barrier protecting the underneath metal from getting corroded. But in certain aggressive environments such as Cl^- containing environments, this passive layer breaks down resulting in extensive corrosion of Al. Many applications which use Al, for eg., aircrafts that are frequently used in marine environments, encounter interaction with Cl^- ions and undergo corrosion. To understand such effects, many experimenters perform corrosion studies in 3.5 wt.% NaCl solution to replicate the effect

of sea water and corrosion products, pits are extensively observed in these samples. On application of stress, these might be the regions where stress concentrates resulting in crack initiation leading to stress corrosion cracking. Hence, these might have a deleterious effect on the performance of the Al alloys and need to be completely characterized to be able to better design alloys that are corrosion resistant.

2.2.1 Characterization of the pits

It has been reported that the oxide film on aluminum can readily undergo corrosion reactions in chloride environments [89, 90] and the film breaks down at specific points leading to the formation of pits on the aluminum surface. This type of corrosion is known as pitting corrosion [91-93]. The pits are like discontinuities in the sample and can act as sites for stress concentration resulting in crack initiation. Pitting is the precursor to stress corrosion cracking (SCC) [94] and origin for fatigue crack nucleation [95-97]. From the above, the determinantal effect pits might have on the mechanical performance of the alloy is evident. Therefore, it is necessary to characterize the pits and understand their effect on the mechanical performance of the alloy. Several studies have been performed in aluminum alloys to visualize pits and understand their effect on the mechanical performance of the alloy, especially fatigue strength. But in most of the studies, optical microscope or SEM were used to observe the pits [98-101]. D.L DuQuesnay et al. studied the growth behavior of fatigue cracks initiated at corrosion pits. They corroded 7075-T6511 alloy in EXCO solution and performed fatigue tests. The corrosion pit depths were utilized as a metric to predict the fatigue life. The sizes of the pits were measured from the images taken by an optical microscope. A similar study was

performed by K. K. Sankaran et al. on Al 7075 T6 alloys corroded by prohesion spray. They measured pit depths by imaging specimens with an optical microscope to get the pits growth rate and to predict the fatigue lives. Hosni Ezuber et al. observed the shape and morphology of the pits in AA5083 and AA1100 alloys corroded in sea water with optical photographs. Two-dimensional (2D) approach is often inadequate and would result in limited information regarding the pits. To get a thorough understanding of the nature of the pits, its dimensions and correlate the microstructure with the mechanical properties, it is necessary for three-dimensional (3D) studies. X-ray tomography is an excellent technique for this purpose. It is advantageous owing to its non-destructive approach to examine microstructures and high spatial, temporal resolution. Since it is nondestructive, microstructure evolution with time can also be studied. X-ray tomography follows Beer-Lambert law, given by [102]:

$$I = I_0 \exp [(-\mu/\rho)\, \rho x] \quad (4)$$

Where I_0 is the original intensity of X-rays from the source, I is the intensity of the beam when it has travelled a distance x in to the material, μ is the attenuation coefficient and ρ is the density of the material. The object is rotated in pre-defined increments and images are collected at each angle (also called projections). The collected projections are reconstructed using algorithms such as filtered back projection algorithm to obtain the 3D microstructure. Recently, this technique is being extensively used to study the corrosion behavior and its effect on the mechanical behavior of Al alloys in three dimensions [103-108]. Sudhanshu S. Singh et al. studied the localized corrosion rates at inclusion particles, corrosion fatigue and high humidity stress corrosion cracking in Al 7075 alloys using *in*

situ 3D X-ray synchrotron tomography. Y. Nakai et al. measured the shape and dimensions of the pits and cracks formed in corrosion fatigue tests of Al 7075-T651 alloy using computed tomography. S. P. Knight et al. used X-ray tomography to assess the depth and volume of corrosion as a function of time and humidity in AA2024-T351 and 7050-T7451 alloys. T. J. Marrow et al. studied localized corrosion and intergranular cracking in sensitized 5083 Al alloy using high resolution synchrotron X-ray tomography. Utilizing this technique to characterize the corroded region will result in the following advantages:

1. Visualization of the 3D microstructure of the pits
2. Accurate quantification of the dimensions of the pits
3. Correlation of the microstructure with the mechanical properties
4. Microstructural data sets can be incorporated in to models to elucidate the effect of microstructure on the deformation behavior of Al alloys

2.2.2 Characterization of the corrosion layer

In certain medium for e.g. containing chloride ions, the passive oxide film on Al loses its protective nature and can readily undergo various corrosion reactions [109-115]. Due to the reactions, the surface of the specimens will no longer be Al and will be replaced by a corrosion product layer. The pits and corrosion product layers resulting from the corrosion can be sites for stress concentration; hence corrosion is known to have a severe effect on aluminum alloys life resulting in their catastrophic failure, and they are also known to be highly susceptible to stress corrosion cracking (SCC) [116, 117].

Therefore, it is important to understand the properties of the corrosion product layer also apart from the pits.

Apart from a surface corrosion layer, a diffuse layer beneath it has also been observed in Magnesium alloys corroded in NaCl environments [118, 119]. This diffuse layer is known to be partially corroded and forms because of the diffusion of NaCl beyond the surface corrosive layer. Shumin li et al. studied about identification of this diffuse corrosive layer and studied its chemical composition, mechanical properties in Mg alloys. The presence of two layers of corrosion film in 7075 aluminum has also been reported [120]. It is important to identify and characterize this layer to better understand the corrosion mechanisms in Al. EDX and nanoindentation techniques can be used to understand the localized variation in the composition and mechanical properties.

Over the years, nanoindentation has emerged as an excellent technique to obtain mechanical properties in small length scales [121]. The basic components of an instrumented tester and a typical load-displacement curve [122] obtained from nanoindentation can be seen in Figures 7 and 8.

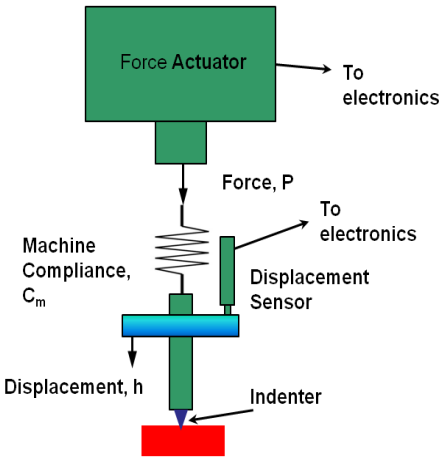

Figure 7. Basic components of an instrumented indentation tester [122].

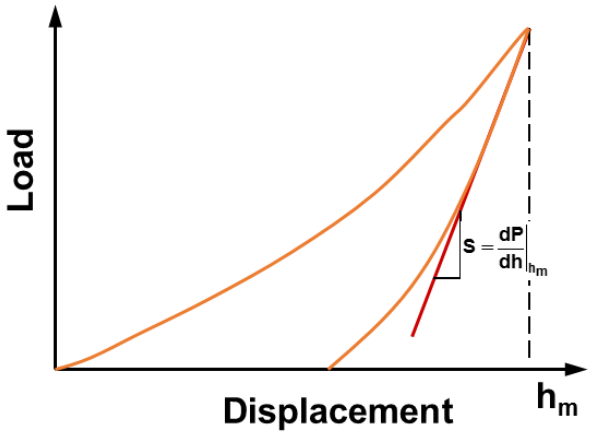

Figure 8. Typical load-displacement curve obtained from nanoindentation [122].

Reduced modulus (Er) and elastic modulus (E) of a material can be obtained from the following equations [123]:

$$E_r = \frac{\sqrt{\pi}}{2\beta}\frac{S}{\sqrt{A}} \tag{6}$$

$$\frac{1}{E_r} = \frac{1-\nu^2}{E} + \frac{1-\nu_i^2}{E_i} \tag{7}$$

Where E and υ are the Young's modulus and Poison's ratio of the material and E_i and υ_i are those for the indenter. A is the contact area and β is the indenter geometry factor. Hardness (H) is calculated as the ratio of load to contact area:

$$H = P/A \tag{8}$$

Where P is the load at maximum displacement.

Recently continuous stiffness measurement technique has emerged as a better technique than the conventional one. In this method, instantaneous measurement of stiffness is achieved by superimposing a small dynamic oscillation on the force signal (Figure 9) [124]. This results in a continuous measurement of properties (Young's modulus and hardness) as a function of depth. The contact stiffness is given by:

$$S = \left[\frac{1}{\frac{f_o}{h_o}\cos\Phi - (K_S - m\omega^2)} - K_f^{-1} \right]^{-1} \tag{9}$$

Where f_0 is the force amplitude, h_0 is the displacement amplitude, ω is the frequency of oscillation, ϕ is the phase angle between displacement and force, K_f is the frame stiffness, K_s is the spring constant of leaf springs supporting the indenter and m is the mass of the indenter. Force amplitude, displacement amplitude and phase angle are continuously measured and in this way contact stiffness is obtained. From this, the reduced modulus and Young's modulus can be obtained from equations 6 and 7.

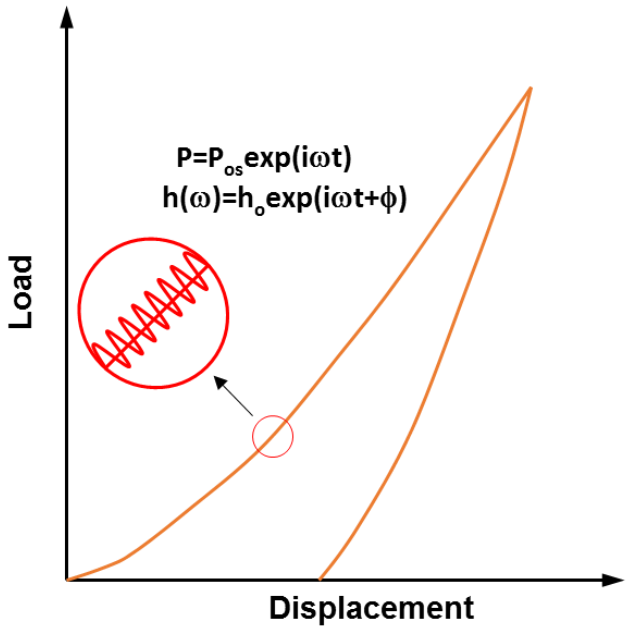

Figure 9. Schematic of CSM technique showing a small harmonic load superimposed [124].

With the critical issues in mind regarding the studies carried out on characterization of corroded region in Al alloys as mentioned above, this research work aims to completely characterize corroded region in Al and achieve the following objectives:

1. Understand the effect of corrosion on the tensile strength
2. 3D visualization of pits and accurate quantification of their dimensions with corrosion
3. Correlation of the microstructure with the mechanical strength
4. Identification and characterization of the partially corroded region

CHAPTER 3

IN SITU FIB/SEM TENSILE TESTING OF TIN (SN) WHISKERS

3.1 Introduction

Restricted usage of Pb in electronic products due to its toxicity has resulted in electronic suppliers moving towards the usage of pure Sn [1]. However, the usage of pure Sn and high Sn based coatings without Pb has resulted in a reliability concern regarding the formation of conductive tin whiskers. These tin whiskers are thin filaments known to grow spontaneously from Sn which can lead to short-circuits and system failures [2]. Hence, an understanding of the properties of tin whiskers and growth mechanisms is important. This study focuses on understanding the tensile behavior of tin whiskers.

The exact mechanisms for whisker nucleation and growth are unknown but most researchers in the whisker research community agree that compressive stresses are necessary for their formation [3-5]. Compressive stresses can be induced by mechanical, chemical and thermal effects [6]. These can be internal stresses arising due to various reasons such as residual (or plating) stress [7, 8-10], intermetallic growth [11, 12, 13-15], oxidation and corrosion [16] etc. resulting in whisker formation. They can also be induced by external pressure which was found to accelerate the growth of Sn whiskers [17]. In the present study, tin whiskers for the tests were obtained by the introduction of compressive stress by two methods: indentation and high temperature furnace aging. The sources of compressive stress and the grain structures were investigated in each of these cases.

While the phenomenon of Sn whiskering has been studied for decades, very little is known about the mechanical properties of these. Very few studies have been conducted on the mechanical behavior of Sn whiskers owing to the difficulties of handling, gripping, and testing such fine-diameter and high-aspect-ratio whiskers [18]. Powell and Skove [19] performed tensile tests on tin whiskers and obtained force vs. displacement curves although the strength was not reported. Dunn [20] attempted to obtain bending stiffness of Sn whiskers and reported young's modulus values with large variability. Manual handling of whiskers, assumption of a circular cross-section and measuring the radius with optical microscopy as done in previous studies can result in significant experimental uncertainty and erroneous results. From the above-mentioned reports, it is evident that more research needs to be done to understand the mechanical properties of whiskers. Recently, Singh et al. [18] utilized a novel method *in situ* FIB/SEM for testing tin whiskers. This method of testing provides more accurate and reliable results than previously available. This is because the MEMS load frame provides higher load and displacement resolution while the FIB cross sectioning allows for the high-resolution measurement of the whisker area required for accurate stress determination. Additionally, the possible damage associated with manual handling is eliminated by using an *in situ* micromanipulator. While that study focused only on reporting the results from a limited number of tests, the present study provides the deformation behavior and post mortem TEM characterization on a wider array of whiskers, providing insight into the possible mechanisms of growth and deformation. In the current work, Sn films were electrodeposited on Cu disks and whiskers were obtained by two different accelerated growth methods as previously mentioned. These were then tested *in situ* FIB/SEM at two

different gage lengths: 20 µm and 50 µm utilizing a microelectromechanical system (MEMS) tensile testing stage. An attempt was made to understand the effect of gage length and method of processing on the strength of whiskers. To understand the effect of processing on the strength of the whiskers, the possibility of difference in oxygen contents on the two types of samples was investigated and subsequently TEM analysis was done. Possible mechanisms of deformation in tin whiskers from the TEM results were also discussed.

3.2 Experimental Procedures

3.2.1 Electroplating

Oxygen-free Cu rod (alloy 101, Rockwell F84-94, 9.5 mm diameter) was cut into 3-mm-thick disks with an electric discharge machine (EDM) to use as the Sn plating substrate and were then ground, polished to a 0.05-µm finish. After polishing, the disk was ultrasonically cleaned in ethanol and dried before being placed in the electrolytic cell. The Cu disc was used as the cathode, and a Sn strip polished and cleaned similarly was used as the anode. The initial objective of this work was to grow whiskers on these electroplated samples so that these whiskers could be used for testing and further analysis. Since it is known that bright Sn plating has more propensity to whisker formation [21, 22], a sulfate based electrolyte with commercial brightening agents (Electrochemical Products Inc., E-Brite 180) was used. Thin (less than 5 µm) layer of electrodeposited Sn was preferred than thick coating since it has been noted by others [23, 24, 25] that thicker coatings tend to have fewer whiskers and the electroplating time, along with other plating parameters were adjusted accordingly. Plating was achieved in a

vertical PTFE reactor with cathode current density of 212 A/m^2 for 5 min. Based on profilometry (Bruker Dektak XT) measurements, the thickness of the Sn plated films was found to be approximately 2- 4 µm. After plating, the samples were rinsed with water and given a light polish ensuring minimum damage to the Sn film surface.

3.2.2 Accelerated whisker growth

Sn whisker formation and growth was observed to be mainly a stress relief phenomenon [26-31, 32, 33]. Accelerated whisker growth in this study was achieved by the introduction of compressive force in the Sn film by two different methods: indentation and high temperature furnace aging. To relieve this compressive stress induced in the tin film, formation of tin whiskers and hillocks (low aspect ratio whiskers) has been observed.

The samples were indented for a period of 3 days with a custom-made indentation apparatus consisting of 300 g weight and a tungsten-carbide ceramic ball glued to the center of the bottom face of the weight similar to the one shown in [34]. Also, another set of Sn plated samples were aged at 100 °C in a laboratory furnace for about 30 days.

Both the indented and aged samples were checked periodically in a SEM (JEOL JSM-6100 SEM) for whisker and hillock growth. Focused ion beam cross-sectioning was performed on both type of samples to understand the sources of stress and the underlying mechanisms for whisker/hillock growth. A dual-beam focused ion beam (FIB) with a scanning electron microscope (Nova 200 NanoLab FEGSEM/FIB, FEI Co, Oregon) was used in this study. Cross-sectioning was performed by milling a trench starting with a

current of 7 nA and subsequent polishing of the cross-sectioned surface using finer currents till 50 pA. Ion-channeling imaging was also performed in the cross-section to reveal the grain structure.

3.2.3 Testing of Sn whiskers

The whiskers obtained by the above-mentioned methods were utilized for testing and the procedure is mentioned below. Straight whiskers were chosen and their initial area was measured by cross-section of the whisker tip, imaging using FIB/SEM and later correcting this image for the 52° angle at which it was taken. The area was obtained by manually outlining using the image-processing software (ImageJ, Bethesda, MD) and image segmentation was conducted to quantify the actual cross-sectional area of the whisker accurately (Figure 10).

Since the whisker needs to be placed on the MEMS device for testing, trenches of appropriate dimensions matching the dimensions of the whisker were milled on the MEMS device for the whisker to sit firmly (Figure 11). Initial cross-sectioning of the whisker for area calculations also helped in knowing the dimensions of the whisker precisely and the trenches were milled accordingly using the FIB. Small fiduciary marks were also made on the device beside the trenches which were used to track the load and displacement during the test.

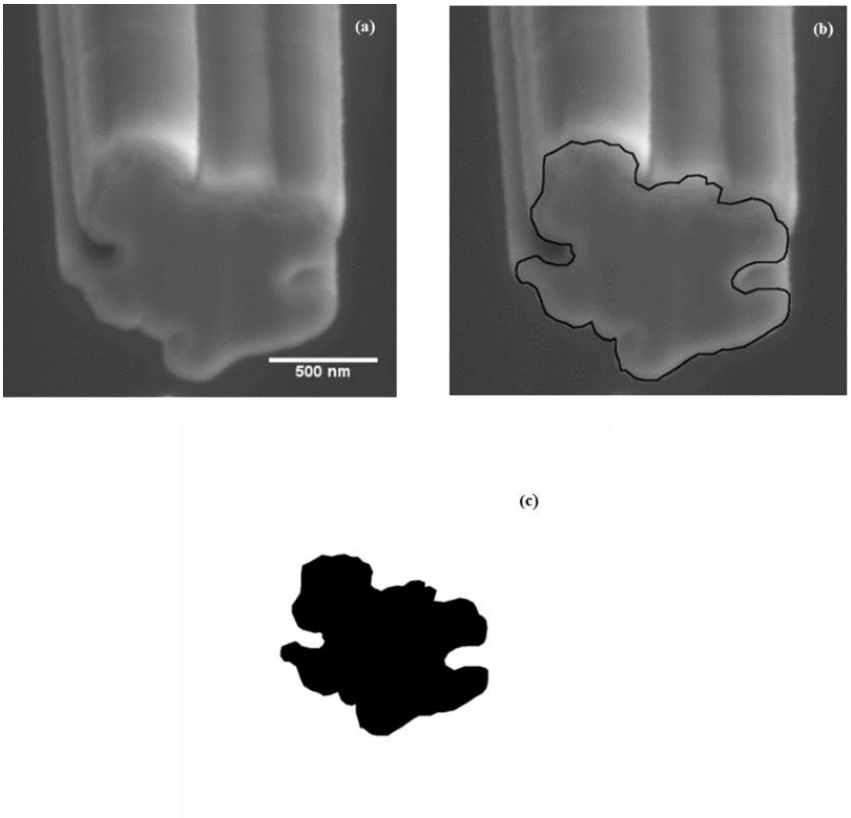

Figure 10. Measurement of cross-sectional area: (a) Whisker cross-section, (b) Outline of the boundary area and (c) Conversion in to binary image to measure the area in Image J.

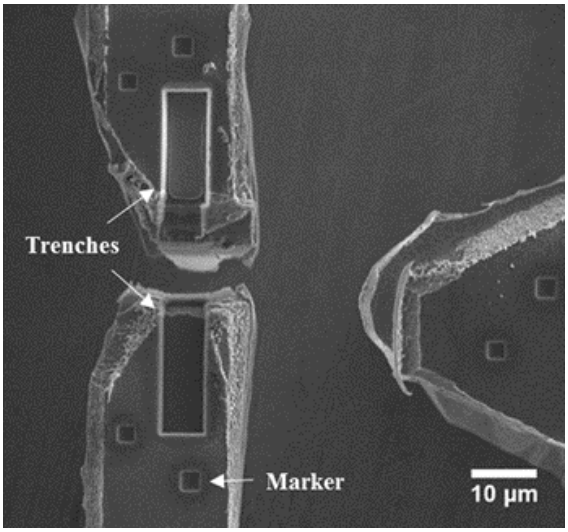

Figure 11. Trenches and markers milled on the MEMS device.

The process by which Sn whiskers were tested in this study is like the one described in Ref. [18] and is shown in Figure 12. A tungsten needle was welded to a Sn whisker in FIB/SEM by depositing platinum to glue the needle and the whisker (Fig. 12(a) and (b)) and FIB was then used to cut the Sn whisker (Fig. 12(c)). The needle was moved to the trench in the MEMS device, and Pt was again used to weld the whisker in the trenches. The FIB was then used to cut the needle from the whisker (Fig. 12(d), (e)).

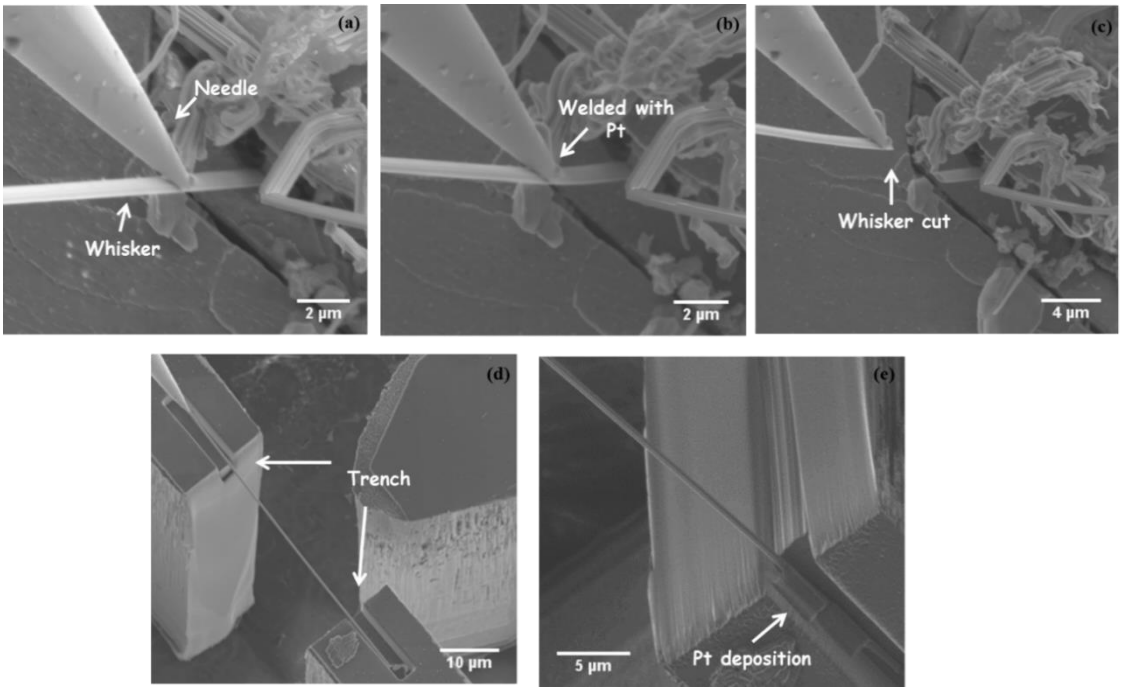

Figure 12. Process of whisker lift-out and placement on the device inside the FIB/SEM: (a) Needle touching the whisker, (b) Welding of the whisker to the needle using platinum, (c) Cutting the whisker near welded region using FIB, (d) Placement of Sn whisker inside the trenches made in the device and (e) The whisker is welded in place using Pt in both the trenches.

After welding, the whisker was deformed in a quasistatic manner by loading the MEMS stage using a piezo actuator with displacement resolution of 30 nm. The MEMS

stage, which is very similar to stages previously used to test freestanding thin films [35, 36] was fabricated using the process described in Refs. [37, 38]. The stage has built-in force and displacement sensors that allow simultaneous measurement of nominal stress and strain in the whisker during *in situ* deformation. Alignment beams and U-springs ensure alignment of the sample with the loading axis. Precision alignment of the whisker in the MEMS stage resulted in accurate measurement of the stress–strain behavior. Furthermore, the MEMS stage is designed to ensure uniform uniaxial loading of the whisker and to minimize any bending or torsion that could arise from loading misalignment [39]. During testing, one end of the MEMS stage was fixed and displacement was imposed on the other end in increments of about 150 nm by gradually increasing the voltage on the piezo. After each loading step, the whisker was allowed to relax for some time and the elongation and force were recorded. This process was repeated until the whisker fractured. The elongation and force on the whisker were used to calculate the strain and stress on the whisker using its length and initial cross-sectional area.

3.2.4 Oxygen detection

To study the oxygen content variation with the processing method and relate it to the strength of whiskers, a qualitative comparison using energy dispersive spectroscopy (EDS) in an electron microprobe (JXA-8530F, JEOL) was made on both indented and aged samples. EDS analysis was performed on tin whiskers, tin hillocks and the surfaces of tin plating as shown in Figure 13. FIB cross-sectioning to observe the different layers present and composition analysis by depth profiling using X-Ray photoelectron

spectroscopy (XPS (VG 220i-XL)) were also performed to further understand the EDS results.

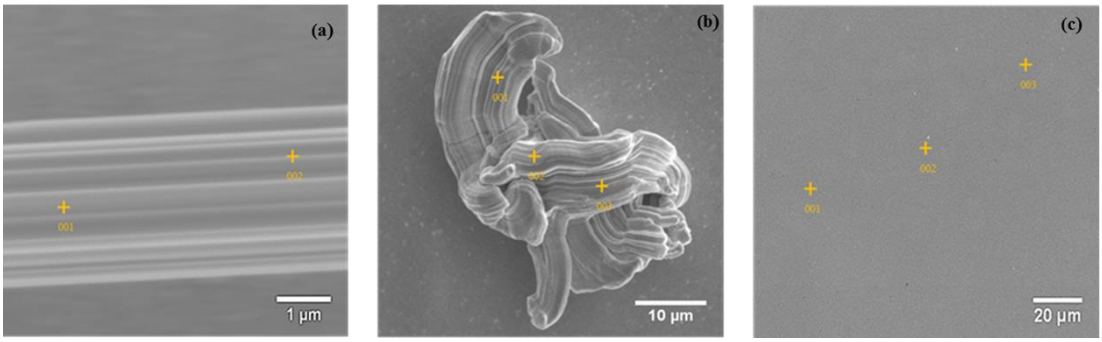

Figure 13. EDS spot analysis: (a) Whisker, (b) Hillock and (c) Surface.

3.2.5 TEM analysis

The objectives of the TEM analysis in the present study are twofold: (1) To understand the mechanisms of deformation in tin whiskers and (2) to understand the effect of processing on the variability observed in the strength between the two kinds of whiskers. TEM samples were prepared using the FIB lift-out technique. These samples were made from both as-grown whiskers as well as deformed whiskers of both types. A part of the whisker was cut using FIB and lifted-out using an *in situ* nanomanipulator to place it on a standard TEM Cu grid. This was later thinned down to electron transparency using a fine current at an accelerating voltage of 10 KeV. Thinning was carried out in two ways such that samples were made along the growth direction of the whisker and also perpendicular to it (cross-section) as shown in Figure 14. TEM investigation was performed in a JEOL

2010F microscope operating at 200 kV using a double-tilt holder for convenient dislocation imaging.

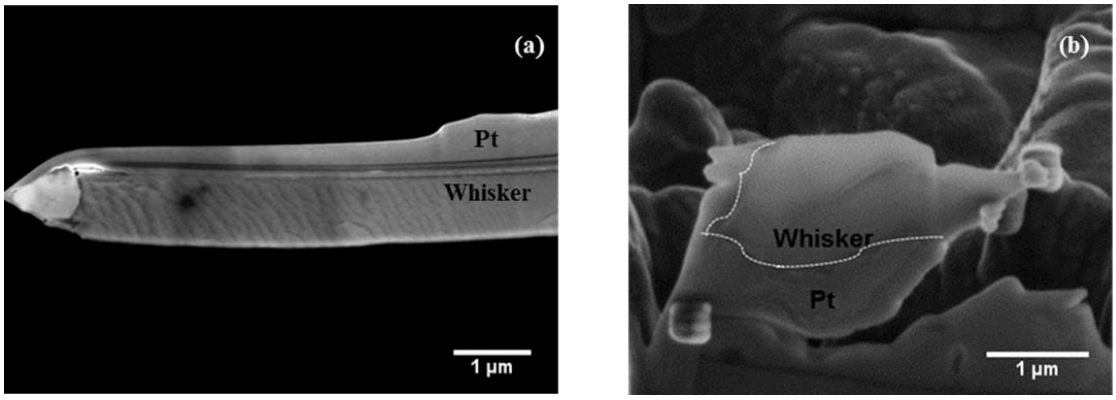

Figure 14. Images showing the two types of TEM samples made: (a) Sample made along the growth direction of the whisker and (b) Sample made perpendicular to the growth direction (as a cross-section).

3.3 Results and Discussion

3.3.1 Accelerated whisker growth

Figure 15 (b) shows the top view of the electroplated Sn film compressed for 3 days with the indenter described previously. Whiskers were observed at the boundary between the deformed (by the ball indenter) region and the un-deformed region and Figure 15 (a) represents a magnified view of one such whisker. Typically, whiskers obtained using this method were 10 - 70 µm long and 0.6 - 3 µm thick. Similar results were obtained by Doudrick et al. [34] and Williams et al. [40] who observed whiskers and hillocks respectively by indentation. Cross-section followed by ion channeling imaging was performed using the FIB in the un-deformed region (Figure 15 (c)) as well as the deformed region (Figure 15 (d)) of the Sn plating. Plated columnar grain structures

could be seen in the un-deformed region whereas equi-axed grains resulting from the deformation and recrystallization could be observed in the deformed region. This change in grain structure in the deformed region might provide more diffusion paths for the atoms and result in the accumulation of Sn atoms at the interface of the deformed and un-deformed region and subsequent growth of the whisker as discussed in Ref. [41].

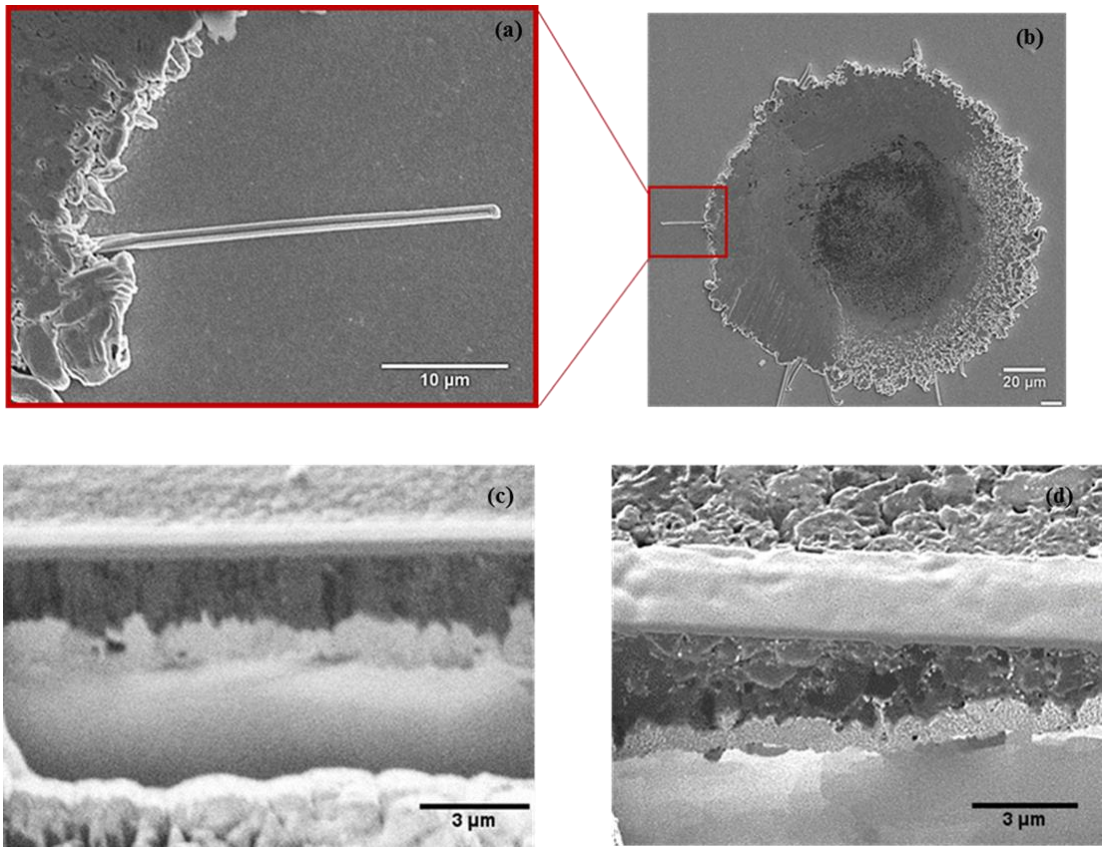

Figure 15. (a) Magnified image of a whisker obtained by the method of indentation and (b) Top view of an indent showing whiskers at the boundary between deformed and un-deformed region. Images of the cross-section obtained using FIB after ion-channeling: (c) Un-deformed region showing columnar grain structure and (d) Deformed region showing equi-axed grain structure.

Figure 16 (a) and (b) represent Sn whiskers and hillocks obtained by aging the electroplated samples at high temperature (100 °C). Typically, hillocks were observed after about 10 days of aging and the density of these hillocks increased with aging time. Most whiskers were found to form from these hillocks after about 20 days of aging with very few whiskers forming directly from the Sn plated surface. The protrusion of whiskers from hillocks was observed as a result of the tendency to reduce the surface-free energy of hillocks [42]. Typically, whiskers obtained by high temperature furnace aging were 10 µm -280 µm long and 1 µm -10 µm thick. Intermetallic compound formation between Sn and Cu at the interface is likely to be one of the primary reasons behind introduction of compressive stress in aged samples. This compressive stress in Sn is thought to be due to the volume increase by the growth of the intermetallic compounds [43] (Figure 16 (c)). Extensive intermetallic growth was observed in the aged samples as shown in Figure 16 (d) with two distinct, uniform layers of Cu-Sn intermetallic compounds namely Cu_6Sn_5 and Cu_3Sn.

Striations were observed on the surface of most whiskers obtained by both the methods along the growth direction which is a characteristic feature often observed for extruded whiskers [44, 45].

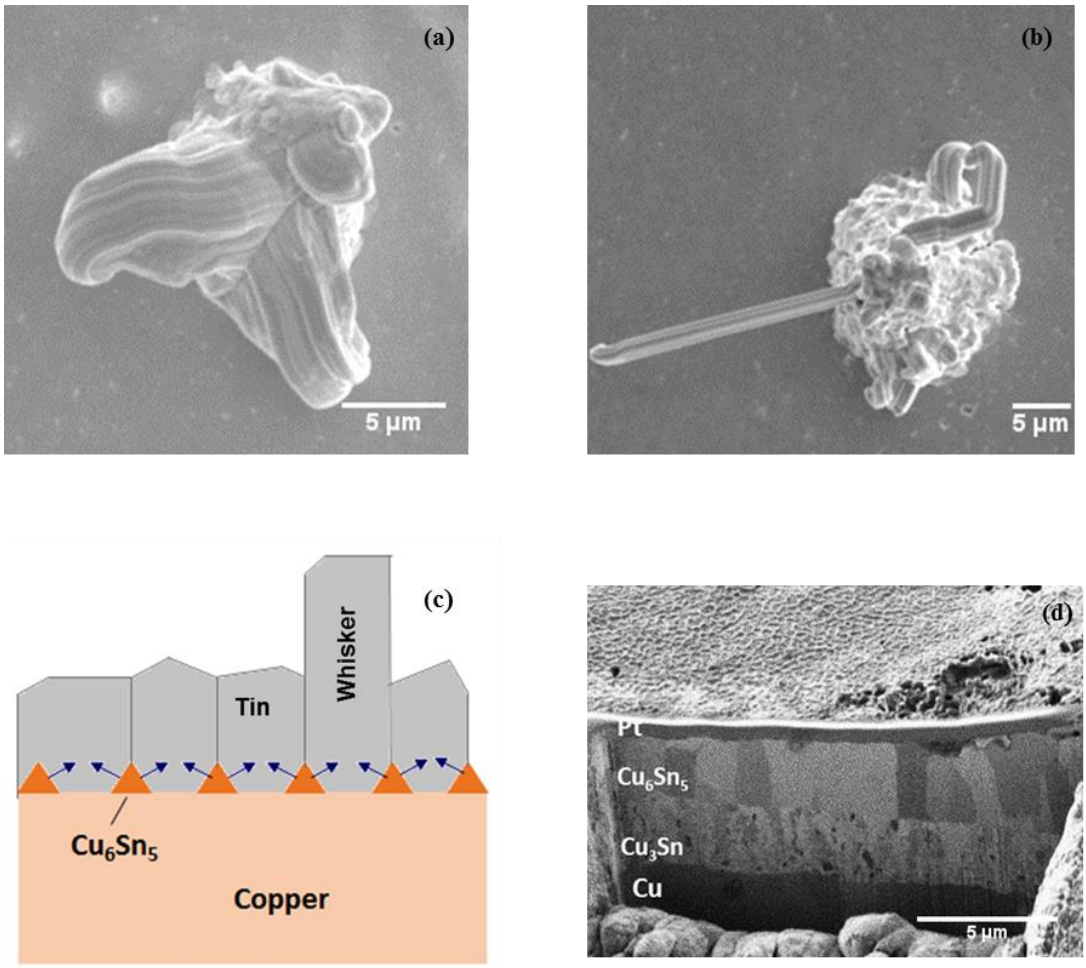

Figure 16. Whiskers and hillocks on aged sample: (a) Hillock, (b) Whisker from the hillock, (c) Schematic showing intermetallic formation at Cu-Sn interface and (d) FIB cross-sectional image after ion-channeling of an aged sample showing two distinct intermetallic layers of Cu_6Sn_5 and Cu_3Sn.

3.3.2 Tensile testing of Sn whiskers

High strengths of tin whiskers have been observed compared to bulk tin which could be attributed to low defect density compared to bulk materials and different deformation mechanisms operative as the size is reduced. Multiple whiskers tested at each condition produced similar strength values indicating the reliability and repeatability

of the testing method. For the range of whiskers tested, the mean strength values ranged between 250 MPa-860 MPa and the stress-strain curves of both the types were found to be fairly linear till the point of fracture. It was observed that the strength of the whiskers decreased with an increase in gage length i.e. for a particular type of whisker, the strength of the whiskers tested at 50 μm gage length showed lower strength than the whiskers tested at 20 μm gage length as shown in Fig. 17 (a) and (b). One possible explanation for this observed strength difference is flaw dependent fracture. In smaller volumes of material there is a lower probability of the material containing a strength limiting flaw, leading to a higher apparent strength. Quantitatively characterizing this type of effect with Weibull statistics requires testing multiple samples with identical volumes, which is not possible due to the large variations in cross sectional area between different whiskers. Also, at a particular gage length, it was observed that the whiskers obtained by high temperature furnace aging showed lower strength than the whiskers obtained by indentation as shown in Fig. 17 (c) and (d). This indicates that the behavior of whiskers is dependent on the growth mechanism and their properties and deformation mechanisms cannot be generalized. Possible explanations for the lower strength of whiskers obtained by high temperature aging are discussed in the following sections.

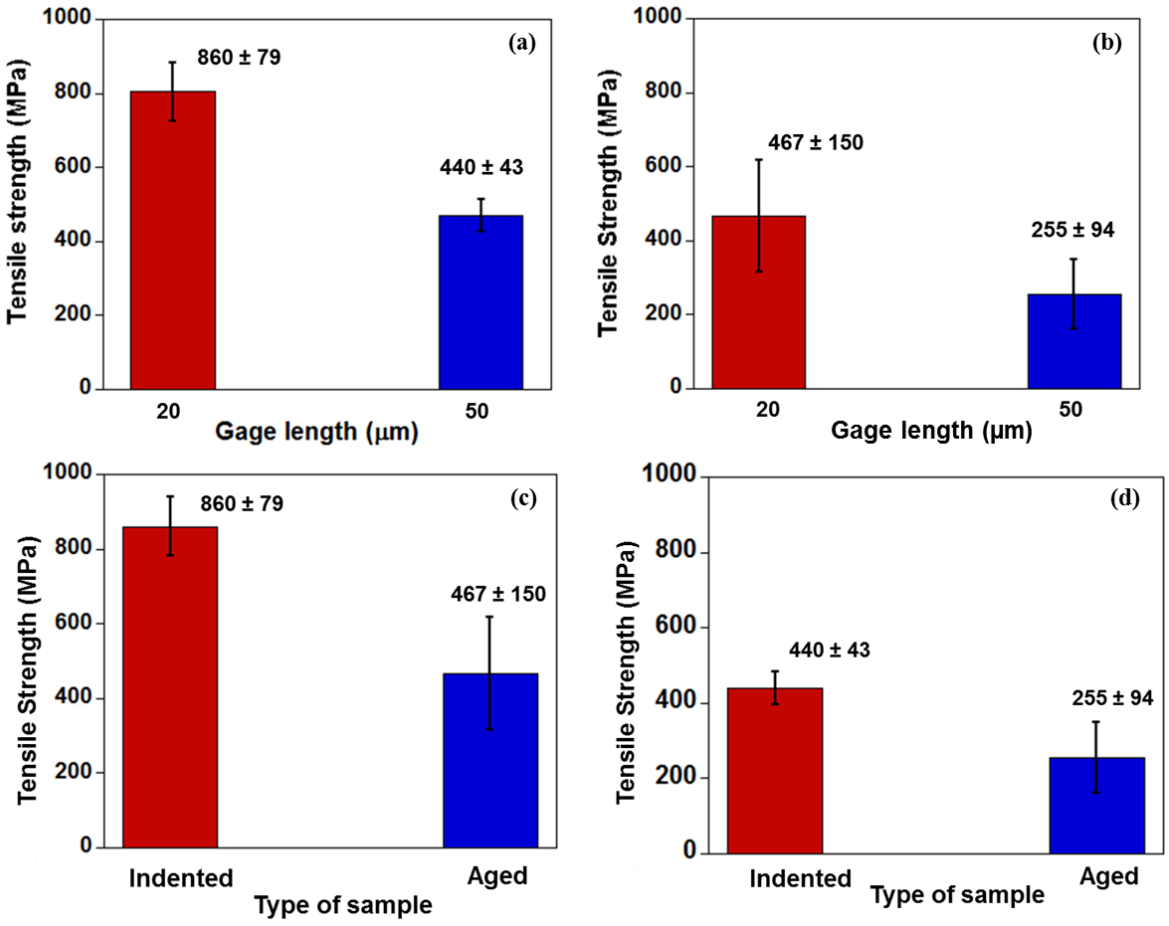

Figure 17. The effect of gage length on the strength of whiskers: (a) For whiskers obtained by indentation and (b) For whiskers obtained by high temperature furnace aging. The effect of processing on the strength of whiskers: (c) For whiskers tested at 20 μm gage length and (d) For whiskers tested at 50 μm gage length.

3.3.3 Role of oxygen on the strength of whiskers

One of the possible causes for the observed processing effect on the strength of whiskers was expected to be due to the possibility of higher oxygen content on samples exposed to high temperatures compared to the indented ones. From the EDS analysis

(Fig. 8), it can be observed that the oxygen content on whiskers and hillocks was similar for both processing methods. The oxygen content on the whiskers and hillocks obtained by indentation at room temperature was around 2 wt. %. Even after aging at high temperature (100 °C) for about 30 days, oxygen content did not vary much and remained in the similar range. This indicates that the tin oxide formed initially is tenacious and the rate of tin oxide growth is not significant upon exposure to elevated temperatures as also indicated by [46]. From this result, it can be seen that the lower strength of aged whiskers cannot be attributed to greater oxidation.

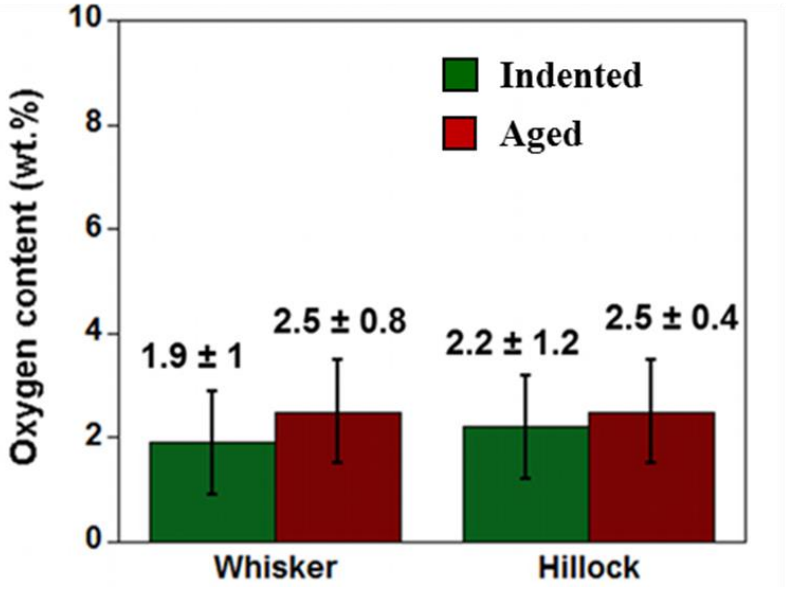

Figure 18. EDS analysis showing the variation of oxygen content on whiskers and hillocks.

While the oxygen content on whiskers and hillocks was found to be similar for both indentation and aging, a huge variation in oxygen content was observed on the tin

surface. The oxygen content was found to be much higher on the tin surface of aged samples compared to the indented. To understand this result, FIB cross-sectioning (Fig. 6 (d)) and XPS analysis were utilized. From Fig. 6 (d), it can be observed that the top-most layer is Cu_6Sn_5 and no longer Sn. Also, the XPS depth profiling results indicated presence of Cu from the start of the profile i.e. Cu is present on the surface along with Sn. Intermetallic compounds initially form at the interface of the Sn plating and Cu substrate and grow until eventually all the tin is consumed as stated by Ref. [47]. This consumption of tin and conversion to intermetallics takes place rapidly by high temperature aging and the surface of the aged samples is intermetallic and no longer tin as shown by FIB cross-section and XPS results. We believe that the higher oxygen content on the surface shown by EDS results is because of the contribution from both Cu and Sn on the surface.

3.3.4 TEM analysis

The as-grown indented whiskers were found to be free of any defects. Post-mortem TEM characterization also showed absence of stored dislocations in fractured whiskers (Fig. 9 (a), (b)). High strengths observed of the indented whiskers could be attributed to the requirement for nucleation of dislocations for the deformation to proceed in such defect free structures.

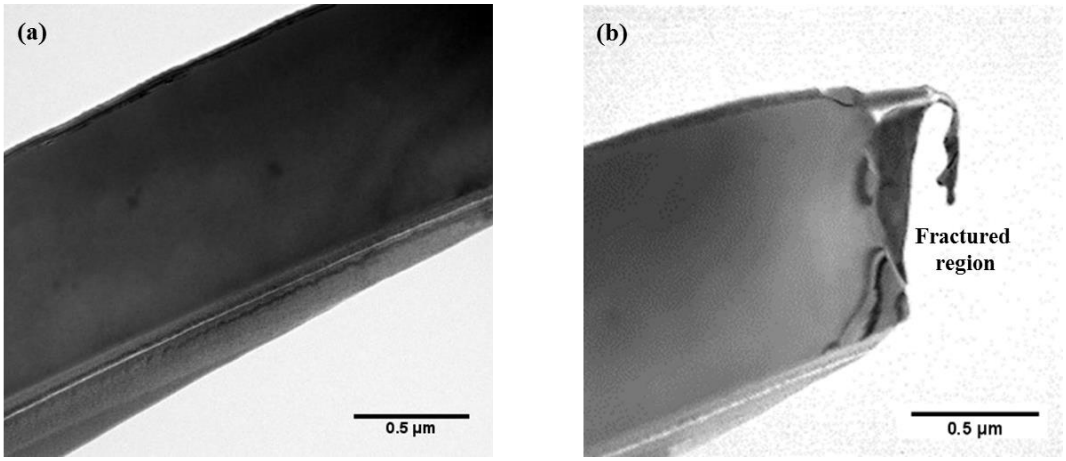

Figure 19. (a, b) Bright field TEM images of deformed Sn whiskers obtained by indentation showing absence of dislocation storage.

On the other hand, the deformation in aged whiskers was found to proceed by a different mechanism. The as-grown aged whiskers showed dislocations arranged in the form of ordered arrays (Fig. 10 (a), (b)). The aged whiskers were exposed to high temperatures for prolonged periods of time prior to the test facilitating dislocation climb and cross-slip. It can be hypothesized that these dislocations try to re-arrange in to low-energy configurations (boundaries) resulting in the ordered array structure. Increased density of the dislocations along with extensive development of cell like structures was prevalent in the deformed aged whiskers (Fig. 10 (c)-(f)). When subjected to load, the dislocations behave very similar to bulk tin and cross slip, climb easily facilitating the formation of sub-grains. It is also possible that several of these boundaries try to link together (Fig. 10 (c)) and result in the extensive sub-grain structure (Fig. 10 (e), (f)). These sub-grains formed are with high density of dislocations at the boundaries and the interior of the grains are essentially dislocation free. The constituent dislocations at the

sub-grain boundary can be clearly seen in Fig. 10 (d). Similar sub-grain structure as observed in aged tin whiskers in the present study was also observed to form in bulk electrodeposited tin coatings due to stress [15, 48]. The aged whiskers and the bulk tin deposits resemble in a way that both contain numerous defects initially unlike the indented whiskers and we believe that the higher dislocation density in aged whiskers might have resulted due to thermal stresses. The sub-grain formation is an indication of dynamic recovery, a phenomenon commonly observed in metals being plastically deformed at temperatures around (0.5-0.7) T_m [48].

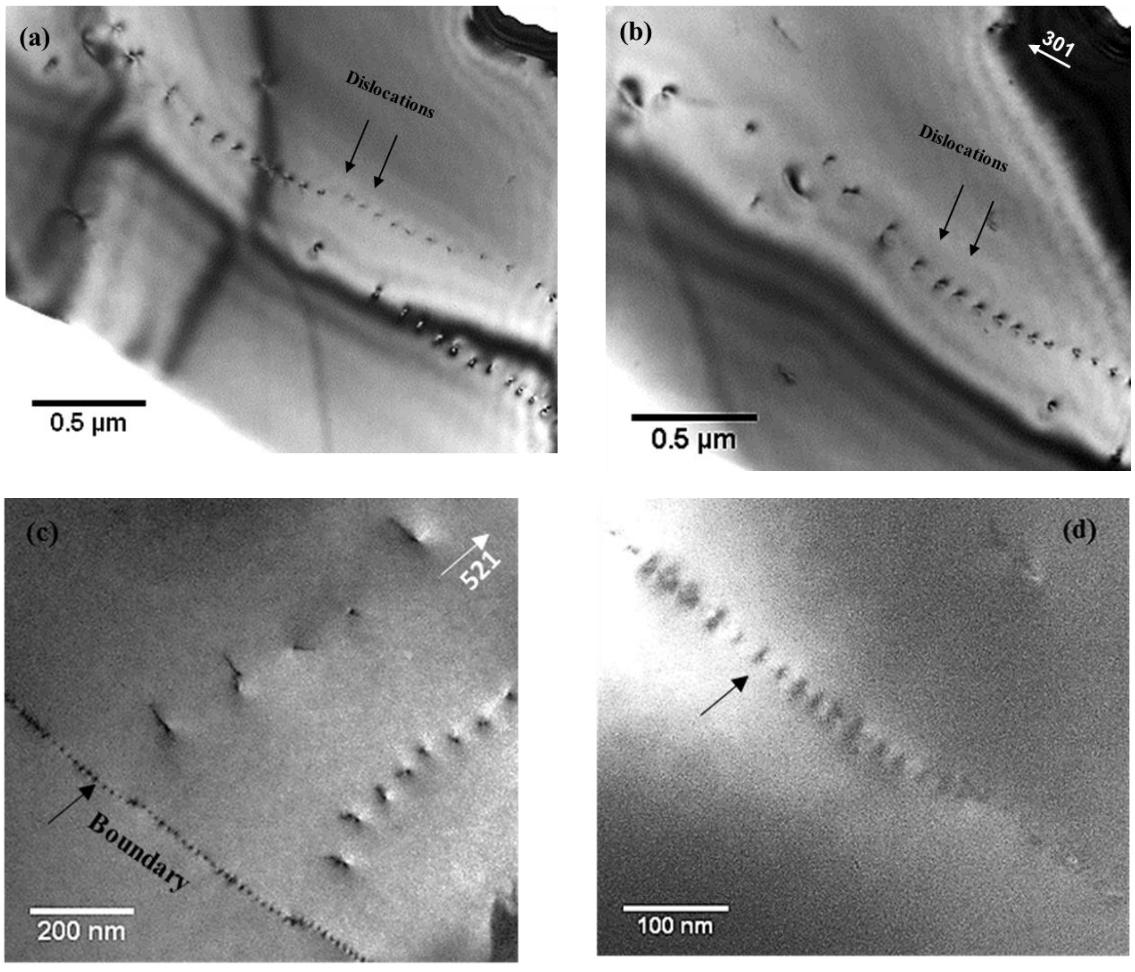

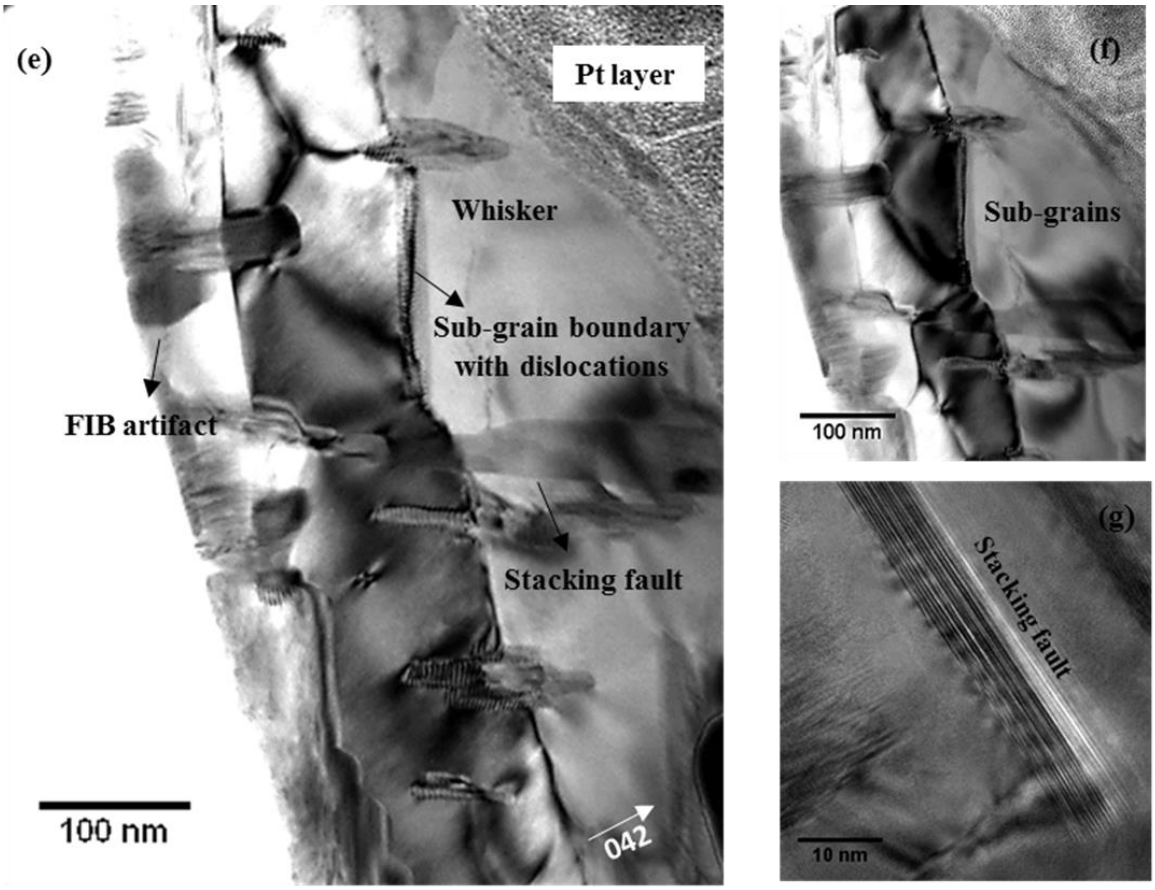

Figure 20. Bright field TEM images of Sn whiskers obtained by high temperature furnace aging: (a, b) As-grown whiskers showing dislocation array structure (c) Deformed whisker showing low energy boundaries trying to link up to form sub-grains (d) Individual dislocations of a sub-grain boundary shown in c (e) Deformed whisker showing sub-grain boundaries with the constituent dislocations and stacking faults emanating from the sub-grain boundaries (f) Clear view of some of the sub-grains shown in (e) (g) Stacking fault observed in a deformed whisker.

Apart from sub-grains, stacking faults with a similar fringe like appearance were also observed in aged whiskers emanating from sub-grain boundaries as shown in Fig. 10 (e) and (g). Dislocations from the sub-grain boundaries might be emitted leaving behind a stacking fault. It was interesting to observe stacking faults in tin whiskers evidencing

partial dislocation activity although tin is a high stacking fault energy material. Several simulation studies have suggested the possibility of stacking faults in tin but there is no experimental evidence till date. Kinoshita et al. suggested that it is energetically favorable for dislocations to dissociate on certain slip systems in tin [49]. To the best of our knowledge, prior to this study, presence of stacking faults in tin has been suggested [49, 50] but not observed and this is one of the first studies to reveal stacking faults in tin.

The contrast in the features observed in the two types of whiskers lead to the important observation that the structure and hence the mechanical behavior of tin whiskers differs significantly with the growth mechanism. The strength variation observed between the indented and aged whiskers in this study could be understood by the fact that the stress required to move pre-existing dislocations as in aged whiskers is lower than that required for dislocation nucleation in indented whiskers.

3.4. Summary

In the present study, tin whiskers were obtained for tensile tests using two accelerated growth methods: indentation and high temperature furnace aging. Both methods introduce compressive stress in the electroplated Sn film and whiskers were found to nucleate and grow to relieve this stress. The source of stress in the indented samples was found to be due to the indenter and the recrystallized grain structure formed due to it was found to aid in the whisker nucleation and growth. Whereas, extensive formation of intermetallic compounds of Cu and Sn were found to be the source of stress in the aged samples. The whiskers obtained by these two methods were utilized for tensile tests. Tensile tests were successfully carried out ensuring maximum reliability by

lifting out whiskers using FIB and placing them on MEMS tensile testing stage inside FIB/SEM. Multiple whiskers tested at each condition produced similar strength values indicating the reliability and repeatability of the testing method. It was observed that the tin whiskers possess high strengths due to their low defect densities compared to bulk materials. The strength of the whiskers was found to be dependent on the gage length at which they were tested and also the processing method. Since there is a high probability to encounter defects as the length is increased, the strength of the whiskers was found to decrease with an increase in their length. The effect of oxygen on the observed processing effect was investigated and the analysis led to an interesting fact that the oxide growth is not significant even at the high temperature exposed in this study and hence there is no effect of oxygen on the strength variation observed. TEM analysis was performed to understand the processing effect as well as the deformation mechanisms in tin whiskers. It is evident from the TEM results that the deformation in the indented whiskers is controlled by dislocation nucleation explaining the high strengths of those. On the other hand, deformation in the aged whiskers is mainly controlled by the arrangement of dislocations in to low-energy configurations and formation of sub-grains leading resembling the behavior of bulk tin. This difference in the features observed in the two types of whiskers clearly explain the strength variation observed.

3.5 References

[1] iNEMI Tin Whisker User Group, Recommendations on lead-free finishes for components used in high-reliability products, version 4, http://www.inemi.org/cms/ [accessed 04/15/2016].

[2] NASA, Multiple examples of whisker-induced failures are documented on the NASA

website, http://nepp.nasa.gov/whisker/ [accessed 04/15/2016].

[3] R.M. Fisher, L.S. Darken, and K.G. Carroll, Acta Metall. 1954; 2: 368.

[4] B.D. Dunn, Circuit World. 1976; 2: 32.

[5] C. Xu, IEEE Trans. Electron. Packag. 2005; 28: 31.

[6] Choi WJ, Lee TY, Tu KN, Tamura N, Celestre RS, Mcdowell AA, et al, proceedings of the 52nd electronics components and technology conference; May 28–31, 2002. p. 628–33.

[7] M. Sobiech, C. Krüger, U. Welzel, J.Y. Wang, E.J. Mittemeijer, W. Hügel, J. Mater. Res. 2010; 25: 2166.

[8] C. Xu, Y. Zhang, C.L. Fan, J.A. Abys, IEEE Trans. Electron. Packag. Manuf. 2005; 28: 31.

[9] M.J. Bozack, E.R. Crandall, C.L. Rodekohr, R.N. Dean, G.T. Flowers, J.C. Suhling, IEEE Trans. Electron. Packag. Manuf. 2010; 33: 198.

[10] K. Murakami, M. Okano, M. Hino, M. Takamizawa, K. Nakai, Mater. Trans. 2010; 51: 143.

[11] W.J. Boettinger, C.E. Johnson, L.A. Bendersky, K.W. Moon, M.E. Williams, G.R. Stafford, Acta Mater. 2005; 53: 5033.

[12] K.N. Tu, Acta Metall. 1973; 21: 347.

[13] X. Deng, G. Piotrowski, J.J. Williams, N. Chawla, J. Electron. Mater. 2003; 32: 1403.

[14] B.Z. Lee, D.N. Lee, Acta Mater. 1998; 46: 3701.

[15] E. Chason, N. Jadhav, W.L. Chan, L. Reinbold, K.S. Kumar, Appl. Phys. Lett. 2008; 92: 171901.

[16] Craig Hillman, Gregg Kittlesen, and Randy Schueller, A new (better) approach to tin whisker mitigation, Dfr solutions, http://www.dfrsolutions.com/uploads/white-papers/WP_SnWhisker.pdf, [accessed 04/15/2016].

[17] Tadahiro Shibutani, Qiang Yu, Masaki Shiratori, Michael G. Pecht, Microelectron. Reliab. 2008; 48: 1033.

[18] S.S. Singh, R. Sarkar, H.-X. Xie, C. Mayer, J. Rajagopalan and N. Chawla, J. Electron. Mater. 2014; 43: 978.

[19] B.E. Powell and M.J. Skove, J. Appl. Phys. 1965; 36: 1495.

[20] B.D. Dunn, Eur. Space Agency (ESA) J. 1987; 11: 1.

[21] NASA, The continuing dangers of tin whiskers and attempts to control them with conformal coating, http://nepp.nasa.gov/docuploads/95565195-0E5A-40D8-98D88425FF668F68/JayBrusseRevision2.pdf [accessed 04/15/2016].

[22] J. Smetana, iNEMI tin whisker user group. iNEMI recommendations on lead free finishes for components used in high reliability products, Proceedings of IPC Printed Circuits Exposition, Apex, and the Designers Summit, Anaheim, CA, February 5–10, 2006.

[23] L.A. Pinol, J. Melngailis, H.K. Charles, D.M. Lee, R. Deacon, G. Coles, G. Clatterbaugh, IEEE Trans. Compon. Packag. Manuf. Technol. 2011; 1: 2028.

[24] J. Cheng, F.Q. Yang, P.T. Vianco, B. Zhang, J.C.M. Li, J. Electron. Mater. 2011; 40: 2069.

[25] M.H. Lu, K.C. Hsieh, J. Electron. Mater. 2007; 36: 1448.

[26] S.C. Britton, Trans. Inst. Metal Finishing. 1974; 52: 95.

[27] W.J. Choi, T.Y. Lee, K.N. Tu, N. Tamura, R.S. Celestre, A.A. MacDowell, Y.Y. Bong, L. Nguyen, Acta. Mater. 2003 ; 51: 6253.

[28] K.N. Tu, Phys. Rev. B. 1994; 49: 2030.

[29] B.-Z. Lee, D.N. Lee, Acta Mater. 1998; 46: 3701.

[30] K.S. Kumar, L. Reinbold, A.F. Bower, and E. Chason, J. Mater. Res. 2008; 23: 2916.

[31] J.W. Osenbach, J.M. De Lucca, B.D. Potterger, A. Amin, R.L. Shook, F.A. Baiocchi, IEEE Trans. EPM. 2007; 30: 23.

[32] E. Chason, N. Jadhav, W.L. Chan, L. Reinbold, K.S. Kumar, Appl. Phys. Lett. 2008; 92: 171901.

[33] W.J. Boettinger, C.E. Johnson, L.A. Bendersky, K.-W. Moon, M.E. Williams, G.R. Stafford, Acta Mater. 2005; 53: 5033.

[34] Kyle Doudrick, Jeff Chinn, Jason Williams, Nikhilesh Chawla, Konrad Rykaczewski, Microelectron. Reliab. 2015; 55: 832.

[35] J. Rajagopalan, C. Rentenberger, H.P. Karnthaler, G. Dehm, and M.T.A. Saif, Acta Mater. 2010; 58: 4772.

[36] J. Rajagopalan and M.T.A. Saif, J. Mater. Res. 2011; 26: 2826.

[37] J.H. Han and M.T.A. Saif, Rev. Sci. Instrum. 2006; 77: 045102.

[38] J.H. Han, J. Rajagopalan, and M.T.A. Saif, Proc. 2007; SPIE 6464: 64640C.

[39] M.A. Haque and M.T.A. Saif, Exp. Mech. 2002; 42: 123.

[40] J.J. Williams, N.C. Chapman, and N. Chawla, J. Electron. Mater. 2013; 42: 224.

[41] Shih-Kang Lin, Yuhi Yorikado, Junxiang Jiang, Keun-Soo Kim, Katsuaki Suganuma, Sinn-Wen Chen, Masanobu Tsujimoto, and Isamu Yanada, J. Electron. Mater. 2007; 36: 1732.

[42] Kiyotaka Tsuji, Role of grain-boundary free energy & surface free energy for tin whisker growth, http://unicon.co.jp/business/pdf/data_rollofgrain.pdf [accessed 04/15/2016].

[43] K. N. Tu, Chih Chen, Albert T. Wu, J Mater Sci: Mater Electron. 2007; 18: 269.

[44] M.W. Barsoum, E.N. Hoffman, R.D. Doherty, S. Gupta, and A. Zavaliangos, Phys. Rev. Lett. 2004; 93: 206104.

[45] B.-Z. Lee and D.N. Lee, Acta Mater. 1998; 46: 3701.

[46] Ray, U., I. Artaki, and P.T. Vianco, IEEE Transactions on components, packaging, and manufacturing technology-part a. Vol. IX. NO I, March 1995.

[47] Copper-Tin Intermetallic Compounds, copper development association Inc., http://www.copper.org/applications/industrial/DesignGuide/performance/coppertin03.html [accessed 04/15/2016].

[48] K.S. Kumar, L. Reinbold, A.F. Bower, and E. Chason, J. Mater. Res. 2008; 23: 171901.

[49] Kinoshita Y, Matsushima H, Ohno N. Model Simul Mater Sci Eng. 2012; 20:035003.

[50] Kinoshita Y, Ohno N., Key Eng. Mater. 2015; 626: 20.

CHAPTER 4

3D MICROSTRUCTURAL CHARACTERIZATION OF PITS USING X-RAY TOMOGRAPHY AND THEIR INFLUENCE ON THE MECHANICAL BEHAVIOR IN ALUMINUM 7075 ALLOYS

4.1 Introduction

7075 aluminum alloys are widely used in various industries due to their high strength-to-weight ratio [1-4]. The corrosion resistance of aluminum is due to its ability to form a natural oxide film (passive) on its surface [5-9]. It has been reported that the oxide film can readily undergo corrosion reactions in chloride environments [10, 11] and the film breaks down at certain points resulting in the formation of pits on the aluminum surface. This type of corrosion is known as pitting corrosion [12-14]. Pitting proceeds by destruction of the protective oxide by adsorption of Cl^- followed by formation of chlorocomplexes that subsequently pass into the solution [15, 16]. Pitting corrosion in the presence of aggressive chloride ions (Cl^-) is known to be the most frequently encountered cause of failure of these high-strength aluminum (Al) alloys [17]. Pitting is the precursor to stress corrosion cracking (SCC) as it provides the required combination of an aggressive local solution chemistry and a stress concentrating feature [18]. Pitting is also identified as potential origin for fatigue crack nucleation [19-21] which can grow at an accelerated rate in corrosive environment affecting the structural integrity of the components [22]. Therefore, it is very important to investigate pitting and understand their effect on the mechanical performance of the alloy. This work focuses on the characterization of pitting in 7075 Al alloys corroded in 3.5 wt.% NaCl solution.

Several studies have been performed in aluminum alloys to visualize pits and understand their effect on the mechanical performance of the alloy, especially fatigue strength. But in most of the studies, optical microscope or SEM were used to observe the pits [23-26]. Two-dimensional (2D) approach is often inadequate and would result in limited information regarding the pits. To get a thorough understanding of the nature of the pits, its dimensions and correlate the microstructure with the mechanical properties, it is necessary for three-dimensional (3D) studies. X-ray tomography is an excellent technique for this purpose. It is non-destructive and allows for superior resolution and image quality with minimal sample preparation. Due to its nondestructive nature, microstructure evolution with time also can be observed. In addition to visualization, such microstructural data sets can be incorporated into finite element models to elucidate the effect of microstructure on bulk deformation behavior [27-33] and for the development of other modeling approaches. Recently, this technique is being extensively used to study the corrosion behavior in three dimensions and its effect on the mechanical behavior of Al alloys [34-39]. X-ray tomography will not only enable us to visualize the pits in 3D in different orientations, but from the 3D microstructure, we can also quantify the dimensions accurately. The data obtained from the 3D microstructure can be correlated with the mechanical behavior of the alloy.

In this work, 7075 Al alloy specimens were corroded in 3.5 wt.% NaCl solution. Multiple samples were corroded and removed after different times (0, 2, 16, 30 and 45 days). Tensile tests were performed on the different samples to understand the effect of corrosion on the strength. X-ray tomographic analysis was performed to visualize pits in 3D and to quantify their dimensions accurately. Knowledge of the 3D microstructure and

structure-property correlation will enable us to better understand corrosion in Al and design alloys against stress corrosion cracking.

4.2 Experimental procedure

The material used in this study was a commercially available 7075-T651 aluminum alloy (5.63 Zn, 2.45 Mg, 1.55 Cu, 0.045 Si, 0.18 Fe, 0.008 Mn, 0.19 Cr, 0.004 Ni, 0.049 Ti, and rest Al) rolled to a 3 inch thickness. Round test specimens with dog bone specimen geometry suitable for tensile testing (diameter = 1mm) were machined by electro-discharge machining such that the longest dimension (length = 22 mm) was along the short-transverse (S-T) orientation. The gage length of this specimen was 8 mm. Since the specimens need to be suitable for X-ray tomography also, which essentially requires a small region of interest, the specimens were covered with a corrosion resistant paint leaving a small region (2 mm) in the center and only this region was exposed to the corrosive fluid. Before the exposure, the region of interest was polished till 1 μm diamond finish and sonicated in acetone to remove any debris. The polished specimens were then exposed to 3.5 wt.% NaCl solution and removed after different times (0, 2, 16, 30 and 45 days). Two specimens were prepared per condition out of which one was used for tensile testing alone and the other was used for X-ray tomography followed by a tensile test.

An *in situ* mechanical testing stage was designed by [40, 41] for synchrotron tomography beam lines. This loading jig is suitable for the present study and has been used for tensile testing with appropriate modifications made to the grips to accommodate the current

sample (Figure 21). Also, since the current tensile tests are not performed *in situ*, the X-ray transparent sleeve was not used. The stepper motor used had a captive linear actuator capable of 8 μm per step and a total stroke of 12 mm. The load cell had a capacity of 500 N. It was ensured that the load train was precisely aligned prior to the test. The sample was placed in between the grips that are attached to the actuator on one side and to the load cell on the other. The stepper motor with the linear actuator applies displacement on the sample and the corresponding load was measured by the load cell. The stress and strain on the specimens during the tensile tests were thus obtained. In this way, tensile tests were performed on the samples corroded for different times and the deterioration of strength with increasing corrosion was studied. Characterization of the fractured samples was done by a dual-beam FIB/SEM (Carl Zeiss Auriga) coupled with an energy dispersed X-ray spectroscopy system (EDX). The structure of the failed region was visualized by imaging using the SEM and compositional analysis was performed using EDX.

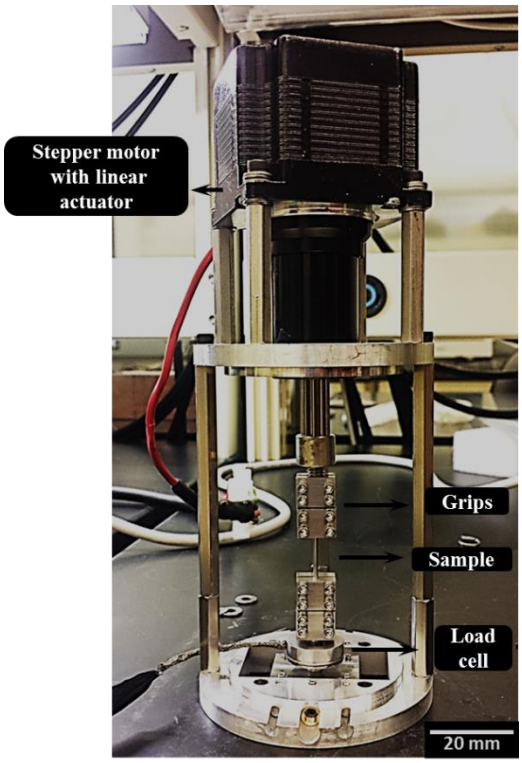

Figure 21. Mechanical loading jig used for tensile testing. The various components of the jig along with the sample are indicated.

X-ray microtomography was conducted on a custom-built system developed at Arizona State University. Details of the development and instrumentation for the system have been provided elsewhere [42]. The operating conditions were selected in such a way that a good contrast is obtained between the Al matrix and the inclusions. The sample was imaged 801 times corresponding to each unique angular position having a 1/4° multiple between 0° and 200°. These radiographs were acquired by X-ray emission at 60 KV with 130 mA of target current, with an X-ray magnification of 6× and a lens magnification of 3.8× resulting in a field of view of about 1.3 mm. Each pixel corresponds to a $(1.2\ \mu m)^2$ area in the sample. Each projection was calibrated for any

defects in the optical system and variability in the CCD elements' sensitivity using a master dark and a master flat frame as explained by [42] resulting in images as shown in Figure 22. To obtain the best possible resolution, three scans (top, middle and bottom) were conducted in the region of interest (2 mm) for each sample. Along with the region of interest, a portion of the paint was also scanned in the top and bottom scans. This was done to ensure that there is negligible crevice corrosion at the interface of the paint and the sample which might affect the mechanical behavior. Reconstruction of the sample's 3D structure was carried out with the help of fast-Fourier-transform back-projection algorithms using the cone-beam Feldkamp–Davis–Kress (FDK) method [42] implemented using MATLAB (MathWorks) script.

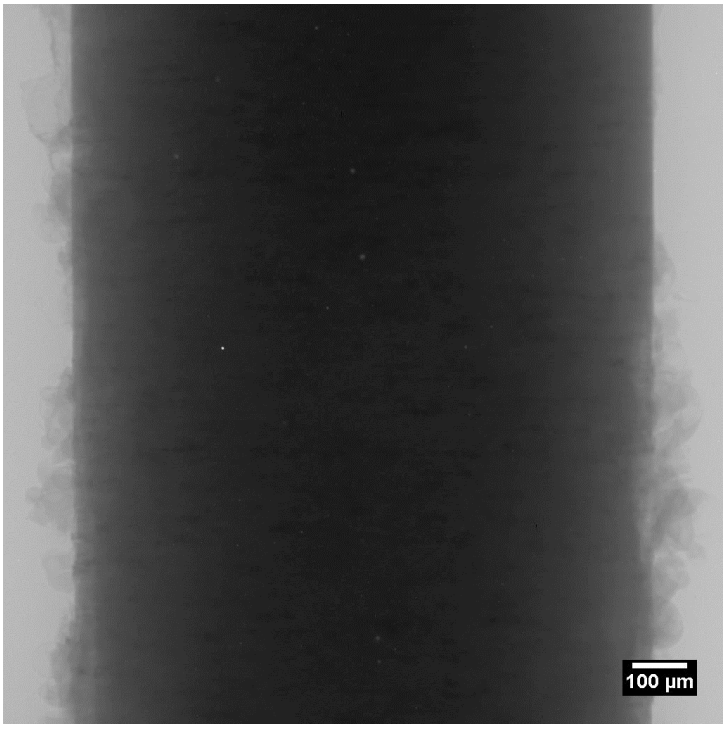

Figure 22. Representative image of a projection obtained from the X-ray tomography after calibration. Outer corrosion layer can also be seen.

Reconstruction produces a stack of two-dimensional (2D) slices and can be viewed from different orientations as shown in Figure 23 (a). Since three separate scans were performed per each sample, the different data sets were stitched together and prepared for segmentation. The background noise in the images was reduced by using image filters. All filtering and segmentation was performed using the Avizo Fire (VSG, Burlington, MA) software package. A non-local means filter was implemented to reduce the noise and preserve the edges making the features sharp. The selection of the appropriate filter was determined by trial-and-error to achieve images that are with least noise and best for segmentation. The improvement in the quality of the images after applying the filter can be seen in Figure 23 (b).

The next step was to visualize the pits in 3D. This is achieved by segmentation of the pits from the rest of the data and 3D rendering using Avizo software. Individual pits were identified and selected in successive slices manually and using semi-automated tools in the software. In this way, all the pits were segmented and visualized in 3D. The Avizo software can also provide quantitative measurements of the segmented data. The volume of each individual pit is extracted from the software whereas the depth was measured manually using image analysis software (ImageJ, Bethesda, MD). Statistical analyses of the pit volumes and depths with respect to corrosion time were performed. The SEM image obtained post fracture was matched with the X-ray tomographic slice which enabled a better understanding of the structure-property correlations in corroded Al 7075 alloys.

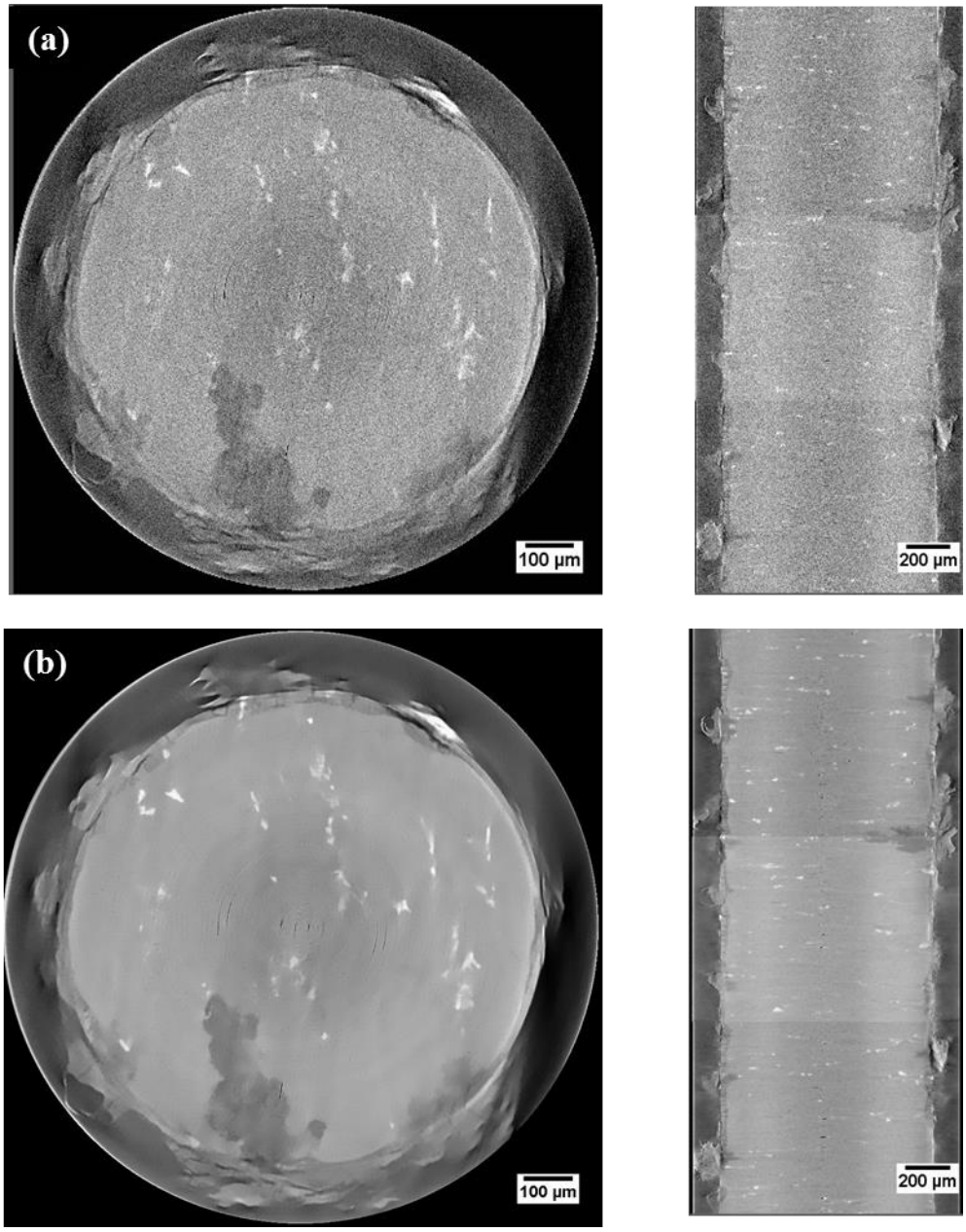

Figure 23. 2D X-ray tomography slices in different orientations (a) Slices after reconstruction prior to filtering (b) Slices after reconstruction and application of non-local means filter reducing showing improvement in quality.

To study the evolution of individual pits due to corrosion, another specimen (Al 7075 in LT orientation) has been prepared and corroded similarly. X-ray tomography

scans were performed once after every 2 days of corrosion and the pit growth is monitored till 20 days. The region of interest was reduced to 1 mm in the center enabling just one scan to be enough to cover the required region.

4.3 Results and Discussion

4.3.1 Effect of corrosion on the tensile strength

Figure 24 shows representative tensile stress-strain curves at different times of corrosion. The determinantal effect of corrosion on the strength of aluminum can be clearly observed. The variation of average tensile strength obtained from the two tests with corrosion is represented in Table 1. The sample after 2 days of corrosion remained mostly unaffected due to corrosion and showed very slight reduction or a similar strength as the un-corroded specimen. It can be seen that a reduction of about 70-100 MPa in strength occurred after 45 days of corrosion. Understanding of the microstructure of the corroded specimens would provide a better idea regarding the causes of the reduction in strength.

Table 1. Variation of tensile strength with corrosion

Corrosion	0 days	2 days	16 days	30 days	45 days
Average tensile strength (MPa)	468.5	474	439	393	365

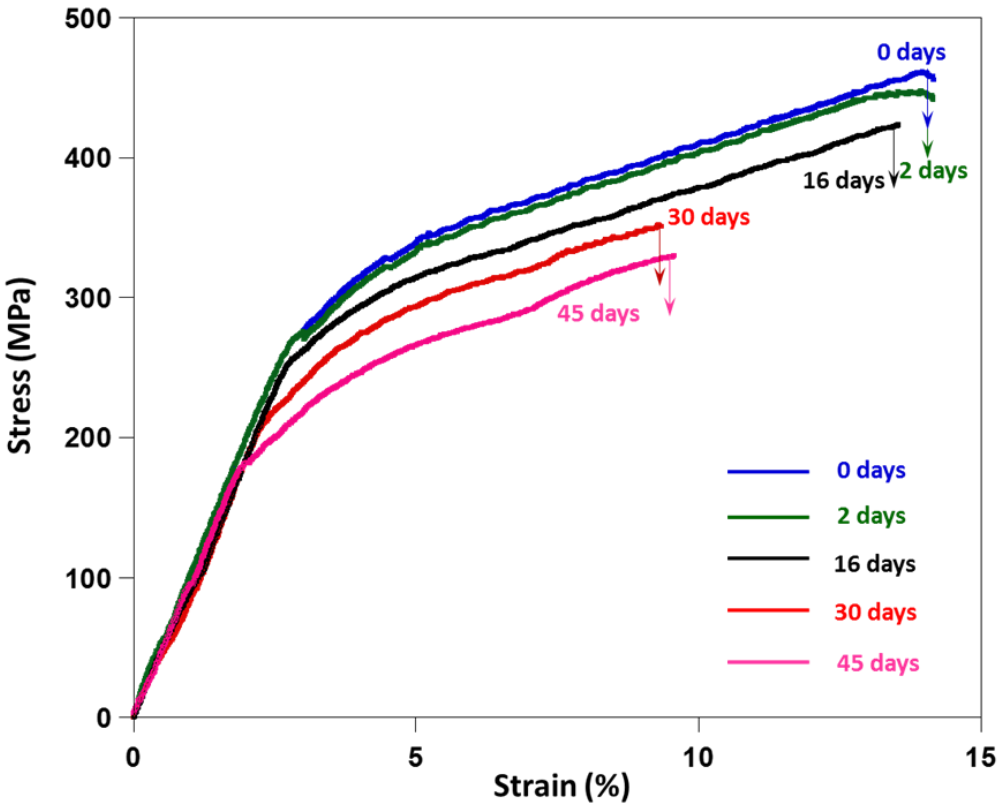

Figure 24. Tensile stress-strain curves showing a decrease in strength with corrosion.

Figure 25 and Figure 26 show the SEM images taken post fracture. A good contrast between the corroded, un-corroded regions and inclusions could be obtained in the back scattered electron images. It is known that failure process in ductile materials is associated with local failure of second phase particles, e.g., inclusions, intermetallic particles, and precipitates [43, 44]. Inclusion fracture has been observed in the un-corroded specimen in the current experiment and can be visualized in Figure 25. where Figure 25 (b) and 25 (c) represent the top and bottom parts of the fractured specimen illustrating an inclusion that has fractured.

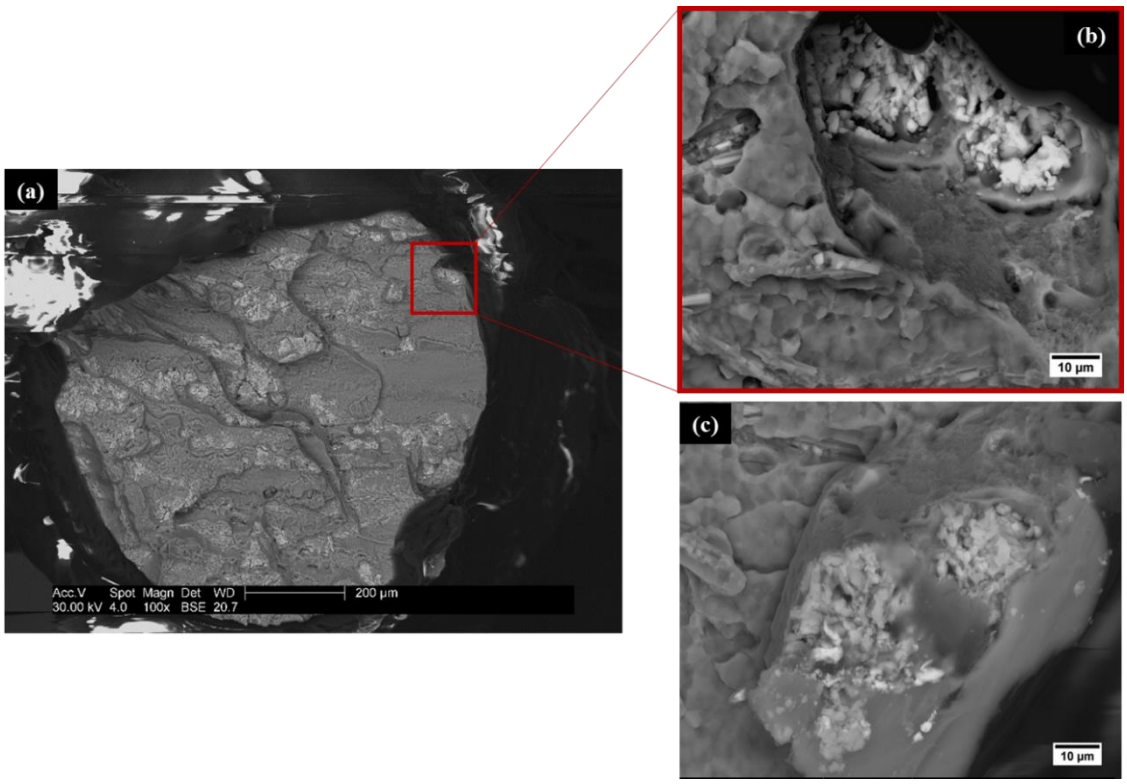

Figure 25. (a) Un-corroded specimen post-fracture (b and c) Top and bottom parts of the fracture surface showing inclusion fracture.

In the corroded specimens, damaged regions due to corrosion (pits and corrosion products) were extensively observed in the fracture surfaces (Figure 26). Also, with increase in corrosion, it was observed that the damaged region penetrated deeper in to the sample (Figure 26 (b)). The pits are like discontinuities in the sample and can be the sites for stress concentration. Pits penetrating deeper in to the sample with increasing corrosion would result in more stress concentration, hence leading to the reduction in strength.

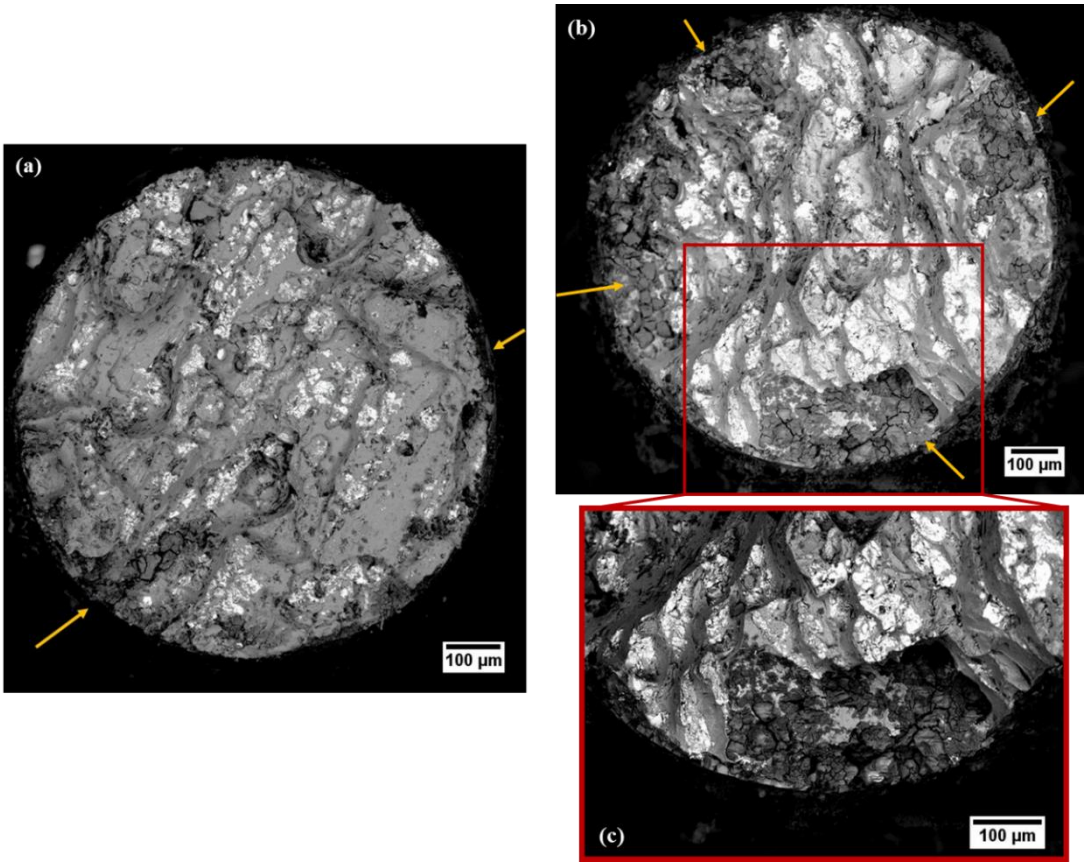

.

Figure 26. Corroded specimens post fracture (a) Corroded for 16 days (b) Corroded for 30 days (c) High magnification image showing a pit from (b). The arrows represent the pits and corrosion products. The corroded region penetrating deeper in to the specimen with increase in corrosion can be observed.

From the SEM observations, it was observed that pits were partially of fully filled with corrosion products. Chemical composition analysis by EDX revealed that this salt is primarily composed of oxygen and aluminum with low concentrations of zinc, sodium and chlorine (Figure 27). The aluminum dissolution reaction in chloride solutions is found to proceed by the formation of aluminum oxy hydroxyl chlorides which further react to form aluminum hydroxide ($Al(OH)_3$) and hydrated aluminum oxide [12]. The

ratio between Al and O observed in this study was about 0.5 - 0.6 indicating that the salt in the pits is likely $Al(OH)_3$ along with sodium and chloride ions.

The pits are discontinuities in the sample and they are no longer aluminum. The salts comprising the pits showed severe compositional modification suggesting the deleterious effect these might have on the strength of the alloy. The strength of the alloy depends on the sizes of the pits formed and hence the quantification of pit dimensions, their correlation with the tensile strength is important. While the SEM images shown above provide basic idea regarding the microstructure, the information is only limited to two-dimensions (2D). These are often inadequate and to achieve a comprehensive understanding of the pit structure and quantify their dimensions accurately, it is necessary to visualize these in three-dimensions (3D). X-ray tomography is best suited for this purpose and is explained in the next section.

4.3.2 Three-dimensional visualization of pits and quantification of their dimensions using X-ray tomography

X-ray tomography used in the present study works mainly by the principle of absorption contrast. Absorption contrast exists when the attenuation of incident X-rays is proportional to mass density; and therefore, Fe-bearing inclusions (high mass density) appear bright and pits (low mass density) appear dark in the reconstructed images (Figure 28). Going back and forth in these slices, the entire pit could be seen clearly in different orientations resulting in a better idea about the pit compared to the 2D SEM imaging. Representative 2D slices from X-ray tomography at various corrosion times can be seen in Figure 28.

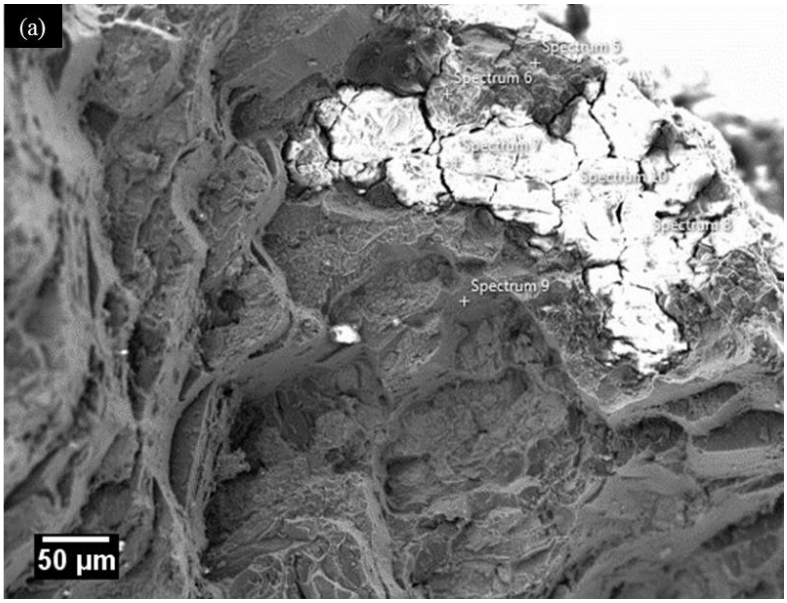

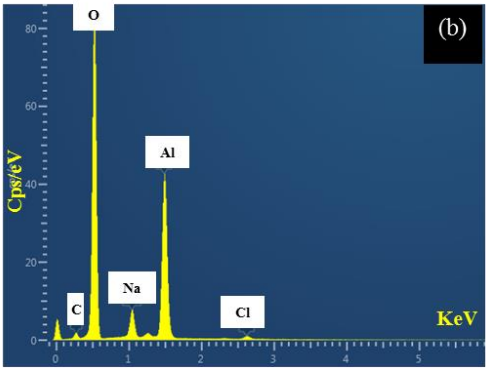

(c)	Composition (wt. %)
O	58.9 ± 0.6
Al	31.4 ± 0.3
Na	4.8 ± 0.2
Cl	1.5 ± 0.6
C	3.6 ± 0.1

Figure 27. (a) A Pit filled with salt observed in the fracture surface (b and c) EDX spot scan results showing high oxidation of the salt.

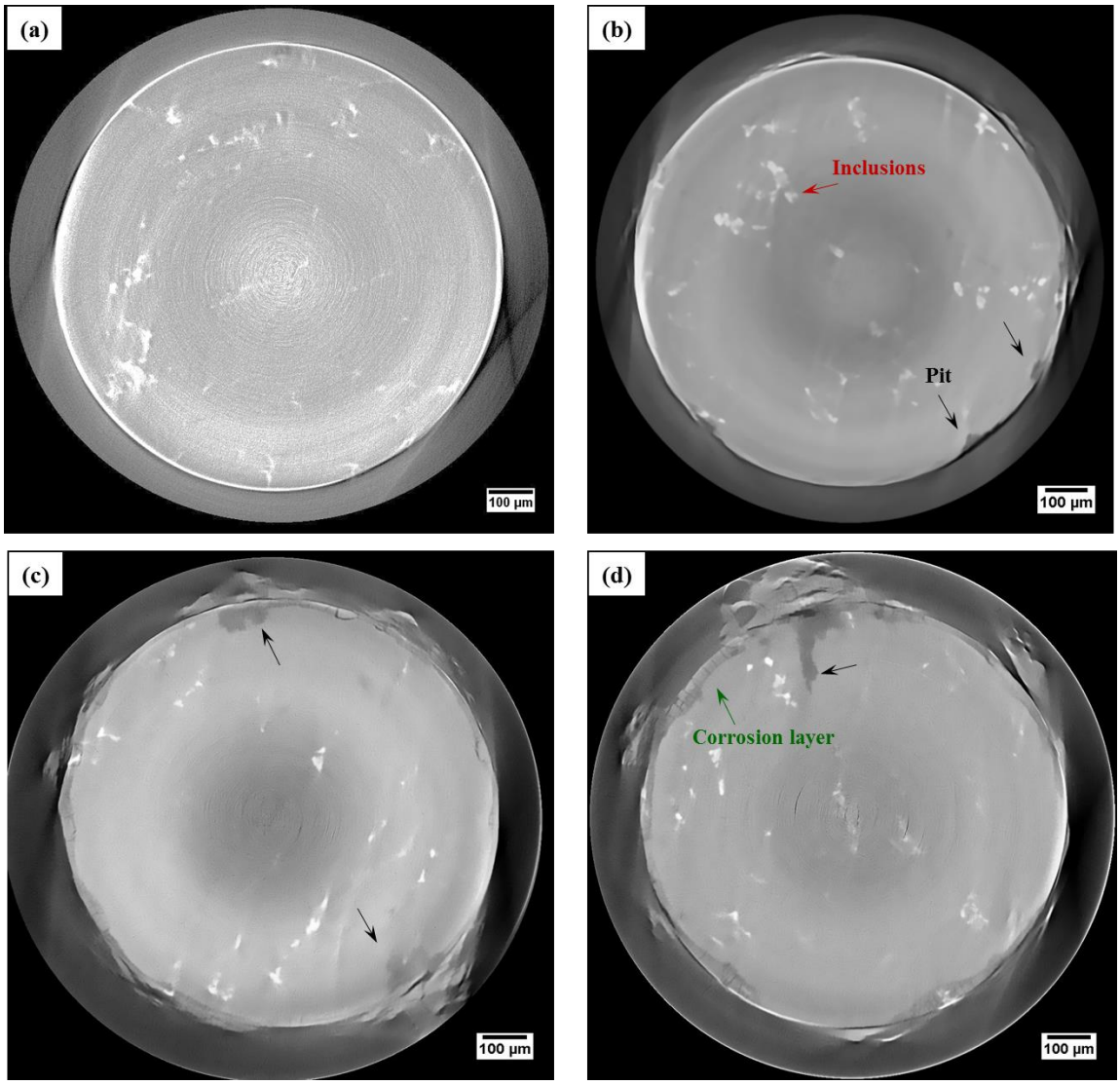

Figure 28. Representative 2D slices obtained from X-ray tomography showing pits, corrosion product and inclusions after (a) 2 days (b) 16 days (c) 30 days (d) 45 days of corrosion.

Since the mechanical strength of the alloy mainly depends on the pit penetration in to the sample, the depth of each individual pit was measured and analyzed. Compared to conventional SEM imaging which provides the details of the pits from a single slice, the X-ray tomographic scans, enable us to observe the entire pit and locate the region of

maximum penetration. Knowing the maximum depth a pit has penetrated would be useful since it would be the region where maximum stress concentration would likely occur. Each individual pit was located, and observing all the slices in which the pit spans, its maximum depth was measured. The distance from the deepest point of penetration to the surface was considered as the depth of the pit. In this way, the depths of all the pits in each specimen were measured. The frequency distribution of pit depths at various times of corrosion can be observed in Figure 29. The details of the deepest pit observed in the entire sample and the average depth of all the pits at different times of corrosion are summarized in Table 2. The pits observed after 16 days of corrosion had depths below 40 µm with majority of them lying between 20 and 40 µm. After 30 days of corrosion, the pit depths increased considerably with most of the pits having depths in between 60 and 100 µm.

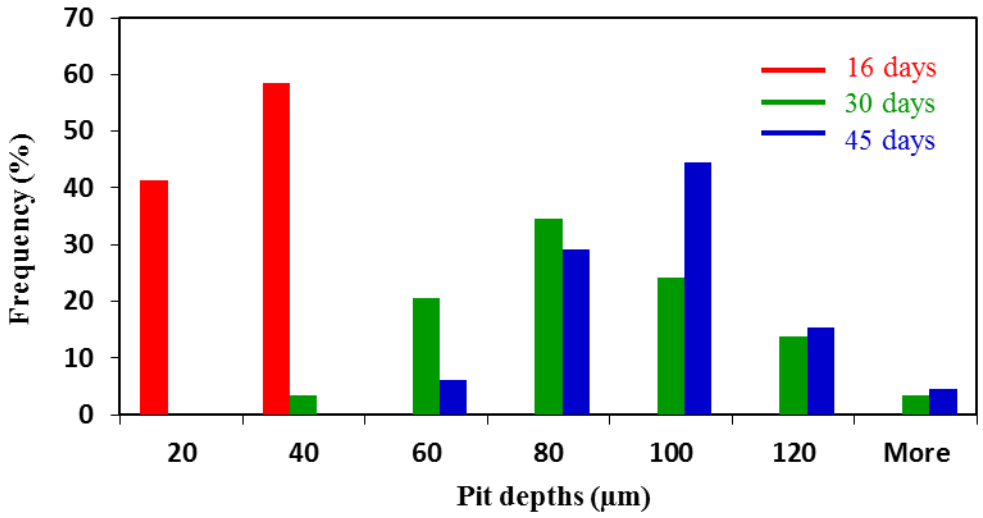

Figure 29. Frequency distribution of pit depths at various times of corrosion.

To visualize the pits in 3D, segmentation of the pits from the rest of the data was performed using the Avizo software. Individual pits were identified and the region inside the pit was selected manually slice by slice using brush and magic wand tools in the software. Figure 30 shows the series of steps used for segmentation along with an example of 3D rendering obtained with all the pits in the specimen segmented. Each individual pit can be visualized in 3D and the details of the pit such as its shape, dimensions can be obtained. Figure 31 shows the 3D renderings of the specimens corroded for various times showing pits on the surface. The size of the pits increasing with corrosion can be clearly observed. It was also observed that most of the pits were adjacent to the Fe-rich inclusions which are segmented in red. It is well known that the corrosion behavior of aluminum alloys is significantly affected by the presence of Fe-rich inclusions and such inclusions are the sites where corrosion pits form [45]. It has been observed in aerated NaCl solution that the Al dissolved preferentially near Fe-rich inclusions, while the inclusions themselves remained inert [3,5]. Such intermetallics are known to influence corrosion of aluminum alloys by functioning as sites for cathodic reaction and this has been observed in the current work. Most of the pits were found to be adjacent to the bright Fe-rich inclusions emphasizing the effect of inclusions on pitting in Al alloys. Also, no definite shape was observed of the pits and they were found to be irregular.

The specimen after 2 days of corrosion showed pits that are very small and difficult to resolve. Also, the number of pits observed were very few and this specimen did not show a considerable reduction in the strength due to which segmentation was not performed on it.

Segmenting the pits and 3D rendering enabled the visualization of pits in 3D which could provide important information regarding its dimensions and shape.

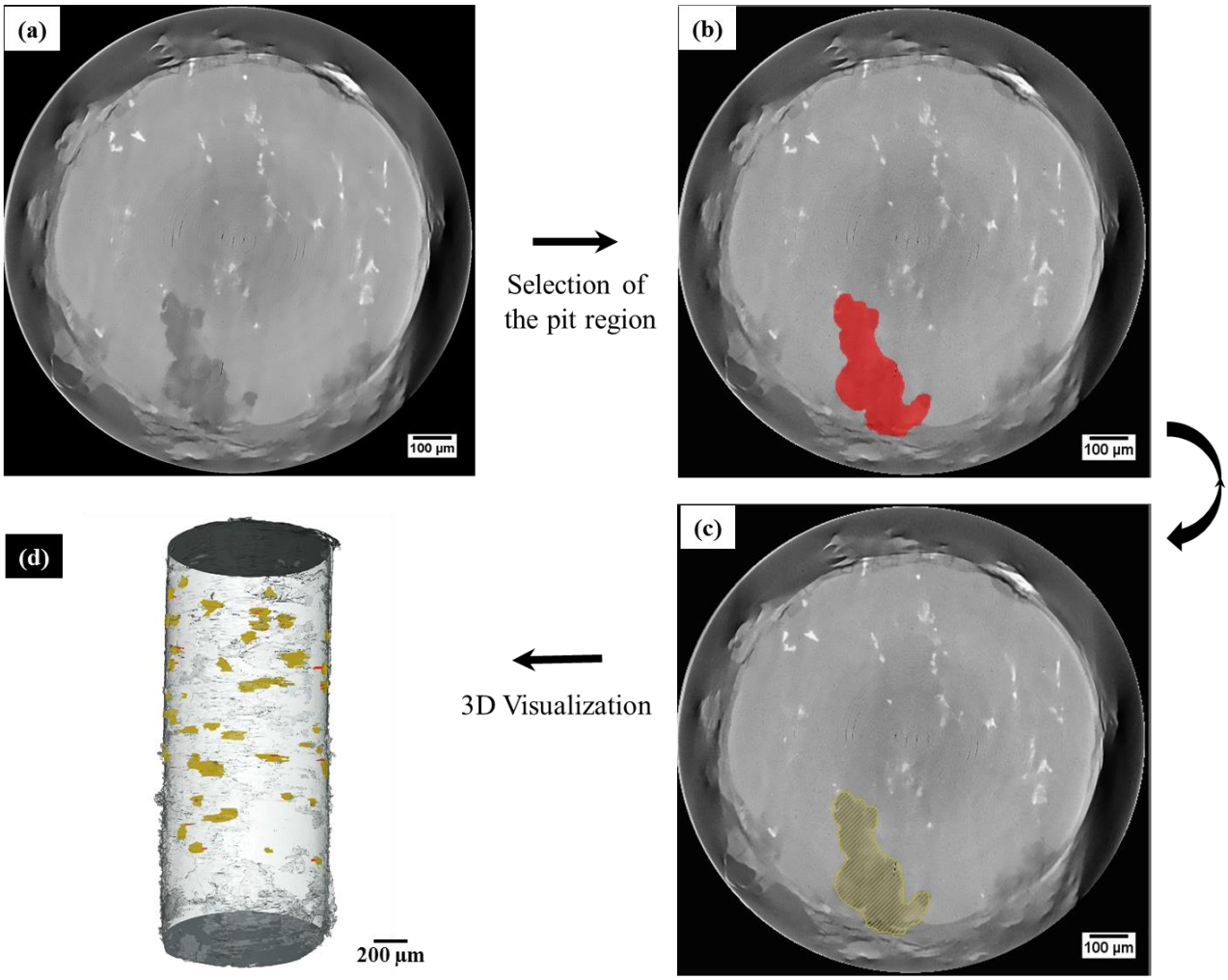

Figure 30. Series of steps used for segmentation of the pits (a-c) Selection of pits using magic wand and brush tools in the Avizo software (d) 3D rendering showing the specimen with all the pits segmented.

A corrosion damage layer with microcracks can also be observed along with the pits in the scans obtained which is characterized in a separate study (chapter 5).

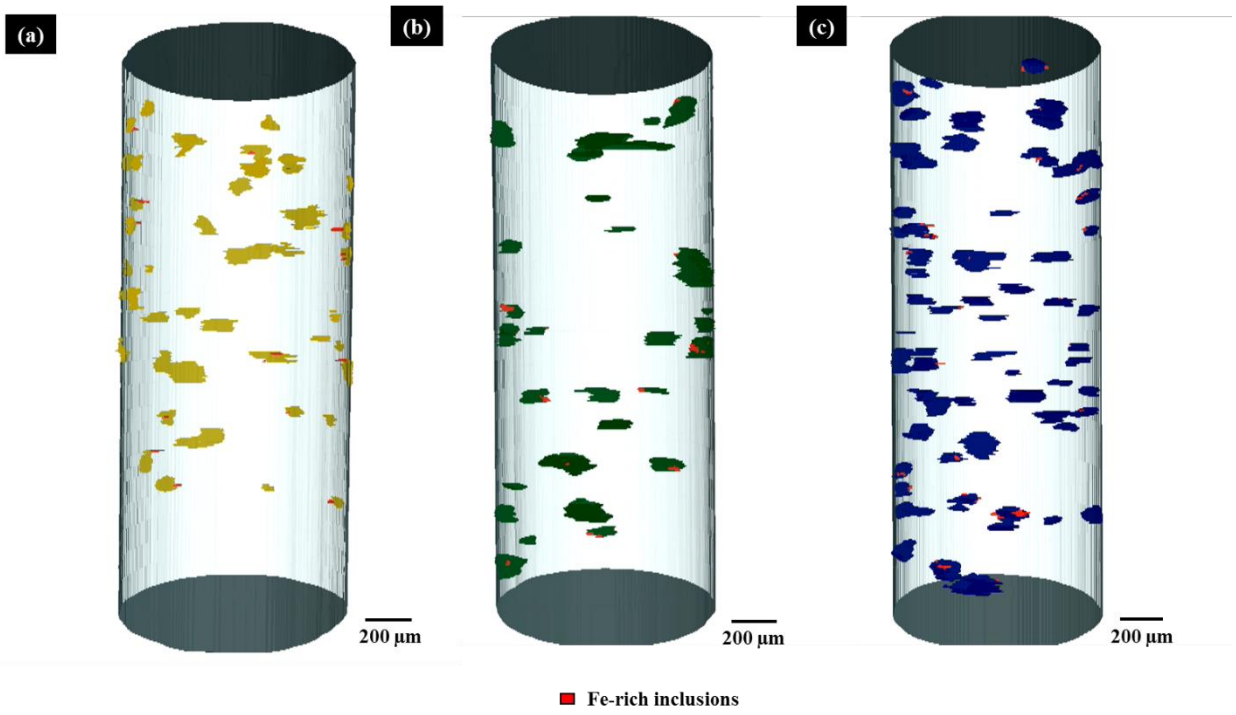

Figure 31. 3D renderings of the specimens with the pits segmented. Fe-rich inclusions adjacent to the pits are also segmented and are shown in red.

Apart from the 3D visualization achieved by segmentation, we can obtain other valuable information such as the volume of the pits from the Avizo software. It computes the volume of all the pixels enclosed in a pit and outputs the volume of the entire pit. In this way, the volume of all the pits found in specimens was computed. This would enable us to compute the total volume fraction of the specimen that is no longer Al and occupied by pits. The frequency distribution of pit volumes at various times of corrosion can be seen in Figure 32. A very high frequency of volume (90%) below $20x10^4$ μm^3 was observed for the pits in specimen corroded for 16 days. After 30 and 45 days of corrosion, large number of pits having bigger sizes were observed. The volume increase

can be attributed to the growth of the pits with time as well as coalescence of smaller pits resulting in a bigger volume. From the total volume occupied by all the pits in the specimen, volume fraction is computed and increase in volume fraction of pits can be observed with increase in corrosion. The details regarding maximum volume of the pit in the sample and the volume fraction occupied by pits with varying corrosion times are given in Table 2.

The depths and volumes of the pits were in the lower end of the distributions after 16 days which increased considerably after 30 days of corrosion. The average pit depth after 45 days of corrosion was about 90 µm with the deepest pit having about 330 µm depth. This is about 30% penetration in to the sample and it might have a great impact on the strength. Also, after 45 days 1.5% of the sample was no longer Al and was covered with pits.

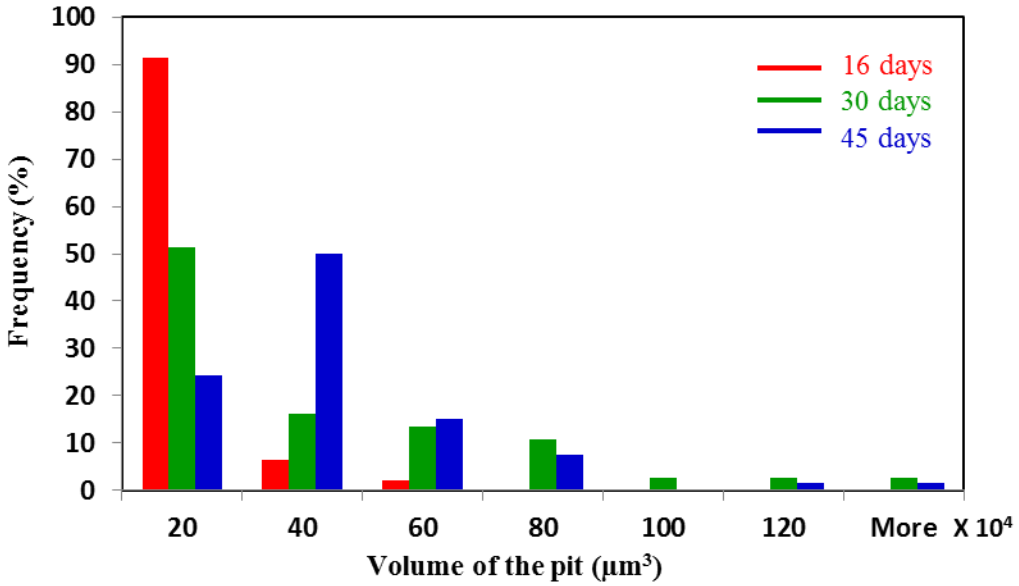

Figure 32. Frequency distribution of pit volumes at various times of corrosion.

The number of pits observed in the sampled volume decreased after 30 days of exposure likely due to coalescence of individual pits. With X-ray tomography, by obtaining the microstructure, the pit could be clearly visualized in 3D. From this, we could accurately quantify the pit dimensions with varying corrosion time which can be correlated with the mechanical properties.

Table 2. Quantitative analysis of pit sizes with corrosion

Corrosion	**No. of pits observed**	**Avg. pit depth**	**Deepest pit**	**Volume fraction occupied by pits**	**Max. volume (x 10^4)**
0 days	0	0	0	0	0
2 days	-	-	16 μm	-	-
16 days	46	22.6 ± 7.5 μm	37.7 μm	0.29 %	43.75 μm^3
30 days	37	78.3 ± 25.4 μm	159.6 μm	0.82 %	211.1 μm^3
45 days	66	90.9 ± 36.6 μm	330.2 μm	1.47 %	263.9 μm^3

4.3.3 Correlation of mechanical properties with microstructure

From the quantitative analysis, we can observe that after 45 days of corrosion, about 1.5 % of the specimen volume is covered with pits. The deepest pit observed was about 330 μm and the average pit depth was about 91 μm. This has resulted in a strength

reduction of about 70-100 MPa. The SEM image after fracture was matched with tomography slice and it was observed that the failure has occurred near the deepest pit in the entire sample (Figure 33). This indicates that maximum stress concentrated near the deepest pit in the sample and the remaining pits essentially contributed to the decrease in the load bearing capacity of the sample. After 45 days, the specimen had the deepest pit as well as the highest volume fraction occupied by pits. This implies that this specimen had maximum stress concentration as well as maximum decrease in load bearing capacity compared to other samples; hence it showed the lowest strength. Figure 34 shows few plots which explain the statistical data obtained and the structure-property correlation. Figure 34 (a) shows that the depth of the deepest pit observed in the specimens increased with corrosion. This implies that there would be maximum stress concentration with increase in corrosion and the corresponding decrease in tensile strength can be observed. Figure 34 (b) shows the increase in volume fraction of the specimen occupied by pits with corrosion. This indicates that the decrease in load bearing capacity of the samples increases with corrosion, hence, showing a decrease in tensile strength. Figure 34 (c) shows the decreasing trend between tensile strength and average pit depth. After 45 days of corrosion of Al in 3.5 wt.% NaCl, the average pit depth was about 91 μm and it has resulted in a decrease in strength of about 100 MPa.

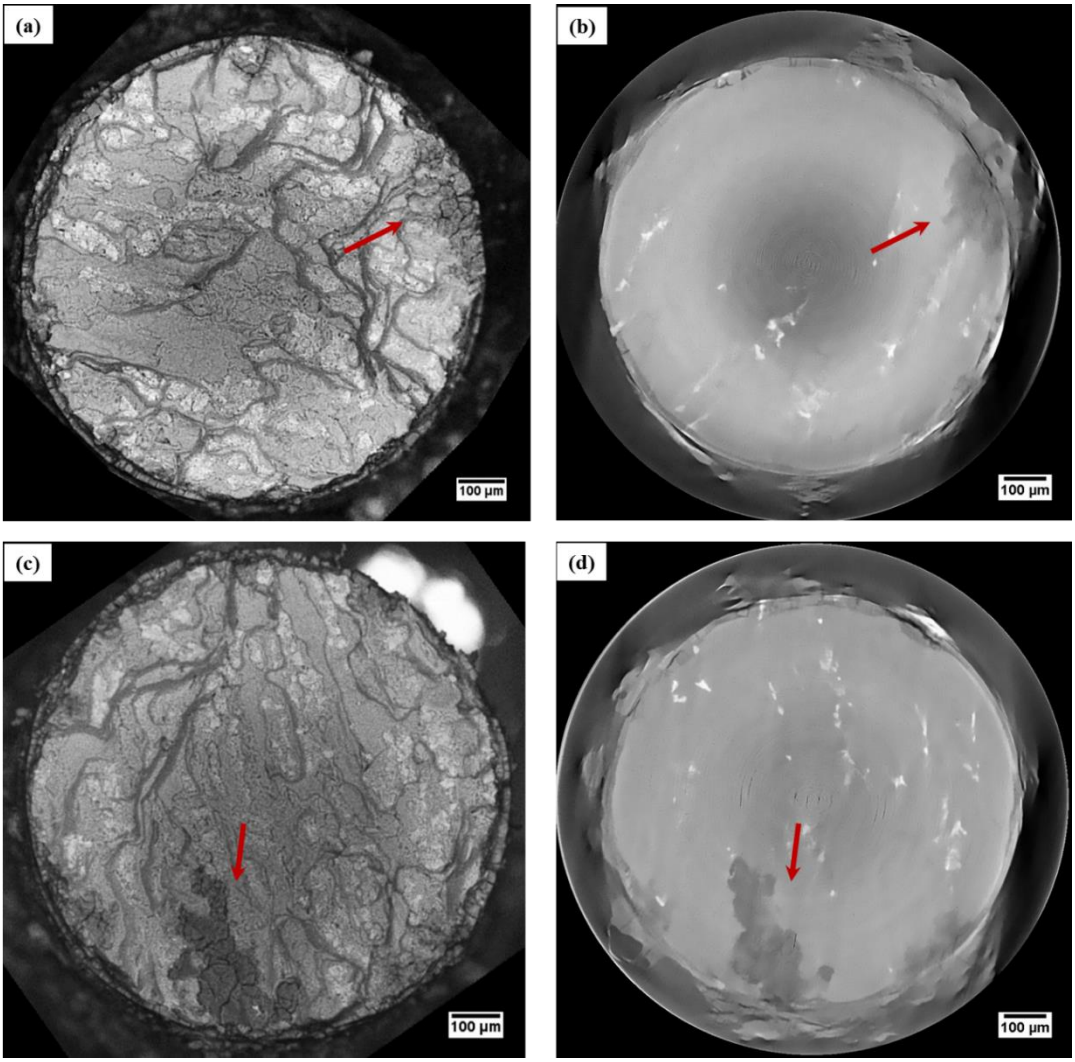

Figure 33. (a, c) Fracture surface after 30 and 45 days of corrosion (b, d) X-ray tomography slice of the deepest pit in the entire sample after 30 and 45 days of corrosion.

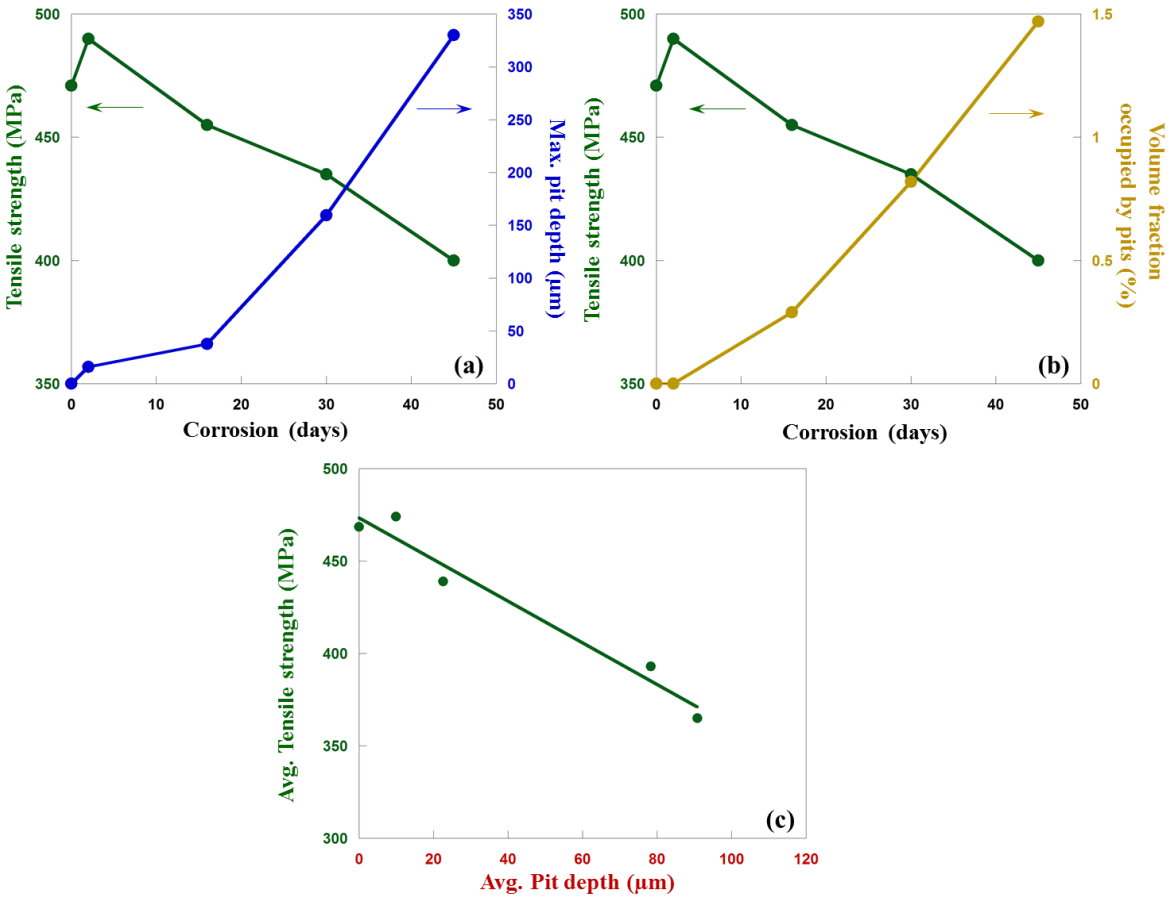

Figure 34. Plots showing (a) strength vs. maximum pit depth (b) strength vs. volume fraction of pits with corrosion (c) strength vs. average pit depth.

4.3.4 Monitoring pit growth

This section shows the evolution of pits with corrosion. X-ray tomography scans were performed once after every 2 days of corrosion and the pit growth is monitored till 20 days. Individual pits were located on the sample and their growth was monitored. The growth of one such pit at different times of corrosion can be seen in Figure 35. Trenching starts around the bright Fe-rich inclusion after about 8 days of corrosion forming a pit.

This pit has increased in its size with further increase in corrosion reaching a depth of about 30 µm after 20 days of corrosion.

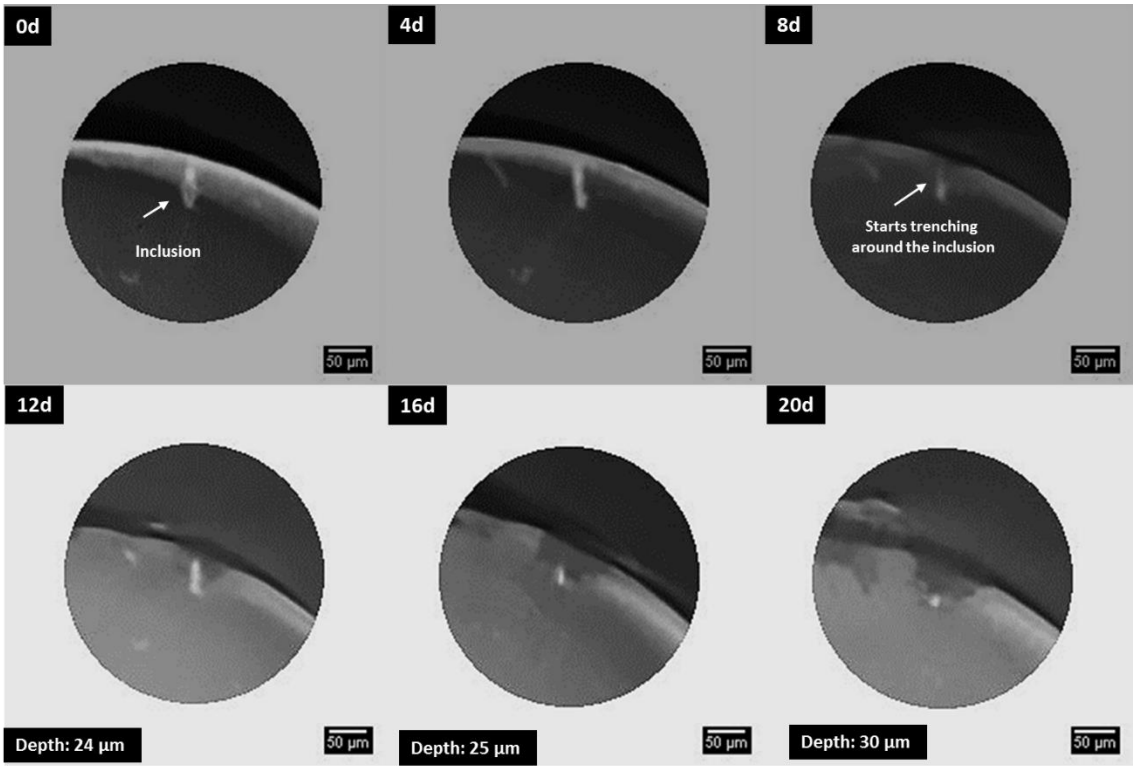

Figure 35. Pit evolution with corrosion (0 – 20 days). The pit starts to form after about 8 days and increases its size with further corrosion.

After prolonged time of exposure, coalescence of individual pits has been observed (Figure 36) which could result in a more extensive localized corrosion attack. Figure 36 (a) shows two individual pits after 16 days of corrosion. After 20 days of exposure, these pits have been coalesced and can be observed in Figure 36 (b).

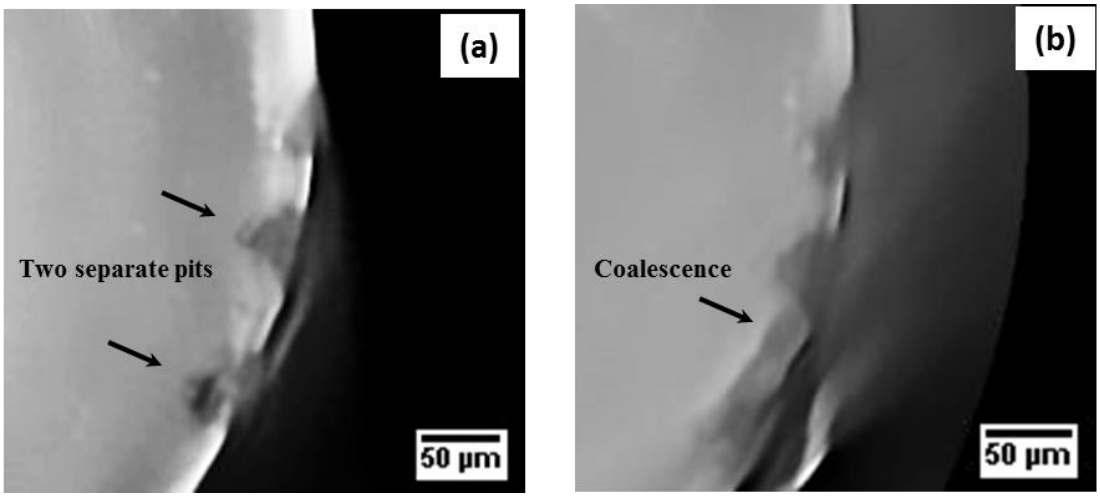

Figure 36. (a) Specimen after 16 days of corrosion showing individual pits (b) Specimen after 20 days of corrosion showing pit coalescence.

The information obtained could be useful for developing models for growth of pits. These microstructural data sets can also be incorporated in to various models to elucidate the effect of corrosion on the mechanical behavior of Al alloys.

4.4 Summary

Overall, we studied the effect corrosion can have on the tensile strength of Al 7075 alloys and correlated it with the microstructure. We could visualize the pits in 3D at different stages of corrosion and quantify their dimensions accurately. The pits are discontinuities in the sample and they are no longer aluminum. The salts comprising the pits showed severe compositional modification suggesting the deleterious effect these might have on the strength of the alloy. On application of stress, these might be the sites for stress concentration resulting in crack initiation. The knowledge about 3D structure of the pit, pit dimensions, and their correlation with the mechanical strength could be very

useful for better understanding of stress corrosion cracking. The experimental results could also be useful for supporting modeling approaches to model the damage region in corrosion of Al alloys. Achieving such scale of information and with such accuracy wouldn't have been possible with conventional 2D techniques.

4.5 References

[1] E.A. Starke Jr., J.T. Staley, Progress in Aerospace Sciences. 1996; 32: 131.

[2] A. AlHazaa, T.I. Khan, I. Haq, Mater Charact. 2010; 61: 312.

[3] C.M. Cepeda-Jimenez, J.M. Garcia-Infanta, O.A. Ruano, F. Carreno, J. Alloys Comp. 2011; 509: 8649.

[4] Arsenault, B., Simard, S., Marcoux, P., & Ghali, E. (2006, January 1). Stress Corrosion Cracking Mitigation of 7075-T6 Aluminum Alloy by Thermal Spray Coating. NACE International.

[5] B.W. Samuels, K. Satoudeh, R.T. Foley, Corrosion. 1981; 37: 92.

[6] M. Baumgaertner, H. Kaesche, Corros. Sci. 1990; 31: 231.

[7] J. Davis (Ed.), Corrosion of aluminum and aluminum alloys (2nd ed.), ASM International, USA (1999), pp. 25–49.

[8] Z. Szklarska-Smialowska, Corros Sci. 1999; 41: 1743.

[9] B. Shaw, G. Davis, W. Moshier, G. long, R. Black, J Electrochem Soc. 1991; 138: 3288.

[10] C.M.A. Brett, Corros. Sci. 1992; 33: 203.

[11] R. Ambat, E.S. Dwarakodasa, J. Appl. Electrochem. 1994; 24: 911.

[12] W. Carrol, C. Breslin, Br Corros J. 1991; 26: 255.

[13] P. Natishan, E. McCafferty, G. Hubler, Proceedings- The electrochemical society. Pennington, 86–7 (1986), pp. 437–449.

[14] R. Horst, Mater Perform. 1977; 16: 23.

[15] T.H. Nguyen, R.T. Foley, J. Electrochem. Soc. 1979; 126: 1855.

[16] L.F. Lin, C.Y. Chao, D.D. Macdonald, J. Electrochem. Soc. 1981 ; 128 : 1194.

[17] G. Bereket, A. Yurt, Corros sci. 2001; 43: 1179 .

[18] D.A. Horner, B.J. Connolly , S. Zhou, L. Crocker, A. Turnbull, Corros. Sci. 2011; 53: 3466.

[19] G.S. Chen, M. Gao, and R.P. Wei, Corrosion. 1996; 52: 8.

[20] S. Chen, K.-C. Wan, M. Gao, R.P. Wei, and T.H. Flournoy, Mater.Sci. Eng. 1996; A219: 126.

[21] R.S. Piascik and S.A. Willard:Fat. Fract. Eng. Mater. Struct. 1994; 17: 1247.

[22] S. Barter, P.K. Sharp, G. Clark, Eng. Fail. Anal. 1994; 1: 255.

[23] Hosni Ezuber, A. El-Houd, F. El-Shawesh, Mater. Des. 2008; 29: 801.

[24] K.K. Sankaran, R. Perez, K.V. Jata, Mater. Sci. Eng., A. 2001; 297: 223.

[25] D.L DuQuesnay, P.R Underhill, H.J Britt, Int. J. Fatigue. 2003; 25: 371.

[26] G. Bereket, A. Yurt, Corros. Sci. 2001; 43: 1179.

[27] R.S. Sidhu, N. Chawla, Scr. Mater. 2006; 54: 1627.

[28] E. Padilla, V. Jakkali, L. Jiang, N. Chawla, Acta Mater. 2012; 60: 4017.

[29] J.J. Williams, Z. Flom, A.A. Amell, N. Chawla, X. Xiao, F. De Carlo, Acta Mater. 2010; 58: 6194.

[30] J.J. Williams, N.C. Chapman, V. Jakkali, V.A. Tanna, N. Chawla, X. Xiao, F. De Carlo, Metall. Mater. Trans. A. 2011; 42: 2009.

[31] Kimberli Jones, David W. Hoeppner, Int. J. Fatigue. 2009; 31: 686.

[32] N. Birbilis, M.K. Cavanaugh, R.G. Buchheit, Corros. Sci. 2006; 48: 4202.

[33] Minhua Shao, Yan Fu, Ronggang Hu, Changjian Lin, Mater. Sci. Eng,. A. 2003; 344: 323.

[34] Sudhanshu S. Singh, Jason J. Williams, Tyler J. Stannard, Xianghui Xiao, Francesco De Carlo, Nikhilesh Chawla, Corros. Sci. 2016 ; 104 : 330.

[35] Sudhanshu S. Singh, Jason J. Williams, X. Xiao, F. De Carlo and N. Chawla, Fatigue of Materials II Advances and Emergences in Understanding, Edited by: T.S. Shvatsan, M. Ashrafimam. and R. Srinivasan TMS (The Minerals, Metals & Materials Society), 20.

[36] S. S. Singh, J. J. Williams, M.F.Lin, X. Xiao, F. De Carlo and N. Chawla, Mater.Res.Lett. 2014; 2: 217.

[37] Y. Nakai and D. Shiozawa, EPJ Web of Conferences 6, 35004 (2010).

[38] S.P. Knight, M. Salagaras, A.R. Trueman, Corros. Sci. 2011; 53: 727.

[39] T.J. Marrow, L. Babout, B.J. Connolly, D. Engelberg, G. Johnson, J.-Y. Buffiere, P.J. Withers and R.C. Newman, High-resolution, in-situ, tomographic observations of stress corrosion cracking.

[40] J.J. Williams, K.E. Yazzie, E. Padilla, N. Chawla, X. Xiao, F. De Carlo, Int. J. Fatigue. 2013; 57: 79.

[41] Sudhanshu S Singh, Jason J Williams, Peter Hruby, Xianghui Xiao, Francesco De Carlo and Nikhilesh Chawla, Integrating Materials and Manufacturing Innovation. 2014; 3: 9.

[42] J.C.E. Mertens, J.J. Williams, Nikhilesh Chawla, Mater. Charact. 2014; 92: 36.

[43] Y. Yeh, W. Liu, Metall. Mater. Trans. A. 1996; 27A: 3558.

[44] A. Balasundaram, A.M. Gokhale, S. Graham, M.F. Horstemeyer, Mater. Sci. Eng. A. 2003; 355: 368.

[45] T.G. Dunford, B.E. Wilde, in: M.E. Blum, P.M. French, R.M. Middleton, G.F. Vander Voort (Eds.), Microstructure Science, vol. 15, American Society for Metals, Metals Park, OH, and International Metallographic Society, Columbus, OH, pp. 263, 1987.

CHAPTER 5

CHARACTERIZATION OF THE CORROSION INDUCED DAMAGE LAYERS IN 7075 ALUMINUM (AL) ALLOYS

5.1 Introduction

7075 aluminum alloys are widely used in various industries due to their high strength-to-weight ratio [1-4]. When aluminum alloys are exposed to atmosphere, a thin oxide film forms spontaneously which acts as a protective layer and inhibits the further oxidation of the underlying metal. This self-protecting characteristic makes aluminum alloys usually corrosion resistant in a wide range of media [5-8]. But in certain medium for e.g. containing chloride ions, this oxide film loses its protective nature and can readily undergo various corrosion reactions [6-12] thereby reducing the service life of the components. Corrosion can have a severe effect on aluminum alloys life resulting in their catastrophic failure, and they are also known to be highly susceptible to stress corrosion cracking (SCC) [12, 13].

When aluminum alloys are exposed to environments containing chloride ions, the oxide film breaks down at weak points resulting in localized corrosion and the formation of pits [14 - 16]. A corrosion product layer with the presence of cracks has also been observed in this study. These pits and corrosion products can be sites for cracks nucleation and propagation resulting in stress corrosion cracking. This is because in the corroded region, damage creates weak spots, embrittlement, and heterogeneities in the materials strength and elasticity from where cracks can develop, thus leading to potential for unstable crack growth and material failure. Therefore, it is very important to

investigate the microstructure and mechanical properties in the damaged region near the corrosion surface. This work focuses on studying the corrosion layers while pitting was characterized in a separate work.

Apart from the outer corrosion layer observed, a diffuse corrosion layer or a partially corroded region was observed on corrosion of 7075 aluminum alloy in 3.5 wt.% NaCl in this study. This damage region beyond the corrosion layer has been extensively studied in magnesium alloys [17, 18]. The presence of two layers of corrosion film in 7075 aluminum has also been reported [19]. This partially corroded region indicates a diffuse layer in which NaCl has penetrated through, immediately below the corrosion product layer resulting in partial corrosion [17]. This shows that the damaged region extends beyond the corrosion product layer leading to microstructural changes and possible reduction in mechanical properties. The goal of this work, hence, is to investigate the structure, mechanical properties, composition of the damaged region and locate the diffuse layer. This is particularly important since this diffuse corrosion layer is a part of the bulk alloy and can also act as sources of crack initiation or a medium for cracks to propagate that initiated at the corrosion product layer [17].

Peridynamic models have been introduced to computationally model this subsurface damage layer previously and were successful in capturing the evolution of damage from corrosion [20, 21]. Mechanical characterization as well as chemical compositional analysis in the corrosion damage layer in the present study would help in calibrating such numerical models, of corrosion-induced damage in aluminum alloys. In this work, we considered commercially available 7075 aluminum alloy and corroded it in 3.5 wt.% NaCl solution to study the damage region. Multiple samples were corroded

and removed at different times for comparison. The structure of the corroded region was characterized using SEM and compositional variation in the different layers was studied using EDX. Nanoindentation was used to accurately determine the Young's modulus and hardness of the damaged region. Knowledge of the structure, composition and mechanical properties of the corrosion damaged region along with the identification of sub surface partially corroded region will allow us to better understand corrosion process in aluminum 7075 alloys and to more accurately model their behavior.

5.2 Materials and experimental procedure

The material used in this study was a commercially available 7075-T651 aluminum alloy. Round test specimens with dog bone specimen geometry (diameter = 1mm) were machined by electro-discharge machining such that the longest dimension (length = 22 mm) was along the short-transverse (S-T) orientation. Specimens were polished to a 1 μm diamond finish and then sonicated in acetone to remove any debris. The polished specimens were then exposed to 3.5 wt.% NaCl solution and removed after different times (0, 2, 16, 30, 45 days). After corrosion in NaCl, the corroded samples were cut by a diamond saw from the middle of the corroded surface and the as-obtained cross-sections were mounted in epoxy. These are then ground and polished for further characterizations. Characterization of the corroded samples was done by a dual-beam FIB/SEM (Carl Zeiss Auriga) coupled with an energy dispersed X-ray spectroscopy system (EDX). The structure of the corroded region was visualized by imaging using the SEM and compositional analysis was performed using EDX. Micromechanical properties

of the corroded samples were analyzed by nanoindentation tests using a commercial nanoindenter (Nanoindenter XP-II, Agilent). Indentation was carried out using continuous stiffness measurement technique (CSM) with a berkovich tip to a depth of 400 nm per indentation. Multiple indentations were carried out in the regions of interest and Young's modulus, hardness for individual indentations were measured. SEM was used after indentation to verify the location of the indents.

5.3 Results and Discussion

On immersion in NaCl solution, the surface of the sample was found to be entirely covered with a corrosion layer (Figure 37 (a)). Corrosive species tend to attack the surface metal and result in a complete modification of the surface layer. Chemical composition analysis by EDX on the surface (Figure 37 (b and c)) revealed that the surface layer was primarily composed of oxygen and aluminum with low concentrations of zinc, sodium and chlorine. The ratio between Al and O observed was about 0.5 - 0.6 indicating that this layer is likely $Al(OH)_3$ along with sodium and chloride ions in it.

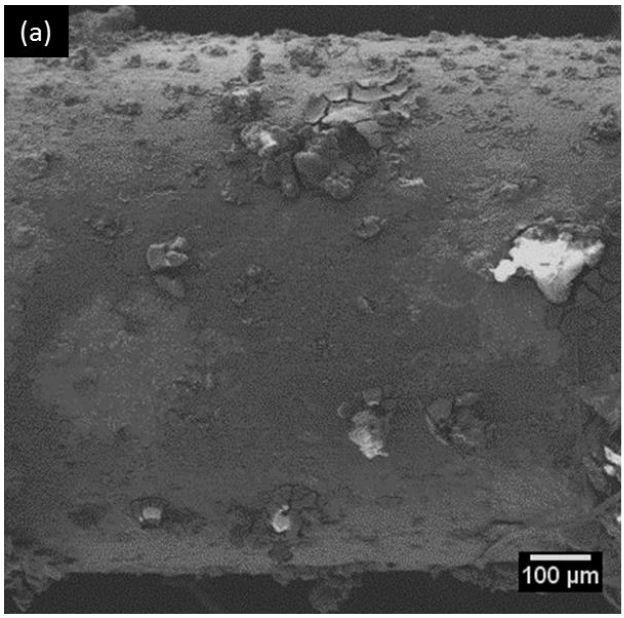

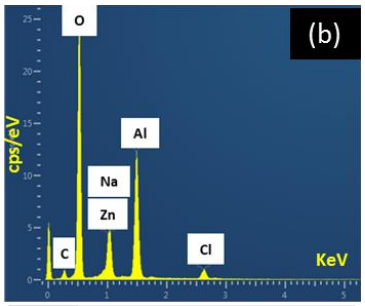

(c)	Composition (Wt. %)
O	50.3 ± 0.9
Al	25.2 ± 0.2
Zn	9 ± 0.06
Na	5.7 ± 0.1
C	6.1 ± 0.7
Cl	3.7 ± 0.05

Figure 37. (a) Corrosion layer on the surface of the sample (b and c) EDX spot scan results showing the high oxidation as well as the incorporation of Na and Cl ions due to corrosion.

Figure 38 shows the cross-sections of the corroded samples with the corrosion layer. The cross-section after 2 days (Figure 38 (a)) did not show the presence of this layer while it was observed after 16 days of corrosion (Figure 38 (b)). The thickness was about 30 µm after 30 days (Figure 38 (c)) and it did not increase considerably after 45 days of corrosion (Figure 38 (d)).

Micro-cracks were evident in the surface corrosion layer on high magnification imaging as seen in Figure 39. which would have occurred during the drying process after removing the sample from the corrosive liquid. This phenomenon referred to as mud cracking has been reported in many corroded alloys and the mechanism is reported elsewhere [17, 22 - 24]. The presence of cracks can facilitate ion diffusion beneath the surface and hence the surface corrosion layer cannot effectively protect the underlying

metal. This results in further propagation of corrosion damage beyond the surface layer forming a partially corroded region. This has also been previously observed in Magnesium alloys and is found to have a significant reduction in mechanical properties compared to the un-corroded alloy [17].

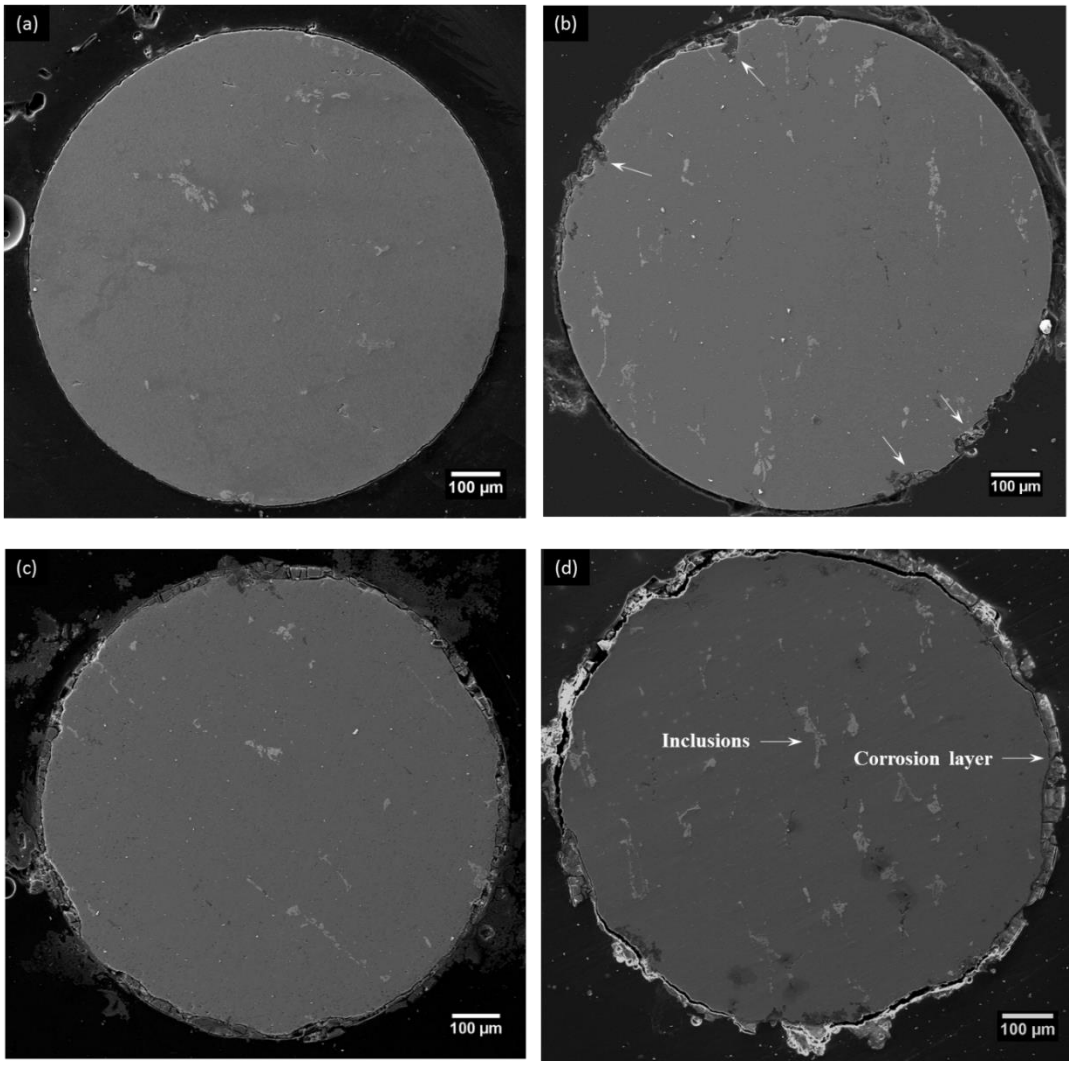

Figure 38. Cross-sections of the sample corroded for: (a) 2 days showing no corrosion layer (b) 16 days showing the corrosion layer in certain regions as indicated by the arrows (c and d) 30 days and 45 days showing a continuous corrosion layer covering almost the entire sample.

Figure 39. Micro-cracks on the corrosion layer which serve as pathways for ion diffusion beyond the surface corrosion layer.

SEM observation alone could not reveal the partially corroded region. EDX techniques (elemental mapping and line scans) were performed near the corrosion surface on the cross-sectioned samples to analyze the compositional variation and thereby identify the partially corroded region. Figure 40 shows the EDX mapping of different elements (Al, O, Na, Cl) across the corroded region. In the regions, where high concentration of O was observed, there was a low concentration of Al. The presence of ions in the corrosion layer as well as beyond it can be observed indicating that the surface layer allows for the diffusion and hence propagating the damage region even beyond it.

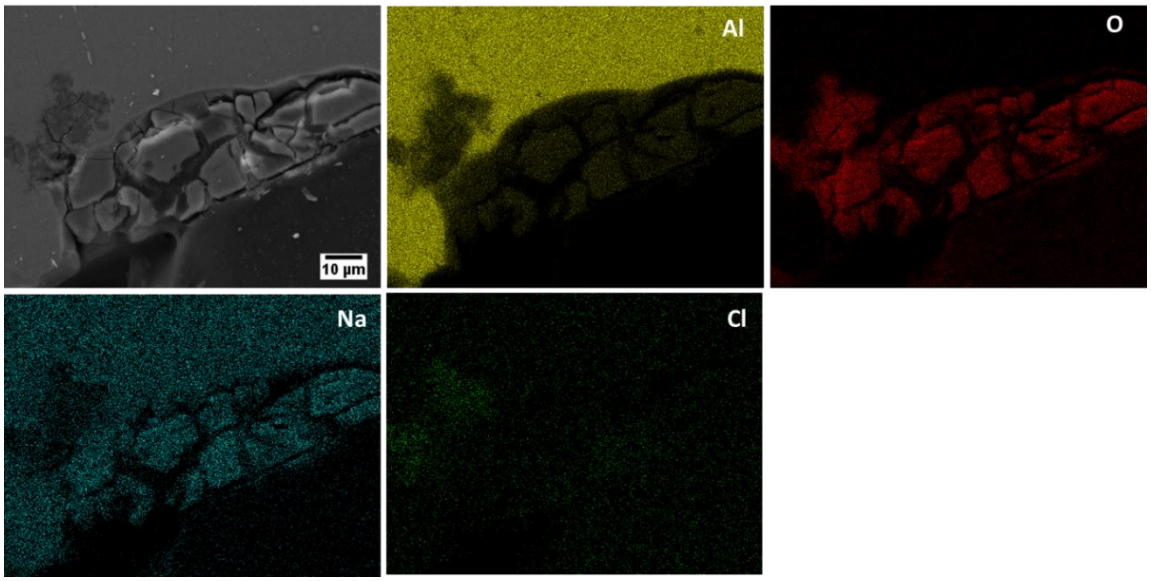

Figure 40. EDX mapping on corrosion induced damge region which shows the presence of Na and Cl ions beyond the corrosion layer resulting in damage propagating beyond the surface corrosion layer in to the bulk. Also, the high amount of O concentration and depletion of Al can be observed in the corroded layer.

To quantify the compositional variation across the damaged region, EDX line scan analysis was performed across the corroded region (Figure 41). Un-corroded bulk alloy consists primarily of Al and low concentration of O while uniform corrosion layer was found to be highly oxidized. The ratio between Al and O in this region was found to be about 0.5 - 0.6. Small amounts of sodium and chlorine were also observed in this region. A region in which the chemical composition gradually changes was also observed sandwiched in between the bulk Al and the corrosion layer. In this region, Al concentration gradually decreases and O concentration increases moving towards the corrosion layer. This gradual variation in the composition is a result of the diffusive nature of the ions beyond the corrosion layer as mentioned previously resulting in a

partially corroded region. This shows that the damage in not only limited to the outer corrosive layer but also a region adjacent to it is affected resulting in a partially corroded region. This region acts as a transit between the bulk alloy and the corrosion layer and it is important to understand it's properties since it might also influence the performance of the alloy. Also, the thickness of this partially corroded region was found to be about 3 – 4 µm and the thickness, compositional variation in this region was found to be independent of the immersion time. There are no significant differences in the surface morphology of the partially corroded region to be able to identify it by imaging alone and the EDX technique helped in identifying it.

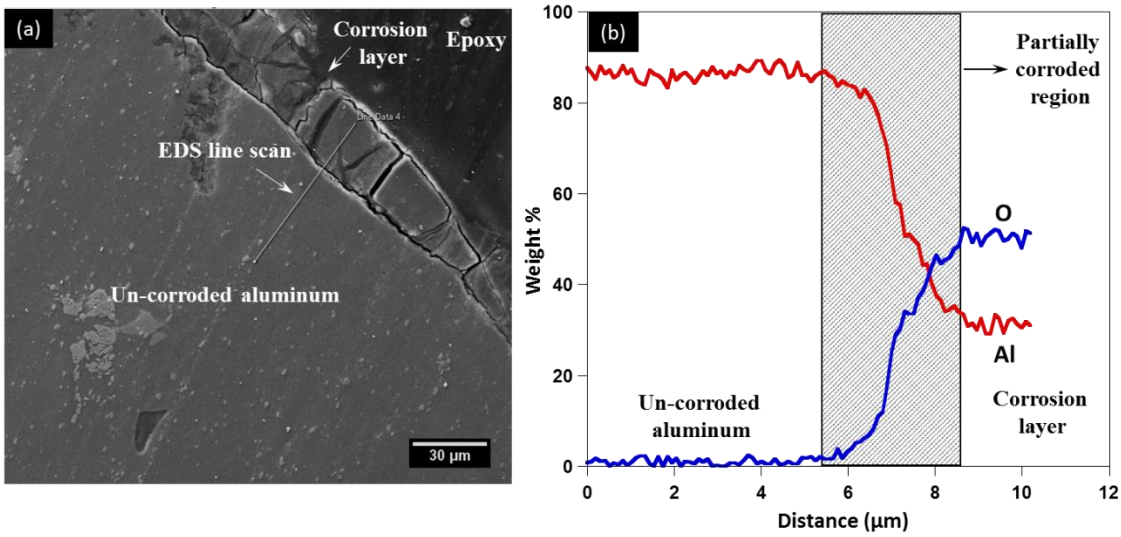

Figure 41. (a) EDX line scan analysis on the cross-section covering the corroded layer and un-corroded aluminum to check for the presence of the partially corroded region (b) Results show a tri-layer structure (Un-corroded Al, partially corroded region and corrosion layer). The partially corroded region acts as a transition layer (patterned) with a gradual change in composition of Al and O.

Based on the above discussion, a tri-layer structure exists in the corroded alloys- corrosion layer, partially corroded region and uncorroded region. The presence of defects and the compositional variation in the corroded regions suggest that the mechanical properties in these would also be effected. It is important to understand the mechanical properties variation in these different regions to be able to gain a comprehensive understanding of corrosion and its effect on aluminum. Since the regions to characterize are very small, especially the partially corroded region being only 3 – 4 μm in thickness, it is necessary to use a technique which can probe localized and small regions accurately. Nanoindentation is one such attractive technique which can quantitatively characterize the mechanical properties of small volumes of material and hence it is used here to measure the elastic modulus and hardness of the different regions in the corroded specimens. Imaging in SEM post nanoindentation revealed the exact location of the indentations in the different regions (Figure 42). As CSM technique is utilized in this work, where the modulus and hardness can be obtained continuously with depth, this results in an accurate measurement of modulus and hardness compared to conventional nanoindentation technique. The partially corroded region is the thinnest of the three regions to be characterized here (3 – 4 μm) and care must be taken such that the size of the indentations should be below the thickness for accurate results. Since the size of the indent depends on the depth till which indentation is carried out, a depth of 400 μm was chosen. Tests in this depth regime not only yielded indentations that lied within the partially corroded region but also provided reliable data. The same depth was used for the remaining two regions as well. Also, sufficient spacing was maintained between the indentations to exclude any interaction effect.

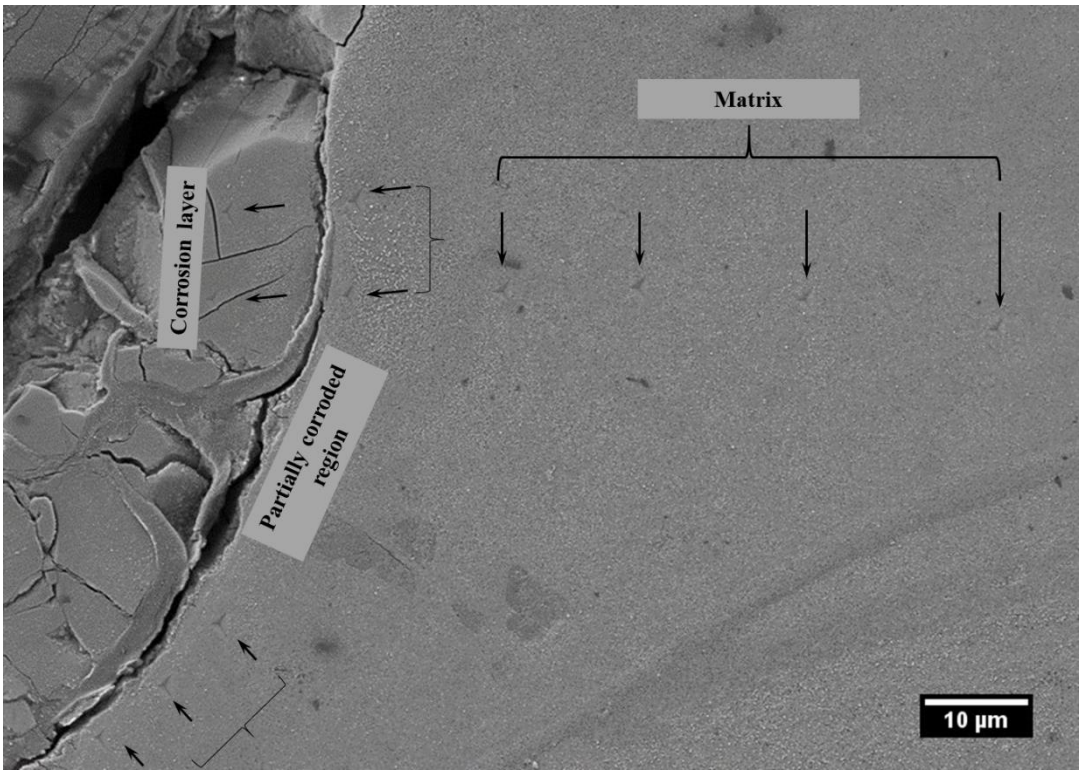

Figure 42. Nanoindentation performed on the tri-layer structure (Un-corroded Al, partially corroded region and Corrosion layer). The black arrows show the location of the indents.

Multiple tests were conducted in each region for accuracy and reliability. Representative Young's modulus, hardness curves as a function of the depth for different regions are shown in Figure 43, Figure 44 respectively, and Table 3, Table 4 summarize these measurements. The Young's modulus and hardness values were taken as the average values where there is a plateau in the curves which is indicated by the dotted lines in the figures. The modulus was found to be highest in the un-corroded region, 84.5 GPa and was similar to the value observed in the literature of 7075 Al [25].

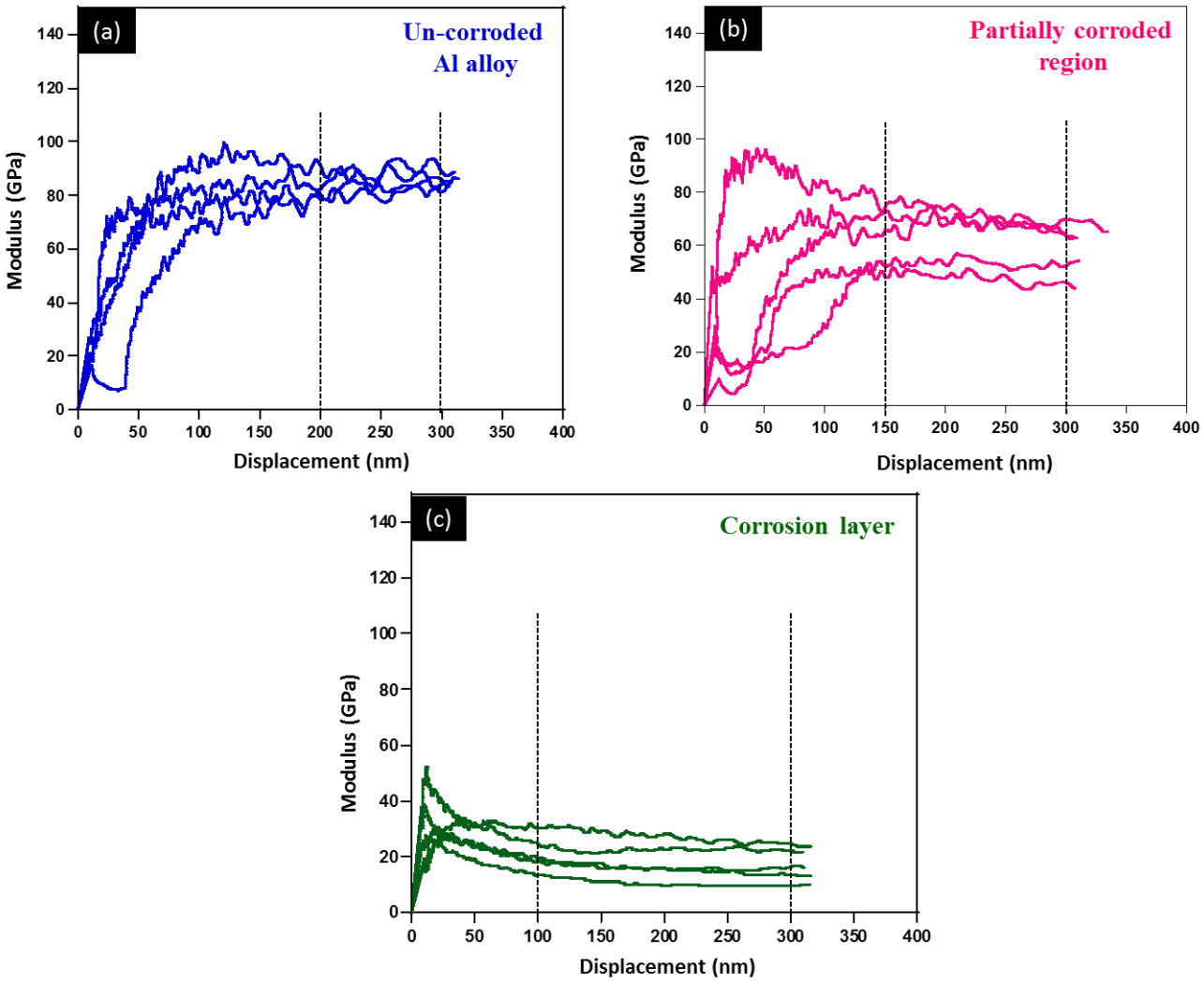

Figure 43. Young's modulus – displacement curves in the tri-layer structure (a) Un-corroded Al alloy (b) Partially corroded region (c) Corrosion layer showing a decrease in modulus from region a to c. The modulus values are averaged from where the curves plateau (indicated by the dotted lines).

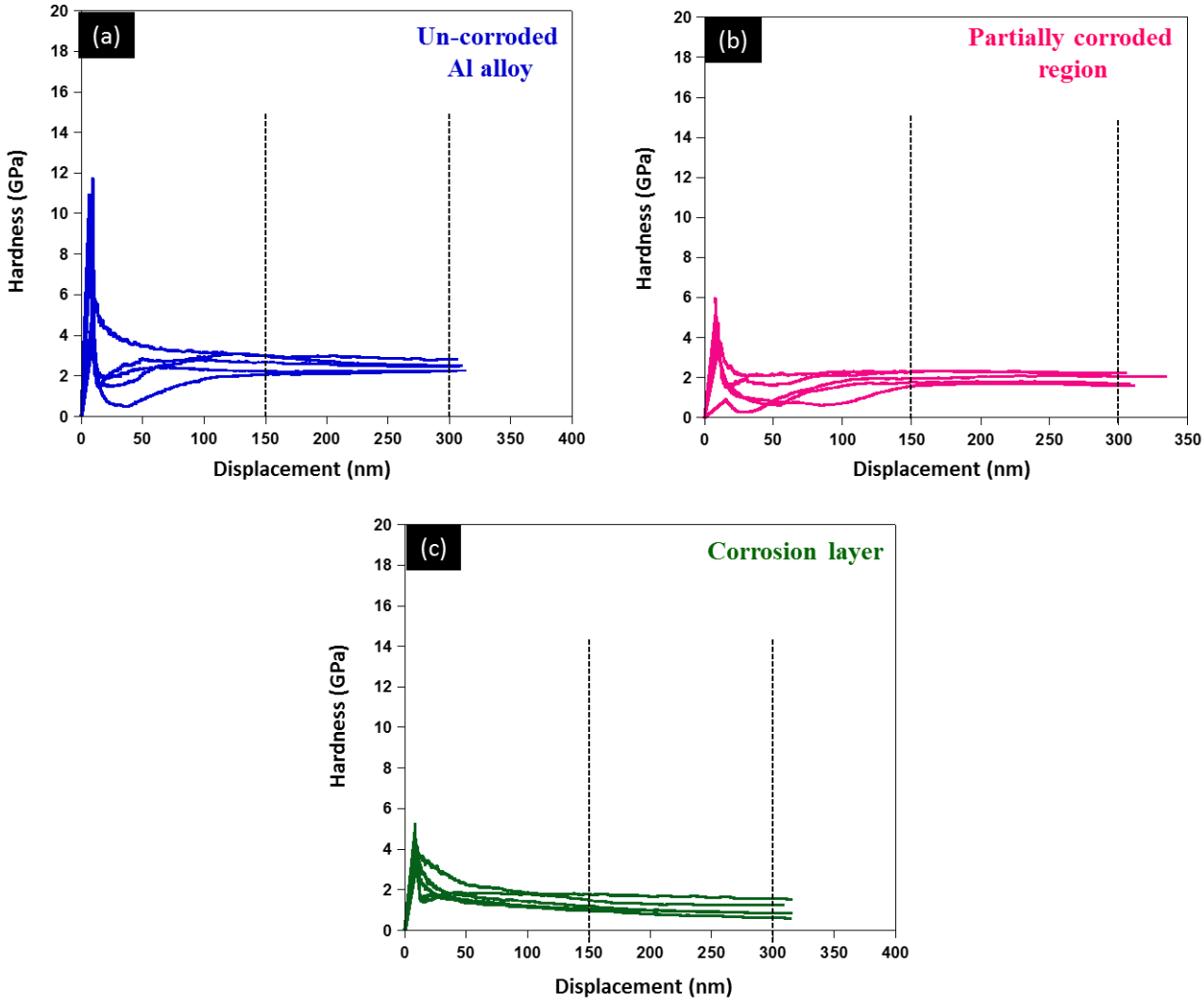

Figure 44. Hardness – displacement curves in the tri-layer structure (a) Un-corroded Al alloy (b) Partially corroded region (c) Corrosion layer showing a decrease in hardness from region a to c. The hardness values are averaged from where the curves plateau (indicated by the dotted lines).

Table 3. Young's modulii of the Al 7075 matrix, partially corroded region and the corrosion layer

Region	Al matrix	Partially corroded region	Corrosion layer
Modulus (GPa)	84.5 ± 4	59.3 ± 9.1	18.7 ± 6.6

Table 4. Hardness of the Al 7075 matrix, partially corroded region and the corrosion layer

Region	Al matrix	Partially corroded region	Corrosion layer
Hardness (GPa)	2.5 ± 0.3	2 ± 0.4	1.1 ± 0.4

The modulus in the corroded regions are much smaller than this indicating the significant mechanical modification introduced by corrosion. The corrosion layer was found to be with the lowest stiffness among the three regions (18.7 GPa) and this could be understood not only because of the cracks observed but also because of the severe modifications in its composition. The modulus in the partially corroded region was found to be heterogeneous and showed a range of values. This could be expected because of the gradual change in composition observed in the previous section. The modulus in this region gradually decreased moving towards the corrosion layer and varied in between 40

to 75 GPa (with an average of 59.3 GPa). The hardness was also also found to follow a similar trend as shown in Figure 42. The hardness in the matrix was highest, 2.5 GPa and lowest in the corrosion layer, 1.1 GPa. The hardness in the partially corroded region was found to be intermediate between these two regions and showed a gradual change with distance from the corrosion layer (varied between 1 to 2.5 GPa with an average of 2 GPa). Overall, there wasn't much change in the hardness of the three regions indicating it would be difficult to separate the corroded region from the un-corroded alloy. The same trend of mechanical properties was observed in specimens corroded for different days. From the considerable reduction in the modulus and hardness values as noted above, we can understand the deleterious effect corrosion can have on the mechanical performance of the alloy.

Overall, there is a significant effect of corrosion on the composition and mechanical properties of Al alloys. With increase in corrosion time, the composition and mechanical properties variation in the damaged region remained the same with the only difference being an increase in the thickness of the outer corrosion layer. The mechanical properties variation in the different regions is a consequence of the modification of composition due to corrosion. Figure 45 shows the variation of both composition and mechanical properties in the different regions. In the partially corroded region, as we move towards the corrosion layer, the composition of Al is found to gradually decrease and a corresponding decrease in the modulus and hardness can be noted (Figure 45). One side of this partially corroded region is found to have composition, mechanical properties same as the corrosive layer, and another side same as the bulk un-corroded alloy. On the other hand, in the corrosion layer, which is highly oxidized with low concentration of Al,

the mechanical properties were the lowest. It can be seen that not only the outer corrosion layer but also the partially corroded region can also play an important role on the performance of the alloy owing to the significant changes in composition and mechanical properties in this region. On application of stress, these corrosion damaged regions can provide sites for crack initiation resulting in stress corrosion cracking and failure of the material. The partially corroded region can not only provide sites for crack initiation but also may provide an easier path for propagating the cracks initiated in the outer corrosion layer in to the bulk. Therefore, the partially corroded region along with the outer corrosive layer can have a significant effect during stress corrosion cracking and it is important to study and understand the properties of these regions. The experimental results obtained in this work could not only help in better understanding of corrosion in Al and hence stress corrosion cracking but also can be used for supporting modeling approaches to model the damage region.

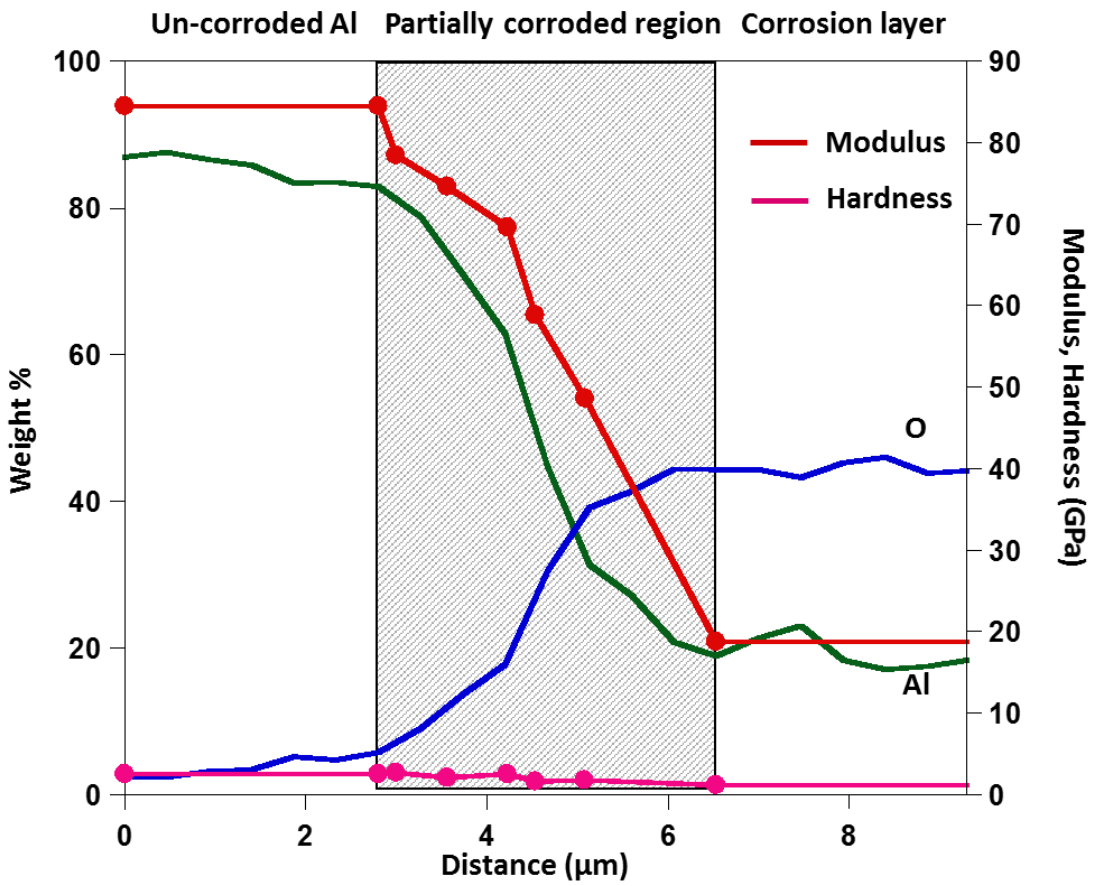

Figure 45. Variation of mechanical properties and compostion in the tri-layer structure (Un-corroded Al, partially corroded region and Corrosion layer). Mechanical properties follow the same trend as the composition; with the decrease in Al concentration from left to right, a corresponding decrease in them can be observed.

5.4 Summary

We have studied the microstructure, composition and mechanical properties of the corroded region in 7075 Al alloy corroded in 3.5 wt.% NaCl solution. A tri-layer structure composed of the bulk Al alloy, partially corroded region and the surface corrosion layer has been observed. The surface corrosion layer was found to be filled with cracks whereas there wasn't any morphological change observed in the partially

corroded region. EDX analysis helped to identify this partially corroded region which extended about 3 – 4 μm in to the bulk and this thickness was found to be independent of the immersion time. While the outer corrosion layer was found to be highly oxidized, the partially corroded region showed partial oxidation with gradual changes in composition. This induces gradual changes in mechanical properties as well, showing a reduction in properties as we move towards the corrosion layer. On application of stress, these corrosion damaged regions can provide sites for crack initiation resulting in stress corrosion cracking and failure of the material.

5.5 References

[1] E.A. Starke Jr., J.T. Staley, Progress in Aerospace Sciences. 1996; 32: 131.

[2] A. AlHazaa, T.I. Khan, I. Haq, Mater. Charact. 2010; 61: 312.

[3] C.M. Cepeda-Jimenez, J.M. Garcia-Infanta, O.A. Ruano, F. Carreno, J. Alloys \ Comp. 2011; 509: 8649.

[4] Arsenault, B., Simard, S., Marcoux, P., & Ghali, E. (2006, January 1). Stress Corrosion Cracking Mitigation of 7075-T6 Aluminum Alloy by Thermal Spray Coating. NACE International.

[5] Davis, J. R. (2000), Corrosion of aluminum and aluminum alloys, Materials Park: ASM International.

[6] E. M. Sherif, S.-M. Park, J. Electrochem. Soc. 2005; 152: B205.

[7] W. R. Osório, N. Cheung, L. C. Peixoto, A. Garcia, Int. J. Electrochem. Sci. 2009; 4: 820.

[8] E. M. Sherif, S.-M. Park, Electrochim. Acta. 2006; 51: 1313.

[9] W. Diggle, T. C. Downie, C. Goulding, Electrochim. Acta. 1970; 15: 1079.

[10] Fang Wang, Yabin Wang, Yanni Li, Int. J. Electrochem. Sci. 2011; 6: 793.

[11] A. I. Onen, B. T. Nwufo, E. E. Ebenso, R. M. Hlophe, Int. J. Electrochem. Sci. 2010; 5: 1563.

[12] J. K. Park, Mater. Sci. Eng. A. 1988; 103: 223.

[13] H. Vogt and M. O. Speidel, Corros. Sci. 1998; 40: 251.

[14] Z. Szklarska-Smialowska, Corros. Sci. 1999; 41: 1743.

[15] W. Carrol, C. Breslin, Corros. J. 1991; 26: 255.

[16] P. Natishan, E. McCafferty, G. Hubler, Proceedings- The electrochemical society. Pennington, 86–7 (1986), pp. 437–449.

[17] Shumin Li, Ziguang Chen, Fei Wang, Bai Cui, Li Tan, and Florin Bobaru, J. Electrochem. Soc. 2016; 163: C784.

[18] W. Song, H. J. Martin, A. Hicks, D. Seely, C. A. Walton, W. B. Lawrimore, P. T. Wang, and M. F. Horstemeyer, Corros. Sci. 2014; 78: 353.

[19] Ilaria M. Comotti, Monica Trueba and Stefano P. Trasatti, Surface and Interface Analysis Special Issue: Aluminium Surface Science and Technology. 2013; 45: 1575.

[20] Z. Chen and F. Bobaru, J. Mech. Phys. Solids. 2015; 78: 352.

[21] Z. Chen, G. Zhang, and F. Bobaru, J. Electrochem. Soc. 2016; 163: C19.

[22] W. C. Neil,M. Forsyth, P. C.Howlett,C. R. Hutchinson, and B. R. W. Hinton, Corros. Sci. 2009; 51: 387.

[23] M. Hasatani and Y. Itaya, Drying Technol. 1996; 14: 1011.

[24] D. Mihoubi and A. Bellagi, Transp. Porous Media. 2009; 80: 519.

[25] Sudhanshu S. Singh, Cary Schwartzstein, Jason J. Williams, Xianghui Xiao, Francesco De Carlo, Nikhilesh Chawla, J. Alloys Cmpnd. 2014; 602: 163.

CHAPTER 6

CONCLUSION

6.1 Summary of research findings and future work

Structural and mechanical characterization of environmental-induced damage resulting in whiskering in tin and corrosion in aluminum 7075 alloys has been performed. This resulted in a better understanding of the structure and properties of the damaged region which could be helpful to design alloys that can better withstand failures. The primary outcomes of this research are listed below.

6.1.1 *In Situ* FIB/SEM tensile testing of tin (Sn) whiskers

1) Accelerated growth techniques were used to probe tin whiskers required for the tests. Whiskers were found to nucleate and grow to relieve the compressive stresses induced in the samples. The sources of this stress and the growth of whiskers using each method were studied.
2) Tensile tests of tin whiskers *in situ* FIB/SEM using a MEMS tensile testing stage were carried out successfully ensuring maximum reliability. The whiskers showed high strengths compared to bulk tin owing to their low defect densities.
3) The behavior and the strength of the whiskers was found to be dependent on the gage length at which it was tested. Longer whiskers showed lower strengths. As the length of the whisker increases, the probability of encountering a strength limiting flaw would be higher, hence explaining the strength reduction.

4) The strength was also found to depend on the processing method. TEM investigation yielded important structural information about whiskers and hence the dependence of the deformation mechanisms on the processing method. Indented whiskers were found to be stronger than the aged ones. The strength variation observed could be understood by the fact that the stress required to move pre-existing dislocations as in aged whiskers is lower than that required for dislocation nucleation in indented whiskers.
5) It was observed that the oxide growth on whiskers is not significant even at the high temperatures exposed in this study and hence would not contribute to the variation in strength that is observed.

Future work

1) It was observed that tin whiskers can bend in response to forces such as electrostatic attraction increasing the probability of tin whisker shorts. Hence performing bending tests to study various properties of whiskers such as bending stiffness, bending strength, Young's modulus would be beneficial. Whisker can be lifted-out using FIB and attached to a metal block with Pt. Nanoindenter can be used to apply load on to the whisker *in situ* SEM in a cantilever fashion till it fails to obtain the bending properties.
2) Electron back scatter diffraction (EBSD) can be used to obtain the orientation of whiskers. Bending tests and *in situ* TEM tensile tests needs to be performed on whiskers with different orientations. This would elucidate the effect of orientation on the mechanical behavior of tin whiskers.

6.1.2 Structural and mechanical characterization of corroded region in Al alloy 7075

1) Visualization and quantification of the microstructure was done using X-ray tomography with a focus on change in dimensions of pits with increasing corrosion. The variation of tensile strength with corrosion and its relation with microstructure was also studied. About 1.5% of the entire volume of the specimen was occupied by pits after 45 days of corrosion and the average pit depth was about 91 μm. The pits formed due to corrosion for 45 days have resulted in a strength reduction of about 70-100 MPa.
2) EDX analysis on the cross-sections of the corroded samples helped to identify a partially corroded region adjacent to the outer corrosion layer which extended about 3 – 4 μm in to the bulk and this thickness was found to be independent of the immersion time. While the outer corrosion layer was found to be highly oxidized, the partially corroded region showed partial oxidation with gradual changes in composition. This induces gradual changes in mechanical properties as well and nanoindentation helped in understanding the mechanical properties variation. A reduction in the Young's modulus and hardness were observed in this region as we move towards the corrosion layer.

Future work

1) Monitoring pit growth on the same sample in different orientations (LT and ST) needs to be performed. An X-ray tomography scan needs to be performed for every 2 days of corrosion and individual pits growth should be monitored. This would provide valuable information regarding the pit growth kinetics, mechanisms as well as their dependence on the orientation in Al 7075 alloys.
2) A detailed analysis on the role of different inclusions on the initiation and propagation of pits needs to be carried out.

REFERENCES

CHAPTER 1 AND 2

[1] iNEMI Tin Whisker User Group, Recommendations on lead-free finishes for components used in high-reliability products, version 4, http://www.inemi.org/cms/ [accessed 04/15/2016].

[2] NASA, Basic info/FAQ, https://nepp.nasa.gov/whisker/background/ [accessed 03/16/2017].

[3] CALCE, Position paper on risks to high reliability electronics and associated hardware from pure tin coatings. Issued by center for advanced life-cycle engineering (CALCE), University of Maryland, 2002.

[4] NASA, Multiple examples of whisker-induced failures are documented on the NASA website, http://nepp.nasa.gov/whisker/.

[5] R.M. Fisher, L.S. Darken, and K.G. Carroll., Acta Metall. 1954; 2: 368.

[6] B.D. Dunn, Circuit World. 1976; 2: 32.

[7] C. Xu, IEEE Trans. Electron. Packag. 2005; 28: 31.

[8] Choi WJ, Lee TY, Tu KN, Tamura N, Celestre RS, Mcdowell AA, et al, proceedings of the 52nd electronics components and technology conference; May 28–31, 2002. p. 628–33.

[9] B.E. Powell and M.J. Skove, J. Appl. Phys. 1965; 36: 1495.

[10] B.D. Dunn, Eur. Space Agency (ESA) J. 1987; 11: 1.

[11] S.S. Singh, R. Sarkar, H.-X. Xie, C. Mayer, J. Rajagopalan and N. Chawla, Journal of Elec Materi. 2014; 43: 978.

[12] M. Osterman, 2002, Mitigation strategies for tin whiskers, https://www.calce.umd.edu/tin-whiskers/tinwhiskermitigation.pdf, calce-epsc, [Accessed: 03/18/2017].

[13] Rendings K H. Aluminium structures used in aerospace - Status and prospects [J]. Mater Sci Forum. 1997; 242: 11.

[14] Heinz A, Haszler A, Keidel C, Moldenhauer S, Benedictus R, Miller W S. [J]. Mater Sci Eng A. 2000; 280: 102.

[15] Williams J C, Jr Starke E A. [J]. Acta Mater. 2003; 51: 5775.

[16] Li Jin-feng, Peng Zhuo-wei, Li Chao-xing, Jia Zhi-qiang, Chen Wen-jing, Zheng Zi-qiao, Trans. Nonferrous met. Soc. China. 2008; 18: 755.

[17] B.Z. Lee, D.N. Lee, Acta Mater. 1998; 46: 3701.

[18] M.W. Barsoum, E.N. Hoffman, R.D. Doherty, S. Gupta, and A. Zavaliangos, Phys. Rev. Lett. 2004; 93: 206104.

[19] G. Stupian, Tin Whiskers in Electronic Circuits. 1992; Aerospace Report No. TR-92(2925)-7, pp. 1 - 21.

[20] B. Hampshire, L. Hymes, Shaving tin whiskers, Circuits Assembly. 2000; 50–53.

[21] Telcordia GR78-Core, Issue 1, September 1997, Physical design and manufacture of telecommunications products.

[22] Nick Vo, Mark Kwoka and Peter Bush, IEEE Trans. Electron. Packag. Manuf. 2005; 28: 3.

[23] S.M. Arnold, The Growth of Metal Whiskers on Electrical Components, Proceedings of IEEE Electrical Components Conference (1959) pp. 75-82.

[24] Directive 2002/95/EC of the European Parliament and of the Council of 27 January 2003 on the restriction of the use of certain hazardous substances in electrical and electronic equipment, official Journal of the European Union, 2003, L 37/19.

[25] R.M. Fisher, L.S. Darken, and K.G. Carroll, Acta Metall. 1954; 2: 368.

[26] C. Xu, IEEE Trans. Electron. Packag. 2005; 28: 31.

[27] S.C. Britton, Trans. Inst. Metal Finishing. 1974; 52: 95.

[28] W.J. Choi, T.Y. Lee, K.N. Tu, N. Tamura, R.S. Celestre, A.A. MacDowell, Y.Y. Bong, L. Nguyen, Acta. Mater. 2003 ; 51 : 6253.

[29] K.N. Tu, Phys. Rev. B. 1994; 49: 2030.

[30] K.S. Kumar, L. Reinbold, A.F. Bower, and E. Chason, J. Mater. Res. 2008; 23: 2916.

[31] J.W. Osenbach, J.M. De Lucca, B.D. Potterger, A. Amin, R.L. Shook, F.A. Baiocchi, IEEE Trans. EPM. 2007; 30: 23.

[32] E. Chason, N. Jadhav, W.L. Chan, L. Reinbold, K.S. Kumar, Appl. Phys. Lett. 2008; 92: 171901.

[33] W.J. Boettinger, C.E. Johnson, L.A. Bendersky, K.-W. Moon, M.E. Williams, G.R. Stafford, Acta Mater. 2005; 53: 5033.

[34] S. Arnold, Growth of metal whiskers on electrical components," Proceedings of Electrical components conference, pp. 75-82, 1959.

[35] R. Diehl and N. Cifaldi, Eliminate whisker growth on contacts by using a tin alloy plate, Insulation/Circuits, April 1976 pp. 37-39.

[36] Shih-Kang Lin, Yuhi Yorikado, Junxiang Jiang, Keun-Soo Kim, Katsuaki Suganuma, Sinn-Wen Chen, Masanobu Tsujimoto, and Isamu Yanada, J. Electron. Mater. 2007; 36: 1732.

[37] J.J. williams, N.C. Chapman, N. Chawla, J. Electron. Mater. 2013; 42: 224.

[38] K. Doudrick, J. Chinn, J. Williams, N. Chawla, K. Rykaczewski, Microelectron Reliab. 2015; 55: 832.

[39] Jung-Lae Jo, Shijo Nagao, Kyoko Hamasaki, Masanobu Tsujimoto, Tohru Sughara and Katsuaki Suganuma, J. Electron. Mater. 2014; 43: 1.

[40] Hiroyuki Moriyuchi, Yoshihiro Tadokoro, Masahide Sato, Takeshi Furusawa and Noboru Suzuki, J. Electron. Mater. 2007; 36: 220.

[41] K.N. Tu, R.D. Thompson, Acta Metall. 1982; 30: 947.

[42] W. Zhang, A. Egli, F. Schwager, N. Brown, IEEE Trans. Electron. Packag. Manuf. 2005; 28: 85.

[43] K.N. Tu, Acta Metall. 1973; 21: 347.

[44] K.N. Tu, C. Chen, A.T. Wu, J. Mater. Sci. Mater. Electron. 2007; 18: 269.

[45] M. Endo, S. Higuchi, Y. Tokuda, Y. Sakabe, Elimination of whisker growth on tin plated electrodes, International Symposium for Testing and Failure Analysis proceedings, pp. 305-311, Oct 1997.

[46] Jay Brussse, Tin whiskers: revisiting an old problem, Electronic packaging and space parts news, vol. 4, no.4, Dec 1998, http://misspiggy.gsfc.nasa.gov/ctre.

[47] John Jones, Tin whiskers and copper, tin intermetallics, Alter technology group, [accessed: 04/01/2017].

[48] M. Dittes, P. J. T. L. Oberndorff, and L. Petit, Tin whisker formation—Results, test methods and countermeasures, in Proc. 53rd. Electron. Compon. Technol. Conf., 2003, pp. 822–826.

[49] P. J. T. L Oberndorff, M. Dittes, and L. Petit, Intermetallic formation in relation to Tin whiskers, in Proc. IPC/Soldertec Int. Conf. Towards Implementation of the RHS Directive, Brussels, Belgium, Jun. 11–12, 2003, pp. 170–178.

[50] P. Oberndorff, M. Dittes, and P. Crema, Whisker formation on Sn plating, in Proc. IPC/JEDEC 5th Int. Conf.

[51] Smetana, IEEE Trans. Electron. Packag. Manuf, 2007; 30: 11.

[52] J. Cheng, F.Q. Yang, P.T. Vianco, B. Zhang, J.C.M. Li, J. Electron. Mater. 2011; 40: 2069.

[53] H. Leidecker, and J. Kadesch, Effects of Uralane Conformal Coating on Tin Whisker Growth, Proceedings of IMAPS Nordic, the 37th IMAPS Nordic Annual Conference, pp. 108-116, September, 10-13, 2000.

[54] P. Harris, The Growth of Tin Whiskers, International Tin Research Institute, pp. 1 – 19, 1994.

[55] K.S. Kim, C.H. Yu, J.M. Yang, Microelectron. Reliab. 2006; 46: 1080.

[56] Y. Nakadaira, S. Jeong, J. Shim, J. Seo, S. Min, T. Cho, S. Kang, S., Microelectron. Reliab. 2007; 47: 1928.

[57] K. Suganuma, A. Baated, K.S. Kim, K. Hamasaki, N. Nemoto, T. Nakagawa, T. Yamada, Sn whisker growth during thermal cycling, Acta Mater. 2011; 59: 7255.

[58] L.A. Pinol, J. Melngailis, H.K. Charles, D.M. Lee, R. Deacon, G. Coles, G. Clatterbaugh, IEEE Trans. Compon. Packag. Manuf. Technol. 2011; 1: 2028.

[59] J. Cheng, F.Q. Yang, P.T. Vianco, B. Zhang, J.C.M. Li, J. Electron. Mater. 2011; 40: 2069.

[60] M.H. Lu, K.C. Hsieh, J. Electron. Mater. 2007; 36: 1448.

[61] V. Glazunova, and N. Kudryavtsev, An investigation of the conditions of spontaneous growth of filiform crystals on electrolytic coatings, Translated from Zhurnal Prikladnoi Khimii, 36, no. 3, pp. 543 - 550, March 1963.

[62] R. Schetty, Minimization of Tin Whisker Formation for Lead Free Electronics Finishing, Proceedings IPC Works Conference, Miami, USA, 2000.

[63] Y. Zhang, C. Su, C. Fan, and J. Abys, Tin whisker growth and prevention, Journal of surface mount technology. 2000; 13: 1.

[64] N. Okamoto, Y. Fujii, H. Kurihara, K. Kondo, Mater. Trans. 2009; 50: 2570.

[65] Jay A. Brusse, Gary J. Ewell, and Jocelyn P. Siplon, Tin whiskers: attributes and mitigation, carts 2002: 22nd Capacitor and Resistor Technology Symposium, 25-29 March 2002.

[66] T. Kakeshita, R. Kawanaka, and T. Hasegawa, J. Mater. Sci. 1982; 17: 2560.

[67] Masanobu Tsujimoto, Shigeo Hashimoto, Masayuki Kiso, Raihei Ikumoto,Toshikazu Kano and Genki Kanamori, The elimination of whiskers from electroplated tin, C. Uyemuri and Co. Ltd [Accessed: 04/01/2017].

[68] W.J. Boettinger, C.E. Johnson, L.A. Bendersky, K.W. Moon, M.E. Williams, G.R. Stafford, Acta Mater. 2005; 53: 5033.

[69] E. Sandnes, M.E. Williams, M.D. Vaudin, G.R. Stafford, J. Electron. Mater. 2008; 37: 490.

[70] A. Dimitrovska, R. Kovacevic, J. Electron. Mater. 2009; 38: 2726.

[71] A. Baated, K. Hamasaki, S.S. Kim, K.S. Kim, K. Suganuma, J. Electron. Mater. 2011; 40: 2278.

[72] B.D. Dunn, European space agency (esa) journal. 1988; 12: 1.

[73] B.E. Powell and M.J. Skove, J. Appl. Phys. 1965; 36: 1495.

[74] Wonmo Kang, Jagannathan Rajagopalan, and M. Taher A. Saif, Nanosci Nanotechnol Lett. 2010; 2: 282.

[75] J. Rajagopalan, C. Rentenberger, H.P. Karnthaler, G.Dehm, and M.T.A. Saif, Acta Mater. 2010; 58: 4772.

[76] J. Rajagopalan and M.T.A. Saif, J. Mater. Res. 2011; 26: 2826.

[77] J.H. Han and M.T.A. Saif, Rev. Sci. Instrum. 2006; 77: 045102.

[78] J.H. Han, J. Rajagopalan, and M.T.A. Saif, Proc. SPIE 6464, 64640C (2007).

[79] Aluminum Standards and Data 1984, The Aluminum Association, Inc., Washington, D.C. 20006.

[80] E. A. Starke, Jr and J. T. Staley, Pro 9. Aerospace Sci. 1996; 32: 131.

[81] T.-S. Huang, MSc. Thesis, Ohio State University, USA, 2005.

[82] J. F. Li, Z. W. Peng, Z. Jia, W. Chen, Z. Zheng, Trans. Nonferrous Met. Soc. China. 2008; 18: 755.

[83] T. P. Savas, J. C. Earthman, J. Mater. Eng. Perform. 2008; 17: 674.

[84] N. L. Sukiman, X. Zhou, N. Birbilis, A.E. Hughes, J. M. C. Mol, S. J. Garcia, X. Zhou and G. E. Thompson (2012). Durability and Corrosion of Aluminium and Its Alloys: Overview, Property Space, Techniques and Developments, DOI: 10.5772/53752.

[86] J. Payne, G. Welsh, R.J. Christ Jr., J. Nardiello, J.M. Papazian, Int J Fatigue. 2010; 32: 247.

[87] Y. Xue, H.E. Kadiri, M. Horstemeyer, J. Jordon, H. Weiland, Acta Mater. 2007; 55: 1975.

[88] M. C. Reboul, B. Baroux, Mater. Corros. 2011; 62: 215.

[89] C.M.A. Brett, Corros. Sci. 1992; 33: 203.

[90] R. Ambat, E.S. Dwarakodasa, J. Appl. Electrochem. 1994; 24: 911.

[91] W. Carrol, C. Breslin, Br Corros J. 1991; 26: 255.

[92] P. Natishan, E. McCafferty, G. Hubler, Proceedings- The electrochemical society. Pennington, 86–7 (1986), pp. 437–449.

[93] R. Horst, Mater. Perform. 1977; 16: 23.

[94] D.A. Horner, B.J. Connolly , S. Zhou, L. Crocker, A. Turnbull, Corros Sci. 2011; 53: 3466.

[95] G.S. Chen, M. Gao, and R.P. Wei, Corrosion. 1996, 52: 8.

[96] S. Chen, K.-C. Wan, M. Gao, R.P. Wei, and T.H. Flournoy, Mater.Sci. Eng. 1996; A219: 126.

[97] R.S. Piascik and S.A. Willard, Fat. Fract. Eng. Mater. Struct. 1994; 17: 1247.

[98] Hosni Ezuber, A. El-Houd, F. El-Shawesh, Mater. Des. 2008; 29: 801.

[99] K.K. Sankaran, R. Perez, K.V. Jata, Materails science and engineering: A. 2001; 297: 223.

[100] D.L DuQuesnay, P.R Underhill, H.J Britt, Int J Fatigue. 2003; 25: 371.

[101] G. Bereket, A. Yurt, Corros Sci. 2001; 43: 1179.

[102] K.E. Yazzie, J.J. Williams, N.C. Phillips, F. De Carlo, N. Chawla, Mater Char. 2012; 70: 33.

[103] Sudhanshu S. Singh, Jason J. Williams, Tyler J. Stannard, Xianghui Xiao, Francesco De Carlo, Nikhilesh Chawla, Corros sci. 2016; 104: 330.

[104] Sudhanshu S. Singh, Jason J. Williams, X. Xiao, F. De Carlo and N. Chawla, Fatigue of Materials II Advances and Emergences in Understanding, Edited by: T.S. Shvatsan, M. Ashrafimam. and R. Srinivasan TMS (The Minerals, Metals & Materials Society), 20.

[105] S. S. Singh, J. J. Williams, M.F.Lin, X. Xiao, F. De Carlo and N. Chawla, Mater.Res.Lett. 2014; 2: 217.

[106] Y. Nakai and D. Shiozawa, EPJ Web of Conferences 6, 35004 (2010).

[107] S.P. Knight, M. Salagaras, A.R. Trueman, Corros sci. 2011; 53: 727.

[108] L Babout, TJ Marrow, D Engelberg, PJ Withers, Mater. Sci.Technol. 2006; 22: 1068.

[109] E. M. Sherif, S.-M. Park, J. Electrochem. Soc. 2005; 152: B205.

[110] W. R. Osório, N. Cheung, L. C. Peixoto, A. Garcia, Int. J. Electrochem. Sci. 2009; 4: 820.

[111] E. M. Sherif, S.-M. Park, Electrochim. Acta. 2006; 51: 1313.

[112] W. Diggle, T. C. Downie, C. Goulding, Electrochim. Acta. 1970; 15: 1079.

[113] Fang Wang, Yabin Wang, Yanni Li, Int. J. Electrochem. Sci. 2011; 6: 793.

[114] A. I. Onen, B. T. Nwufo, E. E. Ebenso, R. M. Hlophe, Int. J. Electrochem. Sci. 2010; 5: 1563.

[115] R. T. Foley and T. H. Nguyen, J. Electrochem. Soc.: Electrochemical Science And Technology. 1982; 129: 464.

[116] J. K. Park, Mater. Sci. Eng. 1988; A103: 223.

[117] H. Vogt and M. O. Speidel, Corros. Sci. 1998; 40: 251.

[118] Shumin Li, Ziguang Chen, Fei Wang, Bai Cui, Li Tan, and Florin Bobaru, J. Electrochem. Soc. 2016; 163: C784.

[119] W. Song, H. J. Martin, A. Hicks, D. Seely, C. A. Walton, W. B. Lawrimore, P. T. Wang, and M. F. Horstemeyer, Corros. Sci. 2014; 78: 353.

[120] Ilaria M. Comotti, Monica Trueba and Stefano P. Trasatti, Special Issue: Aluminium Surface Science and Technology. 2013; 45: 1575.

[121] Oliver, W., & Pharr, G., J. Mater. Res. 2004; 19: 3.

[122] G.M. Pharr, W.C. Oliver, and F.R. Brotzen, J. Mater. Res. 1992; 7: 613.

[123] Hay J., Experimental techniques. 2009; 33: 66.

[124] X. Li and B. Bhushan, Mater. Charact. 2002; 48: 11.

CHAPTER 3

[1] iNEMI Tin Whisker User Group, Recommendations on lead-free finishes for components used in high-reliability products, version 4, http://www.inemi.org/cms/ [accessed 04/15/2016].

[2] NASA, Multiple examples of whisker-induced failures are documented on the NASA website, http://nepp.nasa.gov/whisker/ [accessed 04/15/2016].

[3] R.M. Fisher, L.S. Darken, and K.G. Carroll, Acta Metall. 1954; 2: 368.

[4] B.D. Dunn, Circuit World. 1976; 2: 32.

[5] C. Xu, IEEE Trans. Electron. Packag. 2005; 28: 31.

[6] Choi WJ, Lee TY, Tu KN, Tamura N, Celestre RS, Mcdowell AA, et al, proceedings of the 52nd electronics components and technology conference; May 28–31, 2002. p. 628–33.

[7] M. Sobiech, C. Krüger, U. Welzel, J.Y. Wang, E.J. Mittemeijer, W. Hügel, J. Mater. Res. 2010; 25: 2166.

[8] C. Xu, Y. Zhang, C.L. Fan, J.A. Abys, IEEE Trans. Electron. Packag. Manuf. 2005; 28: 31.

[9] M.J. Bozack, E.R. Crandall, C.L. Rodekohr, R.N. Dean, G.T. Flowers, J.C. Suhling, IEEE Trans. Electron. Packag. Manuf. 2010; 33: 198.

[10] K. Murakami, M. Okano, M. Hino, M. Takamizawa, K. Nakai, Mater. Trans. 2010; 51: 143.

[11] W.J. Boettinger, C.E. Johnson, L.A. Bendersky, K.W. Moon, M.E. Williams, G.R. Stafford, Acta Mater. 2005; 53: 5033.

[12] K.N. Tu, Acta Metall. 1973; 21: 347.

[13] X. Deng, G. Piotrowski, J.J. Williams, N. Chawla, J. Electron. Mater. 2003; 32: 1403.

[14] B.Z. Lee, D.N. Lee, Acta Mater. 1998; 46: 3701.

[15] E. Chason, N. Jadhav, W.L. Chan, L. Reinbold, K.S. Kumar, Appl. Phys. Lett. 2008; 92: 171901.

[16] Craig Hillman, Gregg Kittlesen, and Randy Schueller, A new (better) approach to tin whisker mitigation, Dfr solutions, http://www.dfrsolutions.com/uploads/white-papers/WP_SnWhisker.pdf, [accessed 04/15/2016].

[17] Tadahiro Shibutani, Qiang Yu, Masaki Shiratori, Michael G. Pecht, Microelectron. Reliab. 2008; 48: 1033.

[18] S.S. Singh, R. Sarkar, H.-X. Xie, C. Mayer, J. Rajagopalan and N. Chawla, J. Electron. Mater. 2014; 43: 978.

[19] B.E. Powell and M.J. Skove, J. Appl. Phys. 1965; 36: 1495.

[20] B.D. Dunn, Eur. Space Agency (ESA) J. 1987; 11: 1.

[21] NASA, The continuing dangers of tin whiskers and attempts to control them with conformal coating, http://nepp.nasa.gov/docuploads/95565195-0E5A-40D8-98D88425FF668F68/JayBrusseRevision2.pdf [accessed 04/15/2016].

[22] J. Smetana, iNEMI tin whisker user group. iNEMI recommendations on lead free finishes for components used in high reliability products, Proceedings of IPC Printed Circuits Exposition, Apex, and the Designers Summit, Anaheim, CA, February 5–10, 2006.

[23] L.A. Pinol, J. Melngailis, H.K. Charles, D.M. Lee, R. Deacon, G. Coles, G. Clatterbaugh, IEEE Trans. Compon. Packag. Manuf. Technol. 2011; 1: 2028.

[24] J. Cheng, F.Q. Yang, P.T. Vianco, B. Zhang, J.C.M. Li, J. Electron. Mater. 2011; 40: 2069.

[25] M.H. Lu, K.C. Hsieh, J. Electron. Mater. 2007; 36: 1448.

[26] S.C. Britton, Trans. Inst. Metal Finishing. 1974; 52: 95.

[27] W.J. Choi, T.Y. Lee, K.N. Tu, N. Tamura, R.S. Celestre, A.A. MacDowell, Y.Y. Bong, L. Nguyen, Acta. Mater. 2003 ; 51: 6253.

[28] K.N. Tu, Phys. Rev. B. 1994; 49: 2030.

[29] B.-Z. Lee, D.N. Lee, Acta Mater. 1998; 46: 3701.

[30] K.S. Kumar, L. Reinbold, A.F. Bower, and E. Chason, J. Mater. Res. 2008; 23: 2916.

[31] J.W. Osenbach, J.M. De Lucca, B.D. Potterger, A. Amin, R.L. Shook, F.A. Baiocchi, IEEE Trans. EPM. 2007; 30: 23.

[32] E. Chason, N. Jadhav, W.L. Chan, L. Reinbold, K.S. Kumar, Appl. Phys. Lett. 2008; 92: 171901.

[33] W.J. Boettinger, C.E. Johnson, L.A. Bendersky, K.-W. Moon, M.E. Williams, G.R. Stafford, Acta Mater. 2005; 53: 5033.

[34] Kyle Doudrick, Jeff Chinn, Jason Williams, Nikhilesh Chawla, Konrad Rykaczewski, Microelectron. Reliab. 2015; 55: 832.

[35] J. Rajagopalan, C. Rentenberger, H.P. Karnthaler, G. Dehm, and M.T.A. Saif, Acta Mater. 2010; 58: 4772.

[36] J. Rajagopalan and M.T.A. Saif, J. Mater. Res. 2011; 26: 2826.

[37] J.H. Han and M.T.A. Saif, Rev. Sci. Instrum. 2006; 77: 045102.

[38] J.H. Han, J. Rajagopalan, and M.T.A. Saif, Proc. 2007; SPIE 6464: 64640C.

[39] M.A. Haque and M.T.A. Saif, Exp. Mech. 2002; 42: 123.

[40] J.J. Williams, N.C. Chapman, and N. Chawla, J. Electron. Mater. 2013; 42: 224.

[41] Shih-Kang Lin, Yuhi Yorikado, Junxiang Jiang, Keun-Soo Kim, Katsuaki Suganuma, Sinn-Wen Chen, Masanobu Tsujimoto, and Isamu Yanada, J. Electron. Mater. 2007; 36: 1732.

[42] Kiyotaka Tsuji, Role of grain-boundary free energy & surface free energy for tin whisker growth, http://unicon.co.jp/business/pdf/data_rollofgrain.pdf [accessed 04/15/2016].

[43] K. N. Tu, Chih Chen, Albert T. Wu, J Mater Sci: Mater Electron. 2007; 18: 269.

[44] M.W. Barsoum, E.N. Hoffman, R.D. Doherty, S. Gupta, and A. Zavaliangos, Phys. Rev. Lett. 2004; 93: 206104.

[45] B.-Z. Lee and D.N. Lee, Acta Mater. 1998; 46: 3701.

[46] Ray, U., I. Artaki, and P.T. Vianco, IEEE Transactions on components, packaging, and manufacturing technology-part a. Vol. IX. NO I, March 1995.

[47] Copper-Tin Intermetallic Compounds, copper development association Inc., http://www.copper.org/applications/industrial/DesignGuide/performance/coppertin03.html [accessed 04/15/2016].

[48] K.S. Kumar, L. Reinbold, A.F. Bower, and E. Chason, J. Mater. Res. 2008; 23: 171901.

[49] Kinoshita Y, Matsushima H, Ohno N. Model Simul Mater Sci Eng. 2012; 20:035003.

[50] Kinoshita Y, Ohno N., Key Eng. Mater. 2015; 626: 20.

CHAPTER 4

[1] E.A. Starke Jr., J.T. Staley, Progress in Aerospace Sciences. 1996; 32: 131.

[2] A. AlHazaa, T.I. Khan, I. Haq, Mater Charact. 2010; 61: 312.

[3] C.M. Cepeda-Jimenez, J.M. Garcia-Infanta, O.A. Ruano, F. Carreno, J. Alloys Comp. 2011; 509: 8649.

[4] Arsenault, B., Simard, S., Marcoux, P., & Ghali, E. (2006, January 1). Stress Corrosion Cracking Mitigation of 7075-T6 Aluminum Alloy by Thermal Spray Coating. NACE International.

[5] B.W. Samuels, K. Satoudeh, R.T. Foley, Corrosion. 1981; 37: 92.

[6] M. Baumgaertner, H. Kaesche, Corros. Sci. 1990; 31: 231.

[7] J. Davis (Ed.), Corrosion of aluminum and aluminum alloys (2nd ed.), ASM International, USA (1999), pp. 25–49.

[8] Z. Szklarska-Smialowska, Corros Sci. 1999; 41: 1743.

[9] B. Shaw, G. Davis, W. Moshier, G. long, R. Black, J Electrochem Soc. 1991; 138: 3288.

[10] C.M.A. Brett, Corros. Sci. 1992; 33: 203.

[11] R. Ambat, E.S. Dwarakodasa, J. Appl. Electrochem. 1994; 24: 911.

[12] W. Carrol, C. Breslin, Br Corros J. 1991; 26: 255.

[13] P. Natishan, E. McCafferty, G. Hubler, Proceedings- The electrochemical society. Pennington, 86–7 (1986), pp. 437–449.

[14] R. Horst, Mater Perform. 1977; 16: 23.

[15] T.H. Nguyen, R.T. Foley, J. Electrochem. Soc. 1979; 126: 1855.

[16] L.F. Lin, C.Y. Chao, D.D. Macdonald, J. Electrochem. Soc. 1981 ; 128 : 1194.

[17] G. Bereket, A. Yurt, Corros sci. 2001; 43: 1179 .

[18] D.A. Horner, B.J. Connolly , S. Zhou, L. Crocker, A. Turnbull, Corros. Sci. 2011; 53: 3466.

[19] G.S. Chen, M. Gao, and R.P. Wei, Corrosion. 1996; 52: 8.

[20] S. Chen, K.-C. Wan, M. Gao, R.P. Wei, and T.H. Flournoy, Mater.Sci. Eng. 1996; A219: 126.

[21] R.S. Piascik and S.A. Willard:Fat. Fract. Eng. Mater. Struct. 1994; 17: 1247.

[22] S. Barter, P.K. Sharp, G. Clark, Eng. Fail. Anal. 1994; 1: 255.

[23] Hosni Ezuber, A. El-Houd, F. El-Shawesh, Mater. Des. 2008; 29: 801.

[24] K.K. Sankaran, R. Perez, K.V. Jata, Mater. Sci. Eng., A. 2001; 297: 223.

[25] D.L DuQuesnay, P.R Underhill, H.J Britt, Int. J. Fatigue. 2003; 25: 371.

[26] G. Bereket, A. Yurt, Corros. Sci. 2001; 43: 1179.

[27] R.S. Sidhu, N. Chawla, Scr. Mater. 2006; 54: 1627.

[28] E. Padilla, V. Jakkali, L. Jiang, N. Chawla, Acta Mater. 2012; 60: 4017.

[29] J.J. Williams, Z. Flom, A.A. Amell, N. Chawla, X. Xiao, F. De Carlo, Acta Mater. 2010; 58: 6194.

[30] J.J. Williams, N.C. Chapman, V. Jakkali, V.A. Tanna, N. Chawla, X. Xiao, F. De Carlo, Metall. Mater. Trans. A. 2011; 42: 2009.

[31] Kimberli Jones, David W. Hoeppner, Int. J. Fatigue. 2009; 31: 686.

[32] N. Birbilis, M.K. Cavanaugh, R.G. Buchheit, Corros. Sci. 2006; 48: 4202.

[33] Minhua Shao, Yan Fu, Ronggang Hu, Changjian Lin, Mater. Sci. Eng,. A. 2003; 344: 323.

[34] Sudhanshu S. Singh, Jason J. Williams, Tyler J. Stannard, Xianghui Xiao, Francesco De Carlo, Nikhilesh Chawla, Corros. Sci. 2016 ; 104 : 330.

[35] Sudhanshu S. Singh, Jason J. Williams, X. Xiao, F. De Carlo and N. Chawla, Fatigue of Materials II Advances and Emergences in Understanding, Edited by: T.S. Shvatsan, M. Ashrafimam. and R. Srinivasan TMS (The Minerals, Metals & Materials Society), 20.

[36] S. S. Singh, J. J. Williams, M.F.Lin, X. Xiao, F. De Carlo and N. Chawla, Mater.Res.Lett. 2014; 2: 217.

[37] Y. Nakai and D. Shiozawa, EPJ Web of Conferences 6, 35004 (2010).

[38] S.P. Knight, M. Salagaras, A.R. Trueman, Corros. Sci. 2011; 53: 727.

[39] T.J. Marrow, L. Babout, B.J. Connolly, D. Engelberg, G. Johnson, J.-Y. Buffiere, P.J. Withers and R.C. Newman, High-resolution, in-situ, tomographic observations of stress corrosion cracking.

[40] J.J. Williams, K.E. Yazzie, E. Padilla, N. Chawla, X. Xiao, F. De Carlo, Int. J. Fatigue. 2013; 57: 79.

[41] Sudhanshu S Singh, Jason J Williams, Peter Hruby, Xianghui Xiao, Francesco De Carlo and Nikhilesh Chawla, Integrating Materials and Manufacturing Innovation. 2014; 3: 9.

[42] J.C.E. Mertens, J.J. Williams, Nikhilesh Chawla, Mater. Charact. 2014; 92: 36.

[43] Y. Yeh, W. Liu, Metall. Mater. Trans. A. 1996; 27A: 3558.

[44] A. Balasundaram, A.M. Gokhale, S. Graham, M.F. Horstemeyer, Mater. Sci. Eng. A. 2003; 355: 368.

[45] T.G. Dunford, B.E. Wilde, in: M.E. Blum, P.M. French, R.M. Middleton, G.F. Vander Voort (Eds.), Microstructure Science, vol. 15, American Society for Metals, Metals Park, OH, and International Metallographic Society, Columbus, OH, pp. 263, 1987.

CHAPTER 5

[1] E.A. Starke Jr., J.T. Staley, Progress in Aerospace Sciences. 1996; 32: 131.

[2] A. AlHazaa, T.I. Khan, I. Haq, Mater. Charact. 2010; 61: 312.

[3] C.M. Cepeda-Jimenez, J.M. Garcia-Infanta, O.A. Ruano, F. Carreno, J. Alloys \ Comp. 2011; 509: 8649.

[4] Arsenault, B., Simard, S., Marcoux, P., & Ghali, E. (2006, January 1). Stress Corrosion Cracking Mitigation of 7075-T6 Aluminum Alloy by Thermal Spray Coating. NACE International.

[5] Davis, J. R. (2000), Corrosion of aluminum and aluminum alloys, Materials Park: ASM International.

[6] E. M. Sherif, S.-M. Park, J. Electrochem. Soc. 2005; 152: B205.

[7] W. R. Osório, N. Cheung, L. C. Peixoto, A. Garcia, Int. J. Electrochem. Sci. 2009; 4: 820.

[8] E. M. Sherif, S.-M. Park, Electrochim. Acta. 2006; 51: 1313.

[9] W. Diggle, T. C. Downie, C. Goulding, Electrochim. Acta. 1970; 15: 1079.

[10] Fang Wang, Yabin Wang, Yanni Li, Int. J. Electrochem. Sci. 2011; 6: 793.

[11] A. I. Onen, B. T. Nwufo, E. E. Ebenso, R. M. Hlophe, Int. J. Electrochem. Sci. 2010; 5: 1563.

[12] J. K. Park, Mater. Sci. Eng. A. 1988; 103: 223.

[13] H. Vogt and M. O. Speidel, Corros. Sci. 1998; 40: 251.

[14] Z. Szklarska-Smialowska, Corros. Sci. 1999; 41: 1743.

[15] W. Carrol, C. Breslin, Corros. J. 1991; 26: 255.

[16] P. Natishan, E. McCafferty, G. Hubler, Proceedings- The electrochemical society. Pennington, 86–7 (1986), pp. 437–449.

[17] Shumin Li, Ziguang Chen, Fei Wang, Bai Cui, Li Tan, and Florin Bobaru, J. Electrochem. Soc. 2016; 163: C784.

[18] W. Song, H. J. Martin, A. Hicks, D. Seely, C. A. Walton, W. B. Lawrimore, P. T. Wang, and M. F. Horstemeyer, Corros. Sci. 2014; 78: 353.

[19] Ilaria M. Comotti, Monica Trueba and Stefano P. Trasatti, Surface and Interface Analysis Special Issue: Aluminium Surface Science and Technology. 2013; 45: 1575.

[20] Z. Chen and F. Bobaru, J. Mech. Phys. Solids. 2015; 78: 352.

[21] Z. Chen, G. Zhang, and F. Bobaru, J. Electrochem. Soc. 2016; 163: C19.

[22] W. C. Neil,M. Forsyth, P. C.Howlett,C. R. Hutchinson, and B. R. W. Hinton, Corros. Sci. 2009; 51: 387.

[23] M. Hasatani and Y. Itaya, Drying Technol. 1996; 14: 1011.

[24] D. Mihoubi and A. Bellagi, Transp. Porous Media. 2009; 80: 519.

[25] Sudhanshu S. Singh, Cary Schwartzstein, Jason J. Williams, Xianghui Xiao, Francesco De Carlo, Nikhilesh Chawla, J. Alloys Cmpnd. 2014; 602: 163.